University of Alberta

Suppression of addition reactions of asphaltene model compound
during hydrogenation with sulfided iron catalyst

by

Farhood Karbalaee Habib

A thesis submitted to the Faculty of Graduate Studies and Research
in partial fulfillment of the requirements for the degree of

Master of Science in Chemical Engineering

Department of Chemical and Materials Engineering

© Farhood Karbalaee Habib
Fall 2013
Edmonton, Alberta

Abstract

Due to the complexity of asphaltene and other fractions of vacuum residue, we used a model compound to probe the chemical and physical behaviors of asphaltene. Hydrogenation reactions were conducted in a batch microreactor at 430℃, 13.9 MPa H_2 for 30 min using a solution of 1,3,6,8-tetrahexylpyrene (THP) in tetralin. Sulfided iron was prepared on α-alumina, γ-alumina and glass beads as support materials. The hypothesis of this study was that addition reactions can be suppressed under hydrogenation conditions by using sulfided iron as a low active catalyst in the presence of hydrogen gas and a hydrogen donor solvent, by saturating olefin intermediates. The products were analyzed by high performance liquid chromatography, gas chromatography, matrix assisted laser desorption ionization mass spectrometry, and proton nuclear magnetic resonance spectroscopy to investigate conversion and product distribution for different catalysts and without added catalyst. The results show that catalyst can give significant suppression of addition reactions from 63 mol % for non-catalytic to 13 mol % for sulfided Fe/α-Al$_2$O$_3$ and shift the selectivity toward cracking, without giving a high level of hydrogenation of the aromatics.

Acknowledgements

Table of Contents

List of Tables

List of Figures

Nomenclature

A_{THP}	Model compound peak area
A_s	Internal standard peak area
A_P	Pyrene and alkylpyrenes peak areas
RF	Response factor for HPLC
RF^{GC}	Response factor for GC-FID
W_{THP}	Model compound mass (mg)
W_s	Internal standard mass (mg)
W_P	Pyrene and alkylpyrenes masses (mg)
t	Time (s)
X	Conversion

CHAPTER 1

Introduction

1.1 Introduction

As the world energy demand increases, growing attention has been paid to the unconventional resources, such as heavy oil, bitumen and vacuum residue. Although many countries are reported to have bitumen deposits, large quantities are found in Alberta, Canada and it is playing a significant role in filling the gap of world demands. This province has the third largest oil reserves, after Saudi Arabia and Venezuela, with 170.8 billion barrels of oil, over 99% of which is bitumen,

making Canada an important worldwide player for production of unconventional oils. (1)

Unfortunately, extraction, transportation, and refining of the heavy oils and bitumen have many difficulties and complications, and upgrading operations are needed for refineries in order to process them. Heavy oils and bitumen have high density, therefore low API gravity, high viscosity, high heteroatom content, such as nitrogen and sulfur, as well as high metal content of nickel and vanadium. (2) The heteroatoms and metals content have to be reduced to meet the environmental regulations and prevent fouling and deactivation of catalysts in downstream upgrading processes such as hydroconversion and hydrotreating. Likewise, the vacuum residue, which is the material that remains non-distillable after vacuum distillation, typically accounts for up to 50% of the whole bitumen. (3) Therefore thermal cracking technologies are most commonly used to convert this fraction into more beneficial distillable liquids.

Asphaltenes are the heaviest portion of petroleum, existing in a significant portion in the bitumen, heavy oils, and VR and in less extent in the most of conventional oil. Compared with about 1% fraction in a light density crude oil, the concentration of asphaltenes in bitumen can be as much as 20%. As a solubility class that is soluble in toluene and insoluble in heptane, the asphaltene fraction contains the most complex constituents extracted from the oil. The asphaltenes have higher heteroatom content than the VR or bitumen, and higher tendency of forming large amounts of solid residue, or coke, during thermal upgrading processes. (3, 4)

Studies suggested that a reasonable mechanism for coke formation from hydrocarbons is free-radical chain addition reactions followed by rearrangement to give a more thermally stable product. (5) This type of reaction process would promote the phase separation mechanism that was known to be responsible for coke formation. (6, 7) Suppression of coke formation during thermal cracking, either at low pressure or with added catalysts and hydrogen at high pressure, is an important target for upgrading of bitumen fractions. The ability to understand and control the

addition reactions is an important part of addressing the need to avoid reactions resulting in products with higher molecular weight than the starting components.

1.1.1 Hypothesis

Investigation of the reactions in the presence of sulfided iron catalyst as a cheap and low activity catalyst for suppression of addition reactions and coke formation in presence of hydrogen-donor solvent and in H_2 environment is the objective of this work. Iron catalysts have been proposed for hydrocaonversion of vacuum residue and bitumen, and for coal liquefaction (8-10). In such complex feeds, molecular analysis of heavy components such as asphaltenes by mass spectroscopy techniques is impossible due to its tendency to form aggregates in solution and the wide range of compounds that are present in this solubility class. (11) The catalysts are also expected to change during reaction, with sulfide forms ranging from the pyrite to nonstoichiometric pyrrhotite. (8) Further, a variety of cracked products are obtained from reaction, and these are extremely difficult to characterize. Therefore, it is difficult to optimize conditions, to sort out desired processes, and to obtain meaningful information about catalyst activity and selectivity using actual asphaltene.

One possible alternative is the use of simple compounds as reactants to model reactions of importance in asphaltene hydroconversion to simulate its physical and chemical behaviors. The primary criterion for the selection of model compound in our study is that the model compound reactions should mimic the actual chemistry taking place in asphaltene conversion.

Following from the proposed mechanism of conversion of vacuum residue (5), our hypothesis is that active iron sulfides will hydrogenate unsaturated intermediates, thereby suppressing addition reactions without interfering with the thermal cracking reactions that occur by a free-radical mechanism.

1.1.2 Objectives

Hydrogenation of 1,3,6,8-tetrahexylpyrene in tetralin as a hydrogen donor solvent with sulfided iron catalysts for suppression of addition reactions is studied in this work with following objectives:

1) Preparation of sulfided iron catalyst on various supports
2) Conducting catalytic hydrogenation reactions to be compared together and also with control experiments, including also a commercial Ni-Mo catalyst
3) Identification and quantification of products with analytical methods such as high performance chromatography, gas chromatography, proton nuclear magnetic resonance spectroscopy and matrix assisted laser desorption ionization mass spectroscopy
4) Characterization of catalyst before and after reaction with scanning image microscopy, atomic absorption spectroscopy, X-ray diffraction and X-ray photoelectron spectroscopy to have information about bulk and surface properties of catalyst

1.1.3 Outlines

The thesis is organized in five chapters, including this introduction as the first chapter. The second chapter gives background on the relevant literature. A brief overview of the asphaltenes, including their definition, structure, main properties, and thermal reactions, is presented in this chapter. In addition to the thermal reactions of the asphaltenes and VR, a few important studies on the thermal reactions of model compounds will be reviewed. Then, the importance of catalytic reactions and specifically iron catalyst is reported and relevant catalytic industrial processes are introduced.

The third chapter is about the material and detailed experimental method used in this study, as well as the instruments and method of analysis.

In the fourth chapter, the results are presented including validation experiments, control experiments, the method of calculation, results of catalytic hydrogenation reaction and finally discussion and interpretation of experimental data.

Chapter six is dedicated to the summary of results, conclusions and implications of this study. Also additional information and spectra of analysis are presented in appendices.

1.2 References

1. Alberta oilsands, about the oilsand [Internet].: Government of Alberta; 2012. Available from: http://www.oilsands.alberta.ca/resource.html.

2. Strausz O, Lown E. The chemistry of alberta oil sands, Bitumens, and heavy oils. AERI. Calgary. ; 2003.

3. Speight JG. The chemistry and technology of petroleum fourth edition. ; 2007.

4. Siskin M, Kelemen SR, Eppig CP, Brown LD, Afeworki M. Asphaltene molecular structure and chemical influences on the morphology of coke produced in delayed coking. Energy Fuels. 2006;20(3):1227-34.

5. Alshareef AH, Scherer A, Tan X, Azyat K, Stryker JM, Tykwinski RR, et al. Formation of archipelago structures during thermal cracking implicates a chemical mechanism for the formation of petroleum asphaltenes. Energy Fuels. 2011;25(5):2130-6.

6. Wiehe I. A solvent resid phase-diagram for tracking resid conversion. Ind Eng Chem Res. 1992;31(2):530-6.

7. Wiehe I. A phase-separation kinetic-model for coke formation. Ind Eng Chem Res. 1993;32(11):2447-54.

8. Chadha A, Stinespring C, Stiller A, Zondlo J, Dadyburjor D. Characterization and activity of ferric-sulfide-based catalyst in model reactions of direct coal liquefaction: Effect of preparation conditions. Ind Eng Chem Res. 1997;36(2):284-95.

9. Suzuki T, Ikenaga N. Development of catalyst for commercial coal liquefaction process and recent research trend. Nihon Enerugi Gakkaishi/Journal of the Japan Institute of Energy. 1998;77(4):268-76.

10. Montano PA, Lee YC, Yeye-Odu A, Chien CH. Iron sulfide catalysis in coal liquefaction. Mineral matter and ash in coal. developed from a symposium at the 188th meeting of the american chemical society. Philadelphia, PA, USA: ACS; 1986.

11. Gray MR, Tykwinski RR, Stryker JM, Tan X. Supramolecular assembly model for aggregation of petroleum asphaltenes. Energy Fuels. 2011;25(7):3125-34.

CHAPTER 2

Literature Review

2.1   Literature Review

The properties, specifications and thermal behavior of vacuum residue and asphaltene components must be reviewed to link the behavior of model compounds under cracking conditions to the real asphaltenes. The analysis in this thesis are based on the evidence that the same organic structural elements occur in a number of fractions of bitumen. The main distinction of the asphaltenes, compared to the

remainder of the vacuum residue fraction, is the strong tendency to self-associate, and the low solubility in paraffinic solvents. The current understanding of the asphaltenes, and key features and properties such as the molecular weight and structure, and modeling of the asphaltenes will be summarized in this section. Following the above comment, these features apply to many of the components of vacuum residues from bitumen and petroleum, not just the asphaltene solubility class. Moreover, essential information about the pathways and mechanisms of cracking, reactions of polycyclic alkyl aromatics, properties and performance of sulfide catalysts and industrial hydroconversion operational units will be presented here.

2.1.1   Composition and Structure of Vacuum Residua and Asphaltenes

Oil sands are composed of 16 wt % bitumen and water as well as 84 wt % sand and clay. Bitumen is generally produced by either open pit mining or in situ production. The overall properties of bitumen are not attractive due to low API gravity, high content of vacuum residue, sulfur, nitrogen, metals and high viscosity. The quality is poor given its low hydrogen content and H/C ratio. A comparison of conventional light crude and bitumen is shown in Table 2-1.

Table 2-1 Comparison of light crude and bitumens (1)

Property	Light crude	Athabasca bitumen	Cold lake bitumen
API gravity	40.8	10	9
Sulfur, wt %	0.3	4.4	4.9
Nitrogen, wt %	0.08	0.4	0.5
Metals, wppm	3.2	220	280
Viscosity, $\frac{m^2}{s} \times 10^6$ at 40℃	4	5000	7000
Vacuum residue, 524℃ +, vol %	12.9	52	52

Petroleum crude oils are complex combinations of more than tens of thousands of compounds.(2) Vacuum residua are the heaviest fractions of crude, and are

typically defined as the fraction boils above 524 °C. Fractionation of petroleum using solvents has been done for years. (3) One of these fractions is named asphaltene, which is black powdery materials precipitated by addition of n-alkane solvents to petroleum, residua, or bitumen. (4) Hence, the asphaltene fraction is a solubility class that is soluble in aromatic solvents, such as toluene, and insoluble in n-pentane or n-heptane. The definition based on solubility in aromatics and insolubility in alkanes makes the asphaltene the least soluble fraction of petroleum, including compounds with low solubility because of molecular weight, high aromaticity, polarity, or any combination of the three. In the industry, the removal of the asphaltenes from petroleum is used to reduce the metal and heteroatom contents of the remaining oil or to separate the oil for production of lube cut (e.g propane deasphalting). This reduction can be useful to provide longer lifecycle for catalysts in the downstream processes. Many different solvents such as paraffins, isoparaffins, straight–run naphtha, or other non–aromatic solvents over a range of dilutions and temperatures are being used for industrial precipitation of asphaltenes. (5) For processing of heavy oils and bitumens, deasphalting is not a viable strategy because large volumes of low-value asphalt are produced without an available market or other value.

2.1.1.1 Elemental composition

Although the asphaltene is a complex mixture of different compounds, the general building blocks are the same among asphaltenes from different places, and indeed the remainder of the vacuum residue. (4) The asphaltene is made up of C, H, N, S, O, Ni, and V. (6) For example, the range of C, H, S, N, and O in the asphaltenes from Alberta heavy oils and bitumens are 80.06–86.61, 6.93–8.45, 3.47–8.21, 0.94–2.82, and 0.44–2.61 wt%, respectively. (7) The Ni and V are concentrated in the VR and the asphaltene. For example, while the concentration of Ni and V in Athabasca bitumen is measured to be 65 and 196 ppm, respectively, the n–pentane asphaltene from this bitumen contained Ni and V at 312 and 710 ppm, respectively. (8)

2.1.1.2 Molecular weight

Qian et al. (9) suggested a mean molecular weight of 1238 for a typical asphaltene from field-desorption mass spectrometry with a minimum of 300 and maximum of 3500. There is considerable debate about the maximum limit of asphaltene molecular weight. The range is from 1000 to 10000, while there are published papers which reported the mean value below 1000 and upper limit below 1500. (10) Other authors suggested a more consistent range of 1000 to 2000. (9, 11, 12) Considering the influence of molecular weight on boiling point, claims of lower value are hard to accept. The main difficulty in measurement of this molecular weight is aggregation of asphaltene which makes serious problems in molecular analysis of asphaltene. (1)

2.1.1.3 Molecular structure

Two different views of the asphaltene structure are present in Figure 2-1 and Figure 2-2: the pericondensed or the archipelago structures. The pericondensed model is a core aromatic group containing a large number of fused rings with pendant aliphatic chains. The proposed Yen model by Dickie et al. (13) and modified Yen model by Mullins (14) are focused on pericondensed models.
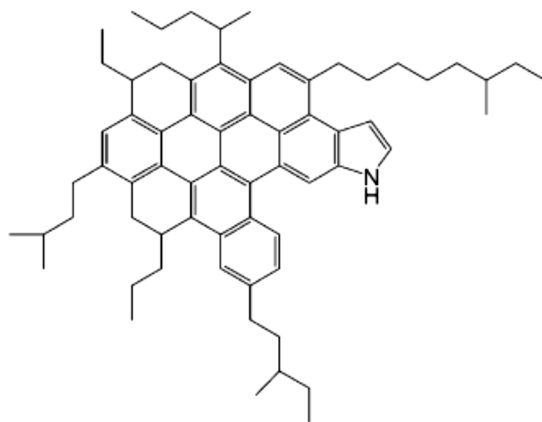
Figure 2-1 Representation of pericondensed model for the molecular structure of asphaltene by Mullins et al. (14)
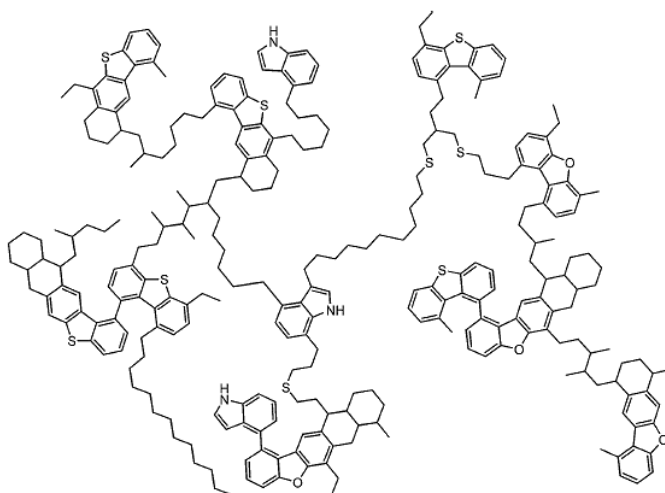
Figure 2-2 Representation of archipelago model for the molecular structure of asphaltene by Sheremata et al.(15)

The archipelago model claims that asphaltenes are composed small ring aromatic clusters connected by aliphatic and sulfur side chains. Sheremata et al. (15) proposed the quantitative molecular representation of asphaltenes as archipelago by Monte Carlo method. This molecular model was consistent with various analysis results; for example, Gray (16) cracked asphaltene under severe conditions and gave wide range of products, which is more consistent with archipelago model than pericondensed model.

Work by Marshall group (17) has used mass spectrometry-mass spectrometry techniques to demonstrate the presence of both large alkylaroamtics and archipelago structures in vacuum residues. Recent results from Karimi et al. (18) and Rueda et al. (19) have established estimated minimum bounds on the mass of archipelago material in asphaltenes. Consequently, the question is not whether complex bridged species are present in the heavy fractions of petroleum, but how much is present for a given feed and for a given extent of processing.

2.1.1.4 Asphaltene aggregation

Since asphaltenes contain various functional groups, the precipitation of asphaltene from oil can lead to a mixture which can form associative interactions

due to both insolubility and the flocculation of colloidal aggregates. (20) Various analytical observations are used to observe the feature of self-associate, including small-angle neutron scattering (SANS), small-angle X-ray scattering (SAXS), vapor phase osmometry (VPO), ultracentrifugation and etc. A wide range of aggregate sizes from dimers to colloidal particles are found in different solution conditions. Therefore the measurement gives different mean size of asphaltene. The consensus suggests that aggregates in the size range of 5-15 nm dominate when asphaltene are dispersed in toluene. (21, 22)

Asphaltene likely associates in solutions through a combination of intermolecular interactions, including π-π stacking, hydrogen bonding and acid-base interactions, resulting in more or less extended aggregates. By adding more n-heptane into toluene solvent, asphaltene aggregate size will become larger (23), which means that good solvents will reduce aggregates size. Asphaltene aggregate size has been shown to reduce as the temperature is raised. (24) At high temperature of 300℃, molecular aggregation of asphaltene was still detected (24) suggesting that aggregates may be remarkably stable in heavy oil and significant in high temperature processing. Another important property of aggregation is that the precipitation of asphaltene can result in the entrapment of material which is ordinarily soluble in n-alkanes.

Asphaltene aggregation has made the characterization of asphaltene difficult since the system might contain both monomers and aggregates. The controversy over asphaltene molecular weight is a good example to show the problem caused by aggregates.

2.1.2 Thermal conversion of vacuum residue and the asphaltenes

2.1.2.1 Free radical chain reaction mechanism

Significant cracking reactions occur for different fractions of crude oil when the temperature is raised above approximately 400 °C. Commercial processes can have a wide range of operation from mild conditions to decrease the viscosity in visbreaking, to severe conditions in order to convert the feed completely to light

gases and olefins in the pyrolysis process. It is believed that regardless of the upgrading process, the chemistry is the same, which involves breaking the chemical bonds of the molecules of the heavy fractions to lighter ones, which are typically accompanied by the formation of gases and coke. (25)

The description of thermal decomposition of n-alkanes by a free radical chain reactions mechanism goes back to the publications of Rice and Herzfeld (26) and Kosiakoff and Rice. (27) The chain of free radical reaction in pyrolysis of n-alkanes in a very simplified form can be written as the following (28):

Initiation:
$$M \xrightarrow{k_1} 2R^{\cdot} \tag{2-1}$$

Propagation:

Hydrogen abstraction
$$R^{\cdot} + M \xrightarrow{k_2} RH + M^{\cdot} \tag{2-2}$$

β-Scission
$$M^{\cdot} \xrightarrow{k_2} R^{\cdot} + A \tag{2-3}$$

Termination:
$$Radical + Radical \xrightarrow{k_3} Products \tag{2-4}$$
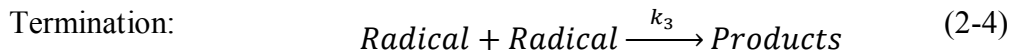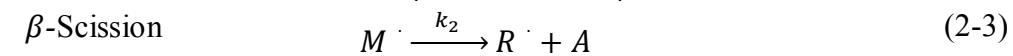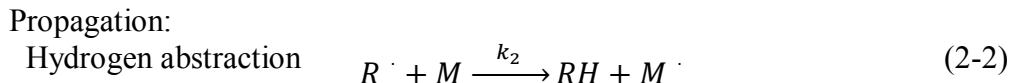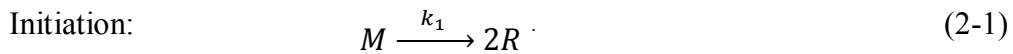
In which M and $M^{\cdot}$ represent the parent alkane and the corresponding radical respectively. RH and $R^{\cdot}$ are the lower alkanes and the corresponding alkyl radicals and A demonstrates an olefin.

LaMarca et al. (29) suggested a mechanism for liquid phase cracking of n-alkanes, and Gray and McCaffrey proposed an extended mechanism accounting for addition reaction, role of hydrogen donor solvent and catalytic reactions. (28) Both of mechanisms are based on free radical chain reactions and are comprised of three steps: initiation, propagation and termination. The latter proposed mechanism is presented in Table 2-2.

Table 2-2 Extended chain reaction mechanism for liquid phase cracking. Hydrogen atoms are omitted for clarity. (28)

Initiation:

$$R\text{-}R' \xrightarrow{k_{in}} R\cdot + R'\cdot \qquad (2\text{-}5)$$

Propagation:

Hydrogen abstraction
$$\beta_j + R_jH \xrightarrow{k_{ij}} \beta_jH + R_j \qquad (2\text{-}6)$$

β-Scission
$$R\cdot\text{-}C\text{-}C\text{-}\beta_j \xrightarrow{k_i} R\text{-}C{=}C + \beta_j \qquad (2\text{-}7)$$

Radical addition
$$R_i + C{=}C\text{-}R_k \xrightarrow{k_a} R_i\text{-}C\text{-}C\cdot\text{-}R_k \qquad (2\text{-}8)$$

Radical rearrangement
$$R\cdot\text{-}C\text{-}C\text{-}\beta_j \xrightarrow{k_s} R_i \qquad (2\text{-}9)$$

Termination:
$$R_i + R_j \xrightarrow{k_t} R_i\text{-}R_j \qquad (2\text{-}10)$$

Olefin removal

Donor Solvent
$$R\text{-}C{=}C + R'H_2 \xrightarrow{k_d} R\text{-}C\text{-}C + R' \qquad (2\text{-}11)$$

Catalytic
$$R\text{-}C{=}C + H_2 \xrightarrow{k_h} R\text{-}C\text{-}C \qquad (2\text{-}12)$$

Aromatic Hydrogenation
$$R' + H_2 \xrightarrow{k_a} R'H_2 \qquad (2\text{-}13)$$
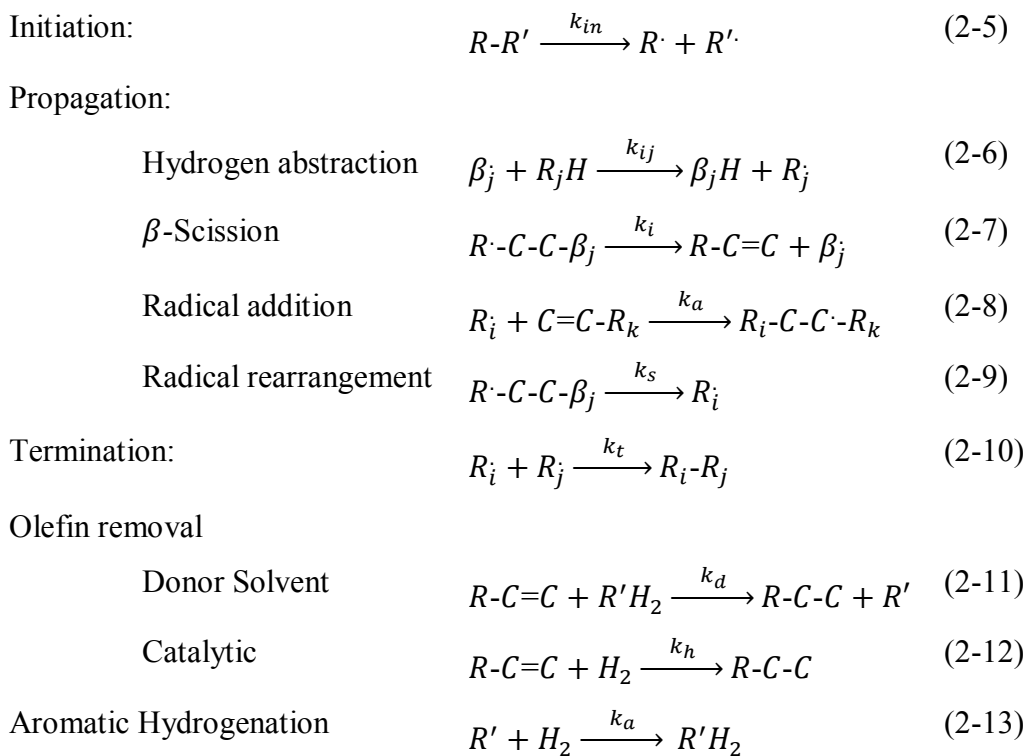
They conclude that β–scission and hydrogen abstraction are important propagation steps for formation of radicals. The aromatic groups would also participate in hydrogen donor–acceptor, or shuttling, reactions but because of their resonance stabilization they do not crack in the range of cracking operations. Cracking of aliphatic radicals via β–scission leads to the formation of another radical and an olefin product. The most abundant products of cracking reactions typically form starting from the most stable radical or crack to give the most stable radical.

The activation energy for cracking in experimental studies (30) showed that the observed activation energy (170-200 kJ/mol) is much less than the chemical bond energy, or bond dissociation energy. The explanation is in the reaction mechanism: Although the initiation step needs very high activation energy to from free radicals, the next steps in the propagation such as hydrogen abstraction and β-

scission have much lower activation energy; therefore the overall activation energy becomes less than the energy required for bond cleavage.

2.1.2.2 Effect of phase in product distribution from cracking

In order to study the mechanism for thermal cracking, n-hexadecane was commonly studied as a model compound by cracking it in both liquid phase and gas phase. Wu et al. (31) studied cracking of n-hexadecane at temperatures of 330-375 °C and compared the results for liquid phase and gas phase. The cracking in both phases followed a first order kinetics with very similar activation energy (290 kJ/mol in liquid phase and 270 kJ/mol in gas phase). However, the product distribution was different. In the liquid phase, alkanes and alkenes were produced with preference on alkanes at high conversion while gas phase cracking always favored alkenes. The yield of gas products from vapor phase cracking was also found to be much higher. This result was consistent with Ford (32) who remarked that the kinetics of liquid-phase thermal decomposition were similar to those of gas-phase thermal decomposition with an activation energy for both of about 257 kJ/mol. He also pointed out that for liquid phase cracking at low conversion, straight-chain alkanes and alkenes have the same selectivity while at high conversion, branched chain alkanes were formed. Based on Ford (32) and Fabuss et al. (33) results, the product distribution of n-hexadecane cracking is strongly reliant on concentration of reactants. In the liquid phase, bimolecular reactions like hydrogen abstraction and addition of olefins are favored while β-scission is dominant in the gas phase.

Khorasheh and Gray (34-37) carried out thermal cracking of n-hexadecane at 13.9 MPa and 380-460 °C in three cases: no solvent, in tetralin and in aromatic solvents. In the absence of solvents major reaction products were C_1 to C_{14} n-alkanes and C_2-C_{15} α-olefins under such a high pressure. The activation energy was estimated to be approximately 256 kJ/mol. Bimolecular reactions (hydrogen abstraction and radical addition) were found to be significant under high-pressure conditions and these addition products were formed:

1. Alkyl hexadecanes in the C_{18} to C_{31} range by addition of parent hexadecyl radicals to α-olefin.

2. Formation of higher n-alkanes by addition of lower primary alkyl radicals to α-olefins including n-C_{15} and n-C_{17}.

3. Addition of lower secondary alkyl radicals resulted in the formation of C_7 to C_{17} branched alkanes.

The addition reactions of the cracked radicals to olefins were significant at higher conversions of n-C16 resulting in the decrease of the observed yields of olefins. These results are consistent with the suggestions of Gray and McCaffrey (28) that olefin formation is essential for obtaining significant yields of larger products, as in coking of VR and asphaltenes, via addition reactions.

In the presence of tetralin, 1- and 2-alkyltetralins were also produced and the distribution of n-alkanes was nearly equimolar due to fast rate of hydrogen abstraction from tetralin. The apparent first-order rate constants decreased with conversion of n-hexadecane. Selectivities for alkanes increased with increase of conversion. Cracking in aromatic solvents also generated biphenyl and higher alkylbenzenes as products. The apparent first-order rate constant increased with initial concentration of n-hexadecane. High initial concentration was discovered to result in high molar selectivities for n-alkanes. The inhibition of cracking rate with these solvents indicated that interactions exist between aromatics and n-hexadecane. This gave an important implication for cracking of bitumen residue which contains both aliphatic and aromatic compounds.

Consequently, the thermal cracking of the asphaltenes for temperatures higher than 350 °C takes predominantly in the liquid phase. Using the observation mentioned above for the reactions in the liquid phase, the asphaltenes molecules are going to crack to produce molecules of different sizes that would make up the liquid oil, but also, would undergo addition reactions to form larger products and eventually coke, as observed experimentally. (25, 28)

2.1.2.3 Reactions of Olefins, Aromatics, Naphthenes and sulfur compounds

In addition to n-alkanes, olefins, aromatics and naphthenes are the other components that their cracking behaviors need to be investigated. Heteroatom components, particularly sulfur compounds such as thiophenes and thioeters, are also rich in asphaltene and vacuum residua and their cracking behavior is important.

2.1.2.3.1 Reactions of Olefins

Olefins do not exist in the crude oil but they will form during operations after undergoing cracking reactions. In general, the β-scission in the propagation step produces one mole of radical and one mole of unsaturated olefin. The radical can continue to participate in the next steps of free radical mechanism while the possible reaction pathways for olefins are: addition reactions with radicals, further cracking and rearrangement. (1) The addition reactions with radicals create larger molecules, which have potential to further polymerization and formation of coke.

$$\text{Radical addition} \qquad R_i + C{=}C\text{-}R_k \xrightarrow{\ k_a\ } R_i\text{-}C\text{-}C^{\cdot}\text{-}R_k \qquad (2\text{-}8)$$
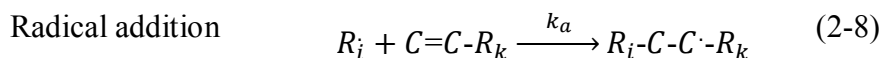
Further cracking of olefin radicals tend to form diolefins. (1) Diolefins proceed with rapid cyclization and aromatization, resulting in coke precursor.

$$(2\text{-}14)$$
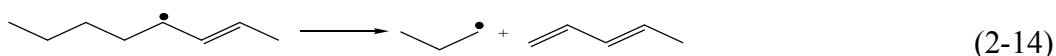
The rearrangement reaction can end up with more stable and less reactive radicals.

2.1.2.3.2 Reactions of Aromatics

The C-C bonds in aromatic compounds are very strong and hard to break due to the resonance stabilization. (1) For instance, benzene and naphthalene have stabilization energies of 6 kcal/mol and 5.5 kcal/mol of C-C bonds, respectively. Therefore, aromatic structures are very stable for thermal cracking at normal conditions and only cracking of side chains and bridges is possible. Zhorov and Volokhova (38) found that presence of aromatic had a hindering effect on thermal cracking. They performed pyrolysis on hexadecane, decalin, naphtha and kerosene gas oil with naphthalene or phenanthrene at temperatures from 800-900 °C and they observed that olefin yields decreased considerably with addition of polyaromatic

hydrocarbons. This was in agreement with results of Khorasheh and Gray (34) who found that cracking of n-hexadecane in toluene and ethylbenzene was slower than cracking of n-hexadecane by itself.

2.1.2.3.3 Reactions of Naphthenes

Naphthenic ring compounds are also found in asphaltene in structures such as cholestanes. Ring opening, isomerization and dehydrogenation are the possible reaction pathways for them in the thermal cracking. Ring opening is an irregular form of β-scission wherein the product of the bond breaking reaction is a single molecule (Gray, 1994). (39) For the reaction of decalin:

(2-14)
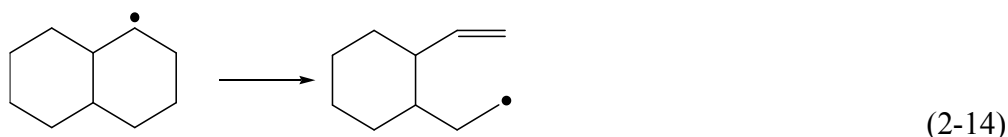
Formation of n-butyl benzene from cracking of tetralin is another example:

(2-15)
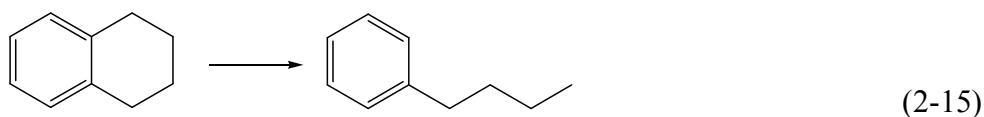
Conversion of tetralin to 1-methyl indane is an example of isomerization.

In the absence of hydrogen, the naphthenic groups can dehydrogenate to form aromatics in thermal cracking condition. In addition, partially hydrogenated aromatic compounds may also go through dehydrogenation and transfer hydrogen to other species. For the reaction of tridecylcyclohexane (40):

(2-16)
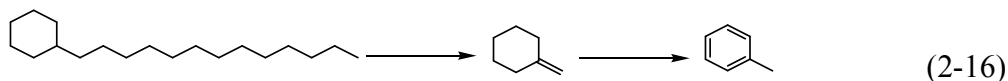
2.1.2.3.4 Reactions of Sulfur Compounds

Compared with other heteroatom compounds, sulfur compounds play an important role in thermal cracking. Thiophenic sulfur is unreactive due to its aromatic structure in thermal cracking, but they are converted in hydrotreatment processes. In other hand, thermal reaction of sulfides is quite favorable, evolving hydrogen sulfide. C-S bonds have a quite low energy of 307 ± 8 kJ/mol compared

with 344 ± 4 kJ/mol for C-C bonds in n-alkanes. (41) The free radical chain reaction mechanism of sulfur compounds is illustrated in Table 2-3.

Table 2-3 Possible reaction pathways for alkylsulfur compounds in residues. (28)

Initiation:	$R_2\text{-}CH\text{-}CH_2\text{-}S\text{-}R' \xrightarrow{k_{in}} R_2\text{-}CH\text{-}CH_2\text{-}S\text{·}+R'\text{·}$	(2-17)
Hydrogen abstraction	$R'_i\text{-}S\text{·}+R_2\text{-}CH\text{-}CH_2\text{-}S\text{-}R' \xrightarrow{k_1} R'_i\text{-}SH+R_2\text{-}C\text{ ·}\text{-}CH_2\text{-}S\text{-}R'$	(2-18)
β-Scission	$R_2\text{-}C\text{ ·}\text{-}CH_2\text{-}S\text{-}R' \xrightarrow{k_2} R_2\text{-}C=CH_2+R'\text{-}S\text{·}$	(2-19)
Decomposition of thiol	$R'_i\text{-}SH \xrightarrow{k'_{in}} R_i^{\,·} + HS^{\,·}$	(2-20)
Hydrogen sulfide formation		
Hydrogen abstraction	$R\text{·}+R_2\text{-}CH\text{-}CH_2\text{-}SH \xrightarrow{k'_1} H_2S+R_2\text{-}C\text{ ·}\text{-}CH_2\text{-}SH$	(2-21)
β-Scission	$R_2\text{-}C\text{ ·}\text{-}CH_2\text{-}SH \xrightarrow{k'_2} R_2\text{-}C=CH_2 + HS^{\,·}$	(2-22)
Hydrogen abstraction	$HS^{\,·}+R_2\text{-}CH\text{-}CH_2\text{-}S\text{-}R' \xrightarrow{k''_1} H_2S+R_2\text{-}C\text{ ·}\text{-}CH_2\text{-}S\text{-}R'$	(2-23)
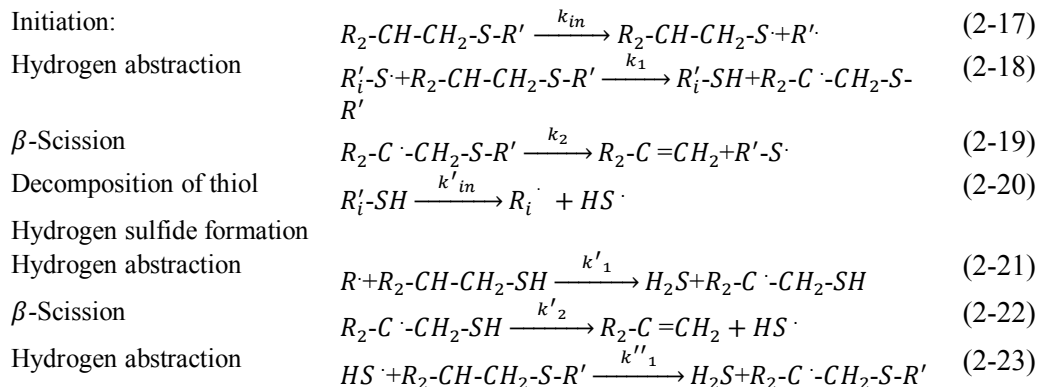
The cracking of sulfides contributes a lot to the conversion of whole hydrocarbon. Furthermore, alkyl sulfides were found to initiate free radical chain reactions.

2.1.2.4 Reactions of Polycyclic Aromatics

There is a vast literature about the thermal cracking of benzene-based compounds which helped to understand the behavior of coals, bitumens, and heavy oils. These heavy resources are also enriched in polycyclic aromatic compounds, and some studies revealed that they may not follow the same reaction kinetics and pathways as the single–ring benzene–based compounds. (42)

Savage et al. (43) found new reaction pathway in thermal cracking of 1-dodecylpyrene (DDP) at mild conditions, 375–425 °C for 10–180 min. The major products in this new pathway were pyrene and dodecane. The abnormality in the formation of this pair was that it requires cleavage of the aryl-alkyl bond in the alkyl chain which is the strongest bond. While the previous studies (44, 45) with alkyl substituted benzene ring compounds showed that cracking happens at β position of side chain and major products are:

- Toluene and an olefin with 1 carbon number less than the side chain
- Styrene and an n-alkane with 2 carbon numbers less than side chain

19

The formation of these two pairs was consistent with energies of the bonds and could be explained completely with free radical chain reaction mechanism.

These strange differences between thermal cracking of the single–ring and multi–ring aromatics motivated Smith and Savage (46-51) to do an inclusive research on reaction products and kinetics of alkylpyrene compounds.

In the primary work of Savage et al. (43), the product distribution from DDP pyrolysis was different in the low and high conversion. At lower conversion, it was similar to the cracking of alkylbenezenes and the two pairs mentioned above.

- 1-methylpyrene and 1-undecene
- 1-ethylpyrene (from the rapid reduction of vinylpyrene), and *n*-decane

Although pyrene and n-dodecane were present in low yields at low conversions, but at higher conversions, they were major products because of significant increase in their yields. The formation of these two products required source of hydrogen which was in agreement with formation of low hydrogen content and insoluble char on the reactor walls. Savage and co-workers tried to explain this hydrogen transfer according to the five mechanisms of hydrogen transfer introduced by McMillen et al. (52) which were concerted hydrogen transfer, reverse radical disproportionation (RRD), H atom elimination-addition, 3 step hydrogen transfer and radical hydrogen transfer (RHT). Therefore, hydrogenolysis reactions via either H atom elimination-addition or RHT were suggested to be responsible for the cleavage of the strong aryl–alkyl bond and formation of pyrene and n-dodecane.

In the next studies, Smith and Savage (46) probed the selectivity to cleave the methyl groups in 1,6-dimethylnaphthalene when reacted with DDP to find that which mechanism is responsible for cleavage. H atom elimination-addition is a non–selective reaction while the RHT is more selective. The results showed that the mechanism responsible for the cleavage is more selective than H atom elimination-addition.

Continuing these studies, Smith and Savage (47) performed the pyrolysis of 1,3-bis(1-pyrene)propane (BPP) in the presence of 1,6-dimethylnaphthalene, which resulted in the cleavage of the strong aryl–alkyl bond to give pyrene and 1-propylpyrene by a selective mechanism such as RHT or molecular disproportionation. Their proposed pyrolysis pathway for BPP is illustrated in Figure 2-3.
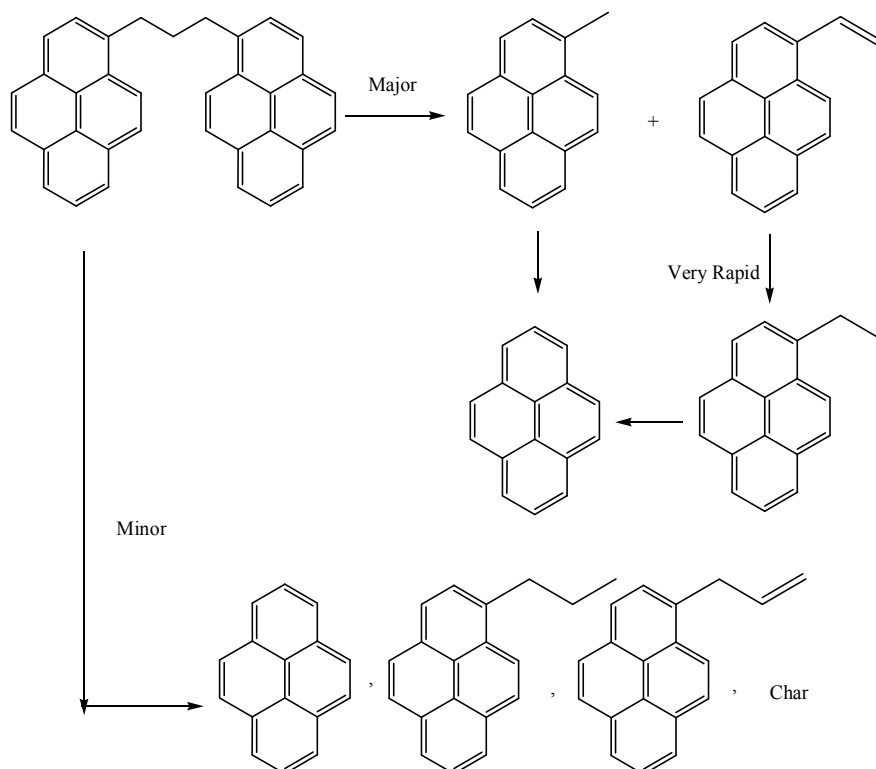
Figure 2-3: Pyrolysis pathway of BPP by Smith and Savage, Reprinted with permission from (SMITH C, SAVAGE P. REACTIONS OF POLYCYCLIC ALKYLAROMATICS .2. PYROLYSIS OF 1,3-DIARYLPROPANES. ENERGY FUELS. 1991;5(1):146-55). Copyright 1991 American Chemical Society.

To identify the actual mechanism responsible for the hydrogenolysis and cleavage of the strong bond, Smith and Savage (48) in the next level of study, investigated the reactions of 1-methylpyrene, which cannot give RHT, and 1-ethylpyrene at 400–450 °C in a batch reactor for up to 300 min. This study showed that RRD was responsible for the dealkylation in 1-methylpyrene to form pyrene, while in the pyrolysis of 1-ethylpyrene both of RRD and RHT were the functional mechanisms.

In kinetic modeling for DDP, results showed that RRD was dominant only at the beginning of the reaction, while the RHT was found to be the main hydrogenolysis mechanism after that, and the H atom elimination-addition mechanism did not describe the observations by itself. (51, 53)

These studies was followed by Freund et al. (54) to have a more accurate clarification about the breakage of strong alkyl-phenyl bonds and to find the source of hydrogen transfer. They used an open reactor for flash thermolysis of 1,20-di(1-pyrenyl)eicosane at 400-500 °C. Similar side-chain cracking to alkylpyrene compounds of Smith and Savage was observed and RHT mechanism was introduced as the most likely mechanism for transfer of H atom. Formation of stable phenalenyl radicals eased the cleavage of alkyl groups after hydrogen transfer. This was addressed by Smith and savage as well. (50)

Freund et al. (54) identified an internal olefin that is next to the pyrene group using ^{1}H–NMR spectroscopy. This olefin was suggested as the possible source of the RHT hydrogen transfer. The proposed RHT mechanism by Freund et al. is presented in Figure 2-4.
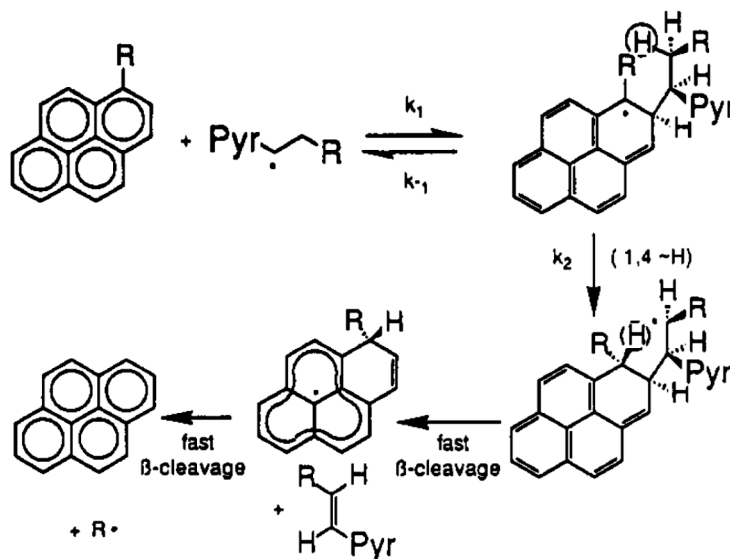
Figure 2-4 The mechanism of RHT hydrogen transfer in the cracking of 1,20-di(1-pyrenyl) eicosane Reprinted with permission from (FREUND H, MATTURRO M, OLMSTEAD W, REYNOLDS R, UPTON T. ANOMALOUS SIDE-CHAIN CLEAVAGE IN ALKYLAROMATIC THERMOLYSIS. ENERGY FUELS. 1991:5(6):840-6). Copyright 1991 American Chemical Society.

Using the data of Freund et al. for the formation of internal olefin, the char materials were present in the work of Savage et al. (43) probably formed by addition reactions of these olefins as suggested later by Gray and McCaffrey (28).

The most vital conclusion from these studies by Savage and co-workers and Freund and co-workers was that cracking of side chains on polycyclic aromatic is more possible with the hydrogen transfer mechanism. Hence, the same structures are present in the asphaltene cracking, similar reaction pathways and cracking kinetics during thermal upgrading processes are feasible. These authors did not consider the addition reactions. Because of high molecular weight of model compounds, thermal cracking would happen in the liquid phase and addition reactions are more favorable in this condition (35), so significant yield of addition products is possible while no attempts were made to quantify them but formation of char and insoluble materials in both studies is the most obvious evidence for formation of complex addition products. For Smith and Savage work (51), the yield of char and other unidentified products increased at higher conversions and at maximum, it was around 40 wt %.

2.1.2.5   Coke Formation

Coke can be defined as carbonaceous solid that is formed during thermal reaction of carbon-rich materials. Coke formation is undesirable because loss of a portion of feed into an invaluable by-product which can't be used as transportation fuels. Also it affects the yield of liquid products in upgrading processes of heavy oil as well as the operability of these processes However; it forms inevitably during the thermal cracking operations. Understanding about the mechanism of coke formation would help to find ways for its suppression.

2.1.2.5.1   Formation of coke by liquid-liquid phase separation

Wiehe (55) suggested a model based on the separation of new phase for formation of coke. This mechanism involves liquid-liquid phase separation in which the new phase is lean in hydrogen. In thermal cracking, aromatic cores lose hydrogen rich bridges and when these components reach a critical concentration, phase separation happens followed by rapid cross linking reactions. This model

linked the molecular weight and hydrogen content of components to define solubility zones. Asphaltenes are located in the middle zone (toluene soluble and n-heptan insoluble) and by passing the limits of this solubility zones according to the mechanism mentioned above, coke would form. These solubility zones and limit of coke formation is illustrated in Figure 2-5 after Wiehe.
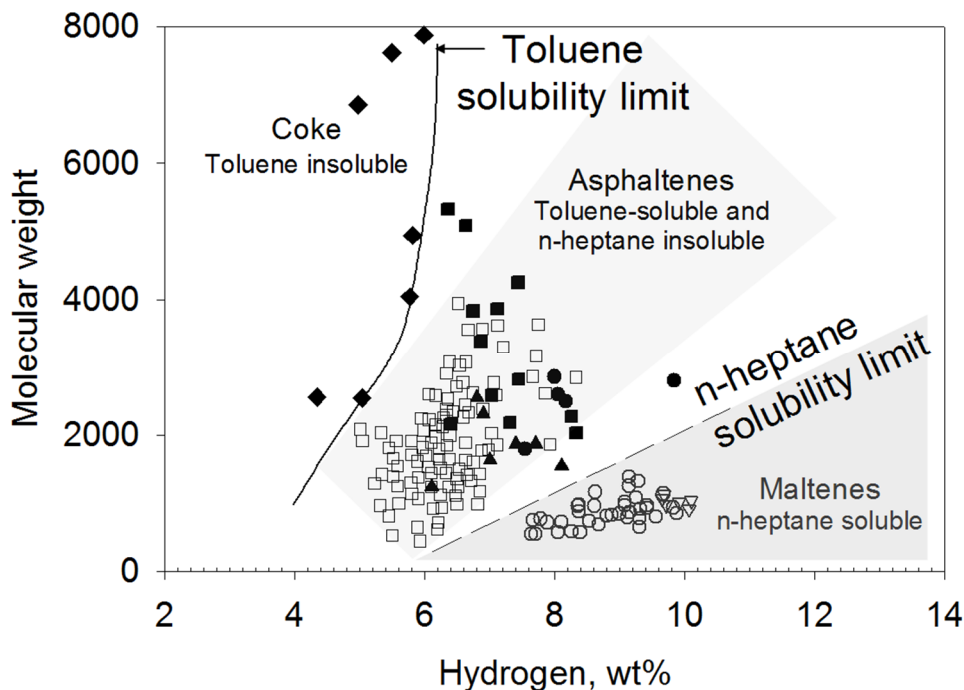
Figure 2-5 Solvent resid phase diagram by Wiehe (55)

2.1.2.5.2 Formation of coke by addition reaction

Wiehe's model does not consider the contribution of addition reactions through free radical chain reactions on the yield of coke.

Khorasheh and Gray (35) stated that olefins could undergo addition reactions in the liquid phase thermal cracking of n-hexadecane at high pressure (13.9 MPa) and a temperature range of 380 to 450ºC. These addition products of the olefins could be continued and by further polymerization that would generate larger molecules with higher molecular weight or coke. Gray and McCaffrey (28) suggested that a reasonable mechanism for coke formation from hydrocarbons is free-radical chain polymerization following by rearrangement to give a more thermally stable product.

More recently, Alshareef et al. (56) studied addition reactions in thermal cracking of heavy oils in liquid phase. They selected a series of model compounds for the large components in petroleum. Thermal cracking in liquid phase in all cases of their studies gave significant yield of addition products larger than the starting compounds ranging from 26 to 62 wt%. They reported that the molecular structure of the addition products were consistent with addition reactions between alkyl groups rather than the formation of aryl-aryl linkages or larger fused-ring products. Their results will be mentioned in details in the next section.

Formation of these higher molecular weight compounds facilitates phase separation mechanism by increasing molecular weight at almost same hydrogen content and it will cross the limit of coke formation in Wiehe's diagram. Therefore, now it is believed that either one of these mechanisms or any combination of them is responsible for formation of coke during industrial processes.

2.1.2.6 Cracking of asphaltene model compounds

Molecular analysis of asphaltene by mass spectroscopy techniques is impossible due to its tendency to form aggregates in solution and the wide range of compounds that are present in this solubility class. (20) Further, a variety of cracked products are obtained from reaction, and these are extremely difficult to characterize. Therefore, it is difficult to optimize conditions, to sort out desired processes, and to obtain meaningful information about catalyst activity and selectivity using actual asphaltene. One possible alternative is the use of simple compounds as reactant to model reactions of importance in asphaltene upgrading to simulate its physical and chemical behaviors.

Alshareef et al. (56-58) investigated cracking and coking reactions of asphaltene model compounds extensively. Their results revealed vast information about the nature of cracking of large model compounds in the liquid phase as well as addition products and their structures. In the first step of their work, kinetics of cracking and coking of two pyrene base model compounds were studied by TGA and microreactor experiments at 400°C. (57) The structures of these two model compounds were shown in Figure 2-6
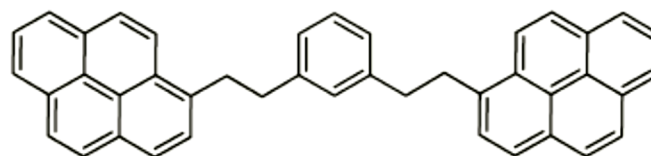
1,3-bis(2-pyren-1-yl-ethyl)-benzene (P-*m*PhP)
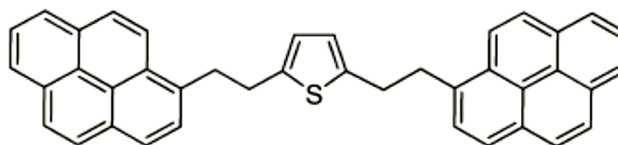
2,5-bis(2-pyren-1-yl-ethyl)-thiophene (PThP)

Figure 2-6 Asphaltene model compounds used by Alshareef for measurement of cracking kinetics (57)

Then in the next step, they studied formation of archipelago structures in the thermal cracking of three types of compounds: alkyl pyrene, alkylbridged pyrene with phenyl or pyridine as a central ring group, and a substituted cholestane-benzoquinoline compound in the molecular weight range of 534 to 763 g/mol. (56) The experiments were conducted in a microreactor, in the liquid phase at 365-420°C and they showed selectivity and nature of the addition products in the cracking. Figure 2-7 shows the suggested structures and molecular weights for addition products.

Mass of parent compound: 763.31 g/mol	**Mass of parent compound:** 534.69 g/mol	**Mass of parent compound:** 702.06 g/mol
Mass of addition product: 1384 m/z	**Mass of addition product:** 866 m/z	**Mass of addition product:** 1402 m/z
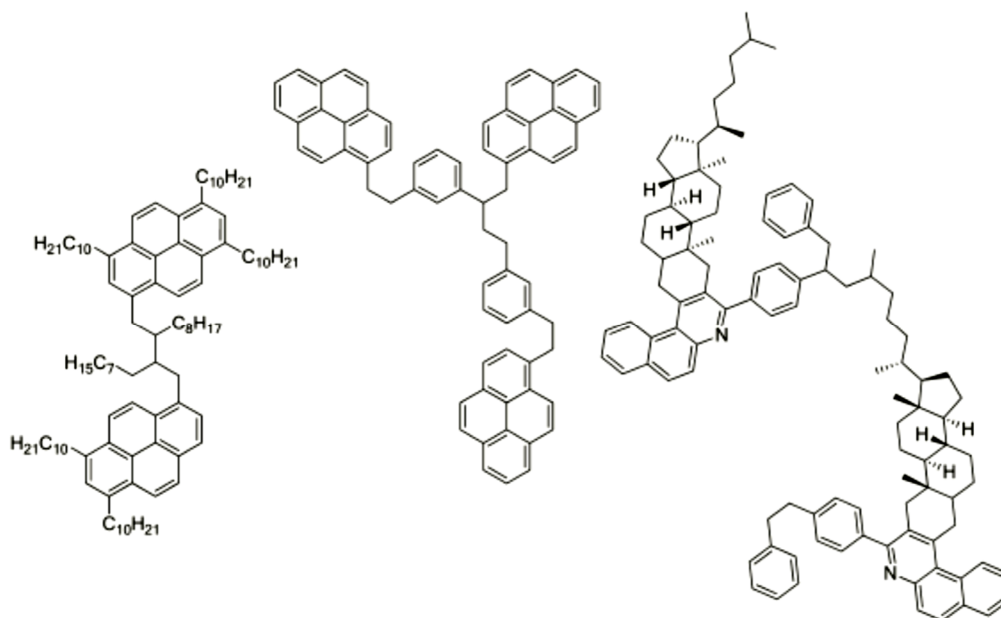
Figure 2-7 Suggested structures for major addition products of asphaltene model compounds (56)

They observed that all of model compounds gave significant yields of addition products ranging from 26 to 62 wt % when cracking in the liquid phase. The NMR studies of products samples showed that addition reactions happened between alkyl bridges groups rather than aryl-aryl or larger fused ring products.

To investigate about the effect of chemical structure on the cracking and coking behaviors, next set of experiments included TGA and microreactor studies of a series of pyrene based model compounds consisting three island molecules in which an aromatic of heteroatomic group was joined to two pyrene groups by ethano bridges.(58)

The most likely mechanism for these processes includes a sequence of free-radical addition reactions to an unsaturated bond, followed by rearrangement, dehydrogenation, and further cracking. Figure 2-8 presents three major cracked

pairs found in the microreactor experiments. The central island could be a hydrocarbon or heteroatomic group.
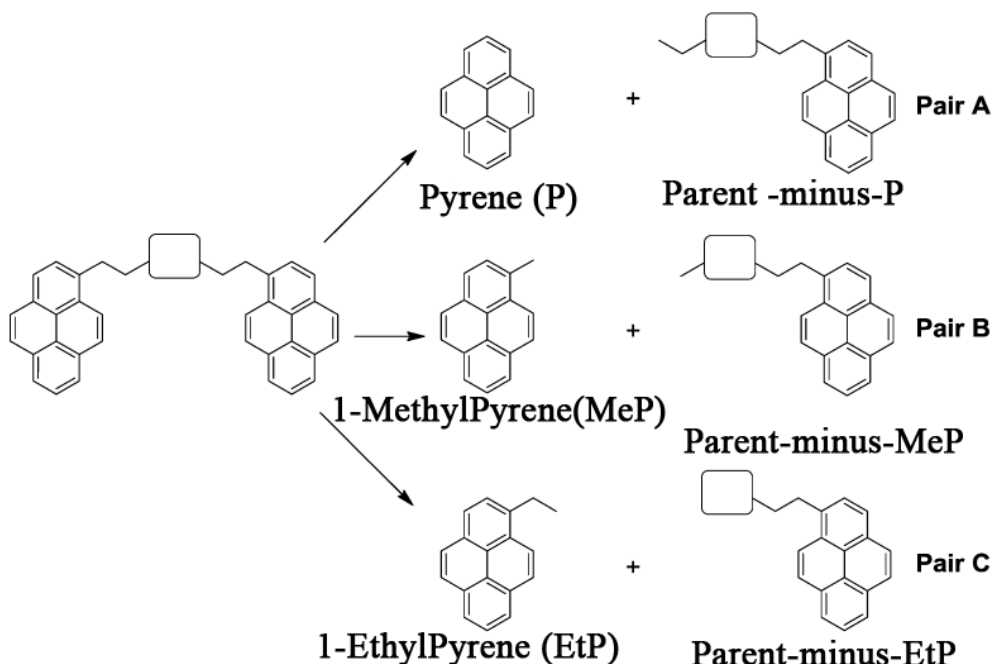
Figure 2-8 Three major pairs of cracked products in microreactor experiments (58)

The change in the central ring in the model compounds had major impact on both the cracking and coking. Compounds with heteroatoms incorporated in the central ring typically gave higher yields of coke and different selectivity of the cracked products, compared to hydrocarbon compounds. For example, replacing the benzene ring with a pyridine group increased the coke yield significantly. They concluded that coke yield of pyrene model compounds is controlled by the activity of the parent compound, the rate of addition reactions, and the nature and activity of cracked and addition products. Also binary experiment with addition of benzopyrene to model compound in reactor confirmed that aryl−aryl addition is not a favorable reaction and is much slower than cracking under the employed conditions. Alkyl−alkyl and alkyl-aryl additions are much faster, despite cracking reactions, and are dominant in building larger product molecules.

2.1.2.7 Relevant catalytic reactions

Catalysts have three main purposes in the upgrading of vacuum residue and asphaltene:

1) Hydrogenation of aromatics and olefins, which is critical for suppression of coke formation as discussed before.

2) Removal of metals content, particularly vanadium and nickel

3) Removal of sulfur, nitrogen and oxygen

Because of high tendency of coke formation in cracking of vacuum residue and asphaltene, use of catalysts for cracking reaction is not economical. Aromatic rings can be hydrogenated in the presence of catalyst and hydrogen gas. The larger size of aromatic groups, the better reactivity for hydrogenation is observed due to high stability of smaller size groups. In the hydrogenation of olefins, catalyst can supply hydrogen to form saturated bonds and prevent coke formation. (59) Sulfur, nitrogen and oxygen content of heavy oil feeds can be reduced by using hydrotreatment catalysts, removing H_2S, NH_3 and water respectively as the by-products of these reactions. (60) For demetallization reactions, nickel and vanadium are converted to their sulfide form and can block in the pores of catalysts. Hydrocracking of the heavy oils with acidic zeolite catalysts can be done after removing their basic nitrogen content. (39) Although acid-catalyzed cracking is a major process in petroleum refining, this type of reaction is ineffective with the high nitrogen contents of vacuum residues.

According to the definition, role of catalyst in a reaction is decreasing the activation energy and introducing new pathways for reaction to occur. Catalytic reactions are following these steps:

1) Diffusion of reactants from bulk of fluid to the active site which can be an ionic compound, metal particles supported on a surface or a chemical compound
2) Coordination of the reactant with catalyst active sites
3) Chemical reaction at the sites

4) Transport of products and unreacted reactant to the bulk

Different transition metals such as iron, nickel, cobalt, molybdenum, tin and tungsten are active for hydrogenation reactions. (61) These metals are active in sulfide as well as metallic form. The activity of metal sulfide catalysts depends on the three major factors: the type of metal, surface area of active site and presence of alloyed metals. (39) One general way to increase the surface area is to use supported metal sulfides on high surface area supports such as γ-alumina.

The catalysts are selected based on their activity and cost. Conventional industrial hydrotreatment catalysts are mixtures of Co and Ni with Mo supported on alumina. To reduce pressure drop in the fixed beds, they are formed into pellets and beads. Ni and Co in the crystalline structure of Mo sulfide for the hydrogenation act as promoters. (60) In the Figure 2-9 catalytic mechanism of hydrodesulfurization of dibenzothiophene is illustrated. Hydrogen gas can adsorb dissociatively on the surface and if it reacts with the sulfur on the surface, the resulting vacancy can adsorb an organic sulfur compound like dibenzothiophene to gain a sulfur atom from it.

These catalysts get deactivated by deposition of nickel and vanadium sulfide from feed and also by coke formation.
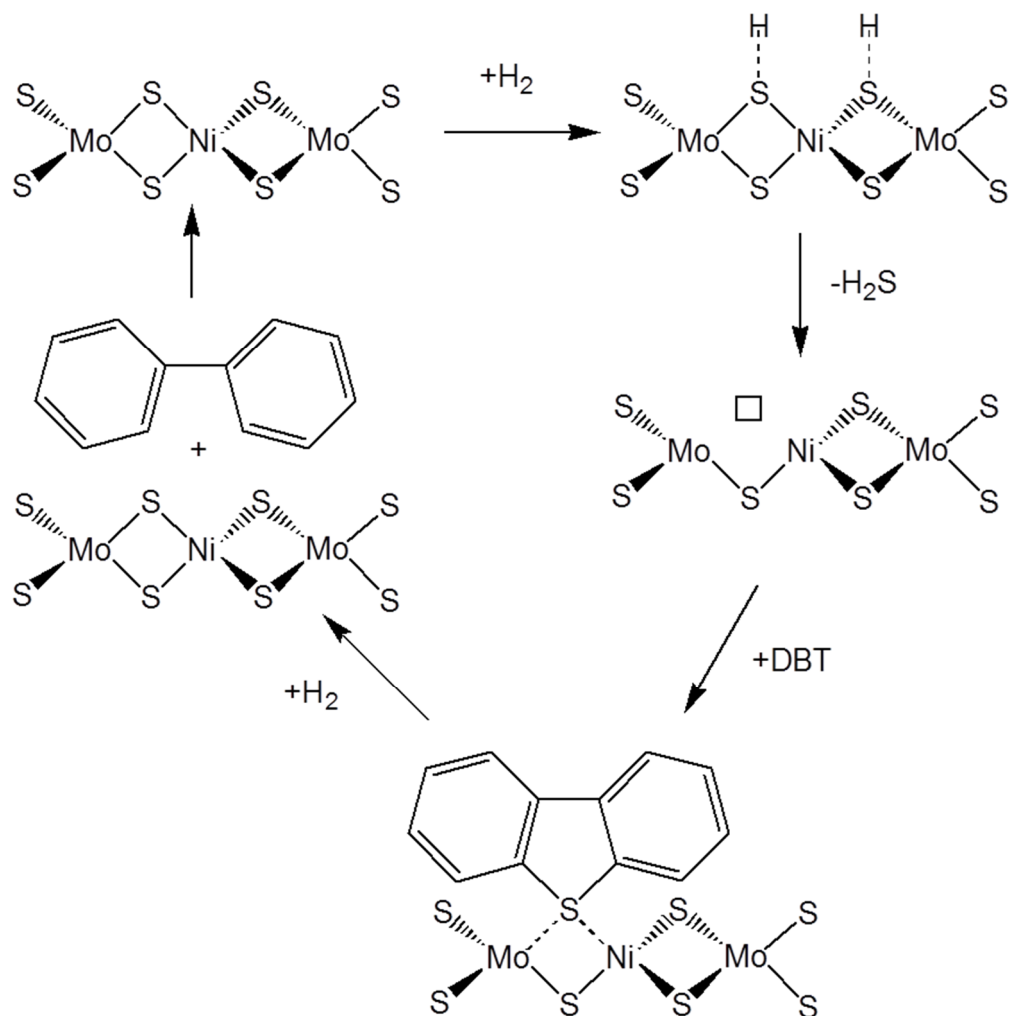
Figure 2-9 mechanism for hydrodesulfurization of dibenzothiophene on Ni-Mo sulfide (62)

Figure 2-10 shows how temperature, hydrogen partial pressure and catalyst activity can change the reaction pathways of thermal and catalytic cracking. Generally, increasing temperature, lowering hydrogen pressure and using catalyst with low activity would direct reaction from hydrogenation toward dehydrogenation and coking. (39)
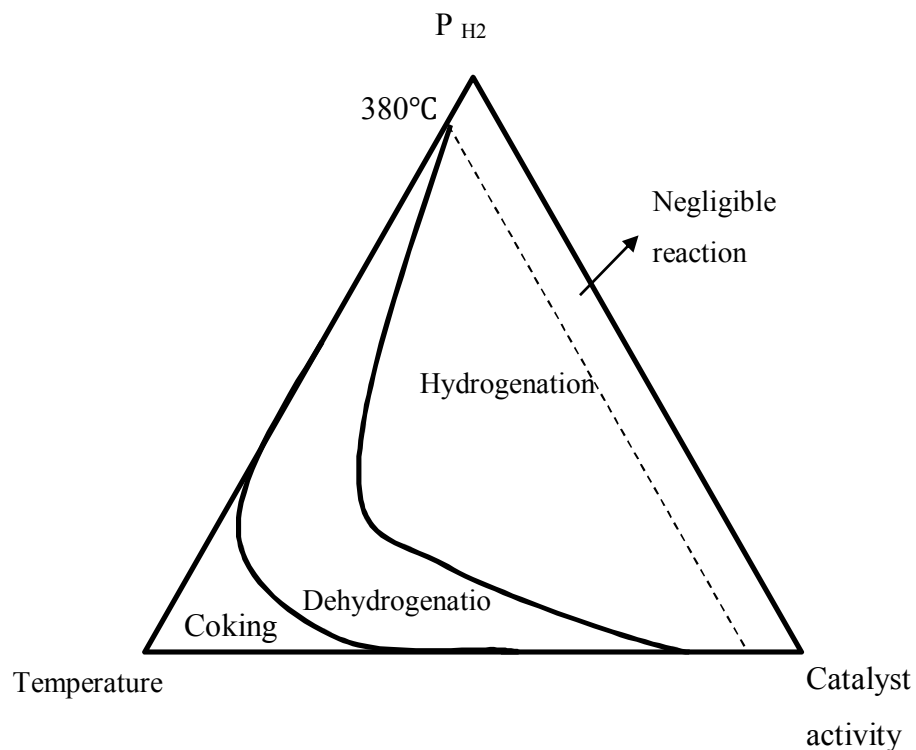
Figure 2-10 Regions of operation for thermal and catalytic reactions and the affecting factors (39)

Song and Yoneyama (63) investigated highly active unsupported Mo sulfide catalyst from decomposition of ammonium tetrathiomolybdate (ATTM) in an organic solvent for hydrogenlysis of 4-(1- naphthylmethyl)bibenzyl (NMBB). The chemical structure of NMBB is shown in Figure 2-11.
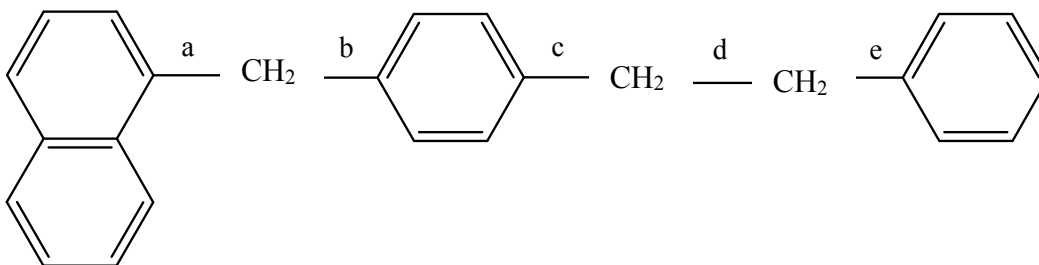
Figure 2-11 Chemical structure of NMBB

In the presence of catalyst, naphthalene and 4-methylbibenzyl were the major products indicating the cleavage of alkyl-aryl C-C bond (a) while for non-catalytic

runs, toluene and 1-(p-tolylmethyl)naphthalene were major products which resulting from cleavage of weakest alkyl-alkyl C-C bond (d). They concluded that catalyst changed the reaction pathway by shifting the mechanism from thermal cracking to hydrogenolysis of bond (a). The suggested mechanism for cleavage of bond (a) was because of its higher electron density in the highest occupied molecular orbital, the naphthyl group in NMBB should be adsorbed preferentially on the surface of the catalyst. Then the dissociatively adsorbed hydrogen on the catalyst surface attacks on ipso position in naphthalene ring (the carbon connected to methylbibenzyl group), leading to the cleavage of bond (a) and the formation of naphthalene and methylbibenzyl; whereas, non-catalytic (thermal) reactions of NMBB involves homolytic cleavage of bond (d), and thus generated radicals can react with gas phase hydrogen (at a much lower rate) to form toluene and 1-(p-tolylmethyl) naphthalene. In our study, the possibility of hydrogenolysis is investigated in the result and discussion chapter.

2.1.2.7.1 *Hydrogenation of olefins*

Although the hydrogenation of sulfur compounds and aromatics gains the most attention in the literature for metal sulfides, some works report on the reactions of olefins. Wiesser and Landa (61) reviewed the properties and applications of metal sulfide catalysis. For the hydrogenation of ethylene, MoS_2 and WS_2 were efficient catalysts. (64) Heavier olefins like 1-octene can be hydrogenated on WS_2-NiS catalyst. (65) Hydrogenation at higher temperatures (more than 400°C) was accompanied by skeletal isomerization. (66)

2.1.2.7.2 *Iron sulfide catalysts in upgrading of oil and coal processing*

Iron catalysts are usually used as powdered or impregnated additives due to their low cost so it can be used without recycling. For example, formation of iron sulfide from in situ sulfidation of iron oxide is one of the famous processes for hydrogenation reactions. But iron sulfide has been known for a long time as catalyst for coal liquefaction. Liu et al. (67) introduced a new in situ impregnation method for preparing iron based catalyst for direct coal liquefaction in which ferric sulfide from reaction of ferric chloride and sodium sulfide produced pyrite and pyrrhotite

and it enhanced the yield of liquid products. Later Hirano and Kanda (68) investigated the natural iron compound for bituminous coal liquefaction and they provided higher yield under mild reaction condition by transferring hydrogen quickly to thermal cracked fragments to stabilize them. They also showed pyrrhotite is the active phase for those reactions.

Rueda et al. (19) studied the presence of different pendant groups by cracking of asphaltene in conditions that minimized side reactions and maximized conversion of vacuum residue to distillates using an iron-based catalyst supported on coal (Ranganathan et al.(69)) with a modest activity to suppress the formation of coke, while exhibiting low activity toward hydrodesulfurization and hydrocracking. The data indicated that iron sulfide could diminish yield of coke formation without hydrogenation of aromatics.

In addition different model compounds have been used to study role of iron catalysts in direct coal liquefaction: The sulfur hydrogenolysis of benzothiophene was used by Guin et al. (70) to study activity of pyrite. Kamiya et al. (71) examined hydrogenation of phenanthrene and cracking of trans-stilbene to study the effect of coal minerals in direct coal liquefaction. Ogawa et al. (72), Hei et al. (73), and Sweeny et al. (74) used the hydrocracking reaction of diphenylmethane to study the H_2-H_2S-pyrrhotite interaction. Ogawa et al. (72) indicated that pyrite is a more active promoter of coal liquefaction than pyrrhotite under H_2 and that pyrite formation from pyrrhotite increases with increasing H_2S pressure. Montano et al. (75) studied the hydrogenation of diphenyl ether in the presence of pyrrhotite and H_2. More recently, Chadha et al. (76) used phenanthrene, diphenylmethane and cumene to study the activity and selectivity of ferric-sulfide-based catalyst for hydrogenation, hydrocracking and catalytic cracking respectively.

Considerable research has also been applied to determining the active phase of the iron catalyst. It is generally accepted that the sulfided form of the catalyst exhibits a higher activity than the oxide phase for coal liquefaction. (77) While the addition of pyrite is known to result in higher conversions and selectivity to oils, studies have shown that, under hydrogenation-liquefaction conditions, pyrite

decomposes to form pyrrhotite with the evolution of hydrogen sulfide. (78, 79) Some researchers have proposed that pyrrhotite is the active phase of the catalyst (77-79) while others have suggested that the hydrogen sulfide evolved during the decomposition of pyrite is responsible for the catalytic activity. (80) Subsequent studies have concluded that both hydrogen sulfide and pyrrhotite are necessary for high catalytic activity. (74) Other researchers have suggested that the active phase of the catalyst is a reduced form of α-Fe which exists as a short-lived intermediate on the surface which is subsequently resulfided. (81, 82) The active form of the iron-based catalysts is still a matter of considerable debate. If iron species react by mechanisms analogous to the better-studied Mo-sulfides, then edge sites will be important for hydrogenation reactions, providing a suitable electronic environment for hydrogen chemisorption and adsorption of hydrocarbons, while vacancies in the sulfide surface will be important for reactions of sulfur compounds. (83, 84)

2.1.3 Hydroconversion and hydrotreating processes in industry

If high temperatures over 410 °C used to cleave the chemical bonds of the molecules of a heavy feed, the process called hydroconversion. Hydrogen in the presence of catalyst is used to hydrogenate aromatics and remove sulfur as well as suppressing coke formation. The objective is to convert low grade materials into lighter and more valuable products. On the other hand, hydrotreatment includes the use of milder temperatures below 410 °C to catalytically remove sulfur and nitrogen, as well as the hydrogenation of olefins and aromatics. Another objective of hydrotreatment is the removal of metals by generating metal deposits in catalyst pores. Here the thermal reactions are not favorable and the objective of hydrotreating processes is to reduce sulphur and nitrogen content in liquid products, and transform them to hydrogen sulfide and ammonia. The detailed explanations of these two processes are presented in the following sections.

2.1.3.1 Hydroconversion

Fixed bed reactors, catalytic ebullated bed, and slurry or additive-based processes are the current three types of hydroconversion processing technology.

2.1.3.1.1 Fixed Bed

Fixed bed reactors are easy to operate and have advantages for scale-up. Figure 2-12 shows the schematic diagram of a conventional fixed bed hydroconversion unit. Typical operating parameters for fixed-bed processing, in this case, atmospheric residue desulfurization, can be found in Table 2-4. Their disadvantages is deposition of minerals and metals on the catalysts pellets, which would result in a pressure drop along the reactor bed and shut downs are inevitable. The metal content to have an acceptable catalyst life should be less than 250 ppm; therefore the hydroconversion of many vacuum residue and asphaltenic feeds are not feasible with this process. However, some modifications have been made to provide possibility of dealing with higher metal content: On-line catalyst replacement by Chevron's OCR process, which has the countercurrent flow of residue and catalyst and Bunker reactor technology by Shell to remove the spent catalysts from the bottom of the reactor and fresh catalyst added at the top. Consequently, catalyst slowly moves downward through the reactor. (1)
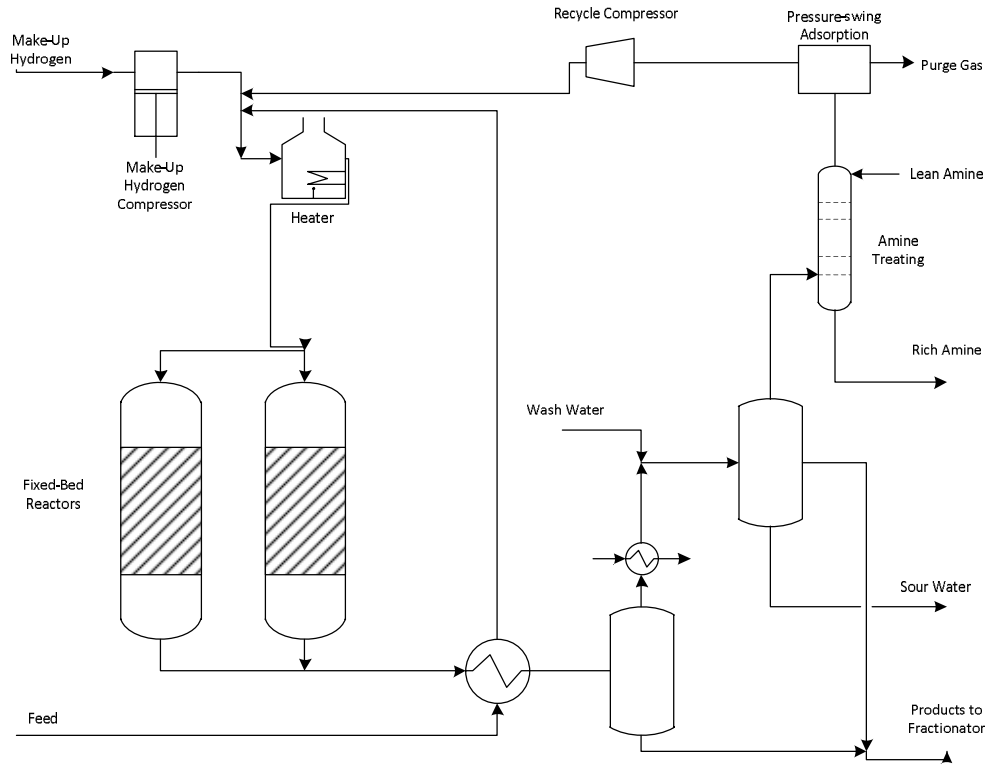
Figure 2-12 Schematic diagram of a conventional fixed-bed residue hydroprocessing unit (85)

Table 2-4 Operating parameters for a typical fixed-bed process (86)

Operating Parameter	Operating Range	
Temperature	370-440	°C
H_2 Partial Pressure	8-13	MPa
LHSV	0.2-0.5	h^{-1}
H_2 Consumption	100-175	Nm^3/m^3

LHSV = Liquid volumetric flow rate at 15 °C (ft^3/h)/Volume of catalyst (ft^3)

2.1.3.1.2 Catalytic Ebullated Bed

Fluidization of supported catalyst pellets is an alternative means to prevent the plugging of the reactor by deposited metals and minerals. In a typical ebullated bed reactor a mixture of hydrogen gas and liquid feed enter at the bottom of the

37

reactor and flow upward through the expanded catalyst bed. Hydrogen, liquid products and hydrocarbon vapours exit from the top of the reactor while a recycle stream of liquid is drawn down a tube and pumped to a distributor at the bottom of the reactor. The energy required for expansion of the bed is provided by the flow rate of the recycle stream, which can be up to 5–10 times that of the feed rate. Hydrogen gas is recycled at 3–4 times the consumption rate to keep hydrogen in excess in the liquid phase. Fresh catalyst is added continuously at the top of the reactor to maintain operating temperature and constant conversion. The general parameters for ebullated bed operation are given in Table 2-5.

Advantages for the processing of heavy residues and bitumen feeds include: the expanded bed prevents clogging of the reactor by solids, the liquid recycle ensures good mixing within the reactor, because of continuous withdrawn of catalyst, long operations can occur without shutting down. (1)

Table 2-5 Operating parameters for a typical catalytic ebullated bed process (86)

Operating Parameter	Operating Range	
Temperature	420-450	°C
H_2 Partial Pressure	10-15	MPa
LHSV	0.1-1.5	h^{-1}
H_2 Consumption	150-300	Nm^3/m^3

LHSV = Liquid volumetric flow rate at 15 °C (ft^3/h)/(Volume of catalyst (ft^3))

2.1.3.1.3 *Slurry or Additive Based Processes*

In these processes, finely divided additives are added to the feed and are circulated within the reactor. They enhance catalytic activity of the reactor and leave the reactor with unconverted. The objective of these additive processes is to maximize the conversion of residue with minimum coke formation and hydrodesulfurization, hydrodenitrogenation, hydrodemetallization, and cracking will be conducted in next steps. Therefore emphasis is on choosing the type and

amount of additive to control coke formation in the reactor and this selection is restricted with cost of additives. Examples are: powdered coal impregnated with iron salts, iron oxide waste, and organometallic compounds such as molybdenum naphthenates.

Since the reactive phase consists of slurry or suspension of finely powdered catalyst, a flow tubular reactor, where a liquid suspension of additive flows upward with hydrogen gas can be used. Table 2-6 summarizes some of the processes presented in literature based on laboratory, pilot and demonstration plants. None of the processes have been commercialized and all the pilot and demonstration units used tubular reactors. (1)

Table 2-6 List of various slurry hydroconversion processes (1)

Process	Company	Catalyst	Conditions	Reference
Combi Cracking	Veba Oil	Fe_2O_3	200bbl/d, 440-490°C, 15-25 MPa	Niemann et al., 1988
CANMET Hydrocracking	CANMET	$FeSO_4$	5000bbl/d, 430-440°C, 24 MPa	Pruden et al., 1989
HDH	PDVSA	Dispersed Mo	200bbl/d, 420-480°C, 14 MPa	Marzin et al., 1988

2.1.3.2 Hydrotreatment

Selective removal of heteroatoms from the feed with negligible cracking of hydrocarbons is the purpose of hydrotreatment. In other words, in hydrotreatment the quality of products is improving to meet the specifications required downstream units. The chemistry involved in hydrotreatment includes: desulfurization, denitrogenation, deoxidation, hydrogenation of chlorides, hydrogenation of olefins, hydrogenation of aromatics, hydrogenation of organometallic compounds and

deposition of metals, and coke formation. Figure 2-13 shows the schematic of a conventional hydrotreating process called diesel hydrotreating.
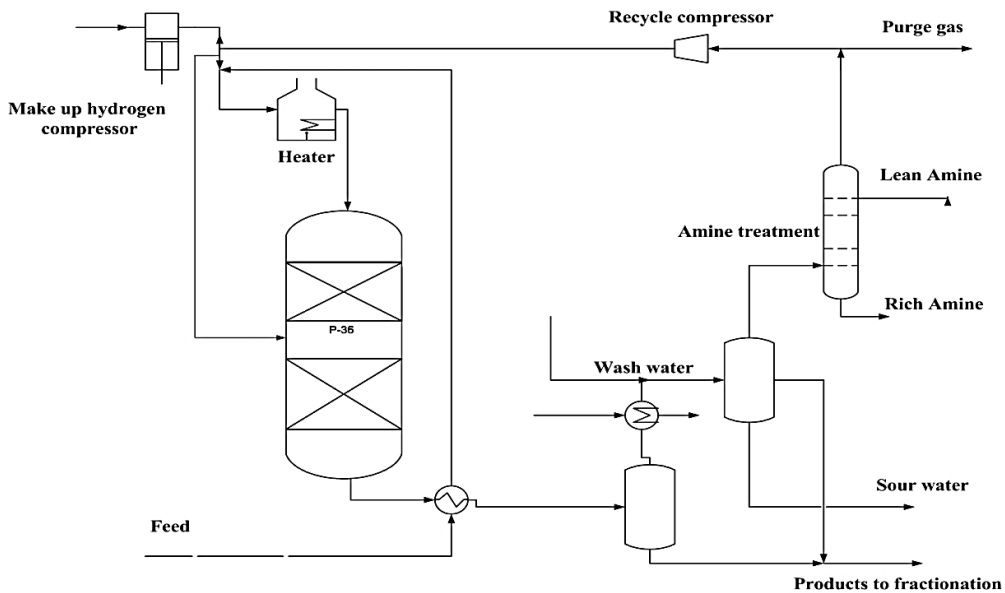
Figure 2-13 Fixed bed hydrotreating process for distillates (1)

Feed is mixed with hydrogen gas and heated to reaction temperature by a furnace and then introduced to the top of a fixed bed reactor, which typically operates with liquid feed flowing downward over solid catalyst co-current with hydrogen gas. Catalyst used is usually Co-Mo or Ni-Mo on γ-alumina comprised of 11-14 wt % Mo and 2-3 wt % of the Ni or Co promoter. Surface areas of the catalyst range from 150-200 m^2/g giving high dispersion. The catalyst is present in the reactor as extruded cylinders (~2 mm diameter), lobed cylinders, or rings. Catalyst can often be regenerated in situ and then ultimately replaced after several regenerations. Reactor effluent is passed through a gas-liquid separator, where a hydrogen enriched gas is separated and recycled. Addition of cold make-up hydrogen gas at an intermediate point along the reactor controls both temperature and hydrogen partial pressure of the process. Similar issues for fixed bed operation in hydroconversion processes also occur in hydrotreatment such as solids build up causing high pressure drop and poor mixing regimes in the reactor. Likewise, a major difficulty treating heavier feed stocks is their high metals content, circa 320 ppm. The operating parameters for the hydrotreatment of various feedstocks are

presented in Table 2-7. Operating parameters and the boiling range of the feed determine the fraction of the feed in the vapour and liquid phase. (1)

Table 2-7 Typical process conditions and hydrogen consumption for distillate hydrotreating (86)

Operating Parameter	Naphtha	Kerosene	Gas oil	Vacuum gas oil
Operating temperature (°C)	320	330	340	360
Hydrogen pressure (bar)	1-2	2-3	2.5-4	5-9
Hydrogen consumption ($\frac{Nm^3}{m^3}$)	2-10	5-15	20-40	50-80
LHSV* (h^{-1})	3-8	2-5	1.5-4	1-2

* LHSV = Liquid volumetric flow rate at 15 °C (ft^3/h)/(Volume of catalyst (ft^3)

2.2 References

1. Gray M,R. Fundamentals of oilsands upgrading. Edmonton, Alberta; 2010.

2. Hughey C, Rodgers R, Marshall A. Resolution of 11 000 compositionally distinct components in a single electrospray ionization fourier transform ion cyclotron resonance mass spectrum of crude oil. Anal Chem. 2002 15;74(16):4145-9.

3. Girdler R. Constitution of asphaltenes and related studies. Proc Assoc Asphalt Paving Technol. 1965;34:45-80.

4. Speight JG. The chemistry and technology of petroleum, fourth edition; 2007.

5. Mitchell D, Speight J. Solubility of asphaltenes in hydrocarbon solvents. Fuel. 1973;52(2):149-52.

6. Siskin M, Kelemen SR, Eppig CP, Brown LD, Afeworki M. Asphaltene molecular structure and chemical influences on the morphology of coke produced in delayed coking. Energy Fuels. 2006;20(3):1227-34.

7. Speight J. *The chemistry and technology of petroleum*. Second ed. New York, NY: Marcel Dekker, Inc.; 1991.

8. Filby R, Strong D. Nickel(ii) and vanadium(iv) complexes in alberta oil-sand bitumens. SHIH SO,MC, editor. ; 1991.

9. Qian K, Edwards KE, Siskin M, Olmstead WN, Mennito AS, Dechert GJ, et al. Desorption and ionization of heavy petroleum molecules and measurement of molecular weight distributions. Energy Fuels. 2007;21(2):1042-7.

10. Di Primio R, Horsfield B, Guzman-Vega M. Determining the temperature of petroleum formation from the kinetic properties of petroleum asphaltenes. Nature. 2000;406(6792):173-6.

11. Rubinstein I, Spyckerelle C, Strausz O. Pyrolysis of asphaltenes - source of geochemical information. Geochim Cosmochim Acta. 1979;43(1):1-6.

12. Ignasiak T, Kempjones A, Strausz O. Molecular-structure of athabasca asphaltene - cleavage of carbon-sulfur bonds by radical ion electron-transfer reactions. J Org Chem. 1977;42(2):312-20.

13. Dicke J, Yen T. Macrostructures of asphaltic fractions by various instrumental methods. Anal Chem. 1967;39(14):1847.

14. Mullins OC. The modified yen model. Energy Fuels. 2010;24:2179-207.

15. Sheremata J, Gray M, Dettman H, McCaffrey W. Quantitative molecular representation and sequential optimization of athabasca asphaltenes. Energy Fuels. 2004;18(5):1377-84.

16. Gray M. Consistency of asphaltene chemical structures with pyrolysis and coking behavior. Energy Fuels. 2003;17(6):1566-9.

17. McKenna AM, Marshall AG, Rodgers RP. Heavy petroleum composition. 4. asphaltene compositional space. Energy Fuels. 2013;27(3):1257-67.

18. Karimi A, Qian K, Olmstead WN, Freund H, Yung C, Gray MR. Quantitative evidence for bridged structures in asphaltenes by thin film pyrolysis. Energy Fuels. 2011;25(8):3581-9.

19. Rueda-Velasquez RI, Freund H, Qian K, Olmstead WN, Gray MR. Characterization of asphaltene building blocks by cracking under favorable hydrogenation conditions. Energy Fuels. 2013;27(4):1817-29.

20. Gray MR, Tykwinski RR, Stryker JM, Tan X. Supramolecular assembly model for aggregation of petroleum asphaltenes. Energy Fuels. 2011;25(7):3125-34.

21. Barre L, Simon S, Palermo T. Solution properties of asphaltenes. Langmuir. 2008;24(8):3709-17.

22. Fenistein D, Barre L, Broseta D, Espinat D, Livet A, Roux J, et al. Viscosimetric and neutron scattering study of asphaltene aggregates in mixed toluene/heptane solvents. Langmuir. 1998;14(5):1013-20.

23. Roux J, Broseta D, Deme B. SANS study of asphaltene aggregation: Concentration and solvent quality effects. Langmuir. 2001;17(16):5085-92.

24. Tanaka R, Hunt J, Winans R, Thiyagarajan P, Sato S, Takanohashi T. Aggregates structure analysis of petroleum asphaltenes with small-angle neutron scattering. Energy Fuels. 2003;17(1):127-34.

25. Moschopedis S, Parkash S, Speight J. Thermal-decomposition of asphaltenes. Fuel. 1978;57(7):431-4.

26. Rice F, Herzfeld K. The thermal decomposition of organic compounds from the standpoint of free radicals VI the mechanism of some chain reactions. J Am Chem Soc. 1934;56:284-9.

27. Kossiakoff A, Rice F. Thermal decomposition of hydrocarbons, resonance stabilization and isomerization of free radicals. J Am Chem Soc. 1943;65:590-5.

28. Gray M, McCaffrey W. Role of chain reactions and olefin formation in cracking, hydroconversion, and coking of petroleum and bitumen fractions. Energy Fuels. 2002 ;16(3):756-66.

29. Lamarca C, Libanati C, Klein M, Cronauer D. Enhancing chain transfer during coal-liquefaction - a model system-analysis. Energy Fuels. 1993;7(4):473-8.

30. Olmstead W, Freund H. Thermal conversion kinetics of petroleum residua. AIChE spring meeting; New Orleans, LA. ; 1998.

31. Wu G, Katsumura Y, Matsuura C, Ishigure K, Kubo J. Comparison of liquid-phase and gas-phase pure thermal cracking of n-hexadecane. Ind Eng Chem Res. 1996;35(12):4747-54.

32. Ford T. Liquid-phase thermal-decomposition of hexadecane - reaction-mechanisms. Industrial & Engineering Chemistry Fundamentals. 1986;25(2):240-3.

33. Fabuss B, Borsanyi A, Satterfield C, Lait R, Smith J. Rapid thermal cracking of N-hexadecane at elevated pressures. Industrial & Engineering Chemistry Process Design and Development. 1962;1(4):293.

34. Khorasheh F, Gray M. High-pressure thermal-cracking of N-hexadecane in aromatic solvents. Ind Eng Chem Res. 1993;32(9):1864-76.

35. Khorasheh F, Gray M. High-pressure thermal-cracking of N-hexadecane. Ind Eng Chem Res. 1993;32(9):1853-63.

36. Khorasheh F, Gray M. High-pressure thermal-cracking of N-hexadecane in tetralin. Energy Fuels. 1993 ;7(6):960-7.

37. Khorasheh F, Gray M. Thermal hydrocracking of N-hexadecane in benzene. Energy Fuels. 1994;8(2):507-12.

38. Zhorov Y, Volokhova G. Influence of aromatic-hydrocarbons on pyrolysis of various feedstocks. Chem Technol Fuels Oils. 1980;16(7-8):507-9.

39. Gray MR. Upgrading petroleum residues and heavy oils. 1st ed. New York, NY: Marcel Dekker INC.; 1994.

40. Savage P, Klein M. Asphaltene reaction pathways .4. pyrolysis of tridecylcyclohexane and 2-ethyltetralin. Ind Eng Chem Res. 1988;27(8):1348-56.

41. McMillen D, Golden D. Hydrocarbon bond-dissociation energies. Annu Rev Phys Chem. 1982;33:493-532.

42. Safarik I, Strausz O. The thermal decomposition of hydrocarbons .3. polycyclic n-alkylaromatic compounds. Research on Chemical Intermediates. 1997;23(2):179-95.

43. Savage P, Jacobs G, Javanmardian M. Auto-catalysis and aryl-alkyl bond-cleavage in 1-dodecylpyrene pyrolysis. Ind Eng Chem Res. 1989;28(6):645-54.

44. Savage P, Klein M. Asphaltene reaction pathways .2. pyrolysis of N-pentadecylbenzene. Ind Eng Chem Res. 1987;26(3):488-94.

45. Savage P, Klein M. Discrimination between molecular and free-radical models of 1-phenyldodecane pyrolysis. Ind Eng Chem Res. 1987;26(2):374-6.

46. Smith C, Savage P. Reactions of polycyclic alkylaromatics .1. pathways, kinetics, and mechanisms for 1-dodecylpyrene pyrolysis. Ind Eng Chem Res. 1991;30(2):331-9.

47. Smith C, Savage P. Reactions of polycyclic alkylaromatics .2. pyrolysis of 1,3-diarylpropanes. Energy Fuels. 1991;5(1):146-55.

48. Smith C, Savage P. Reactions of polycyclic alkylaromatics .4. hydrogenolysis mechanisms in 1-alkylpyrene pyrolysis. Energy Fuels. 1992;6(2):195-202.

49. Smith C, Savage P. Reactions of polycyclic alkylaromatics .7. hydrogenolysis in binary-mixtures. Energy Fuels. 1994;8(3):545-51.

50. Smith C, Savage P. Reactions of polycyclic alkylaromatics - structure and reactivity. AICHE J. 1991 ;37(11):1613-24.

51. Savage P. Hydrogen-transfer mechanisms in 1-dodecylpyrene pyrolysis. Energy Fuels. 1995 ;9(4):590-8.

52. McMillen D, Malhotra R, Chang S, Ogier W, Nigenda S, Fleming R. Mechanisms of hydrogen transfer and bond scission of strongly bonded coal structures in donor solvent systems. Fuel. 1987;66(12):1611-20.

53. Smith C, Savage P. Reactions of polycyclic alkylaromatics .6. detailed chemical kinetic modeling. Chemical Engineering Science. 1994 ;49(2):259-70.

54. Freund H, Matturro M, Olmstead W, Reynolds R, Upton T. Anomalous side-chain cleavage in alkylaromatic thermolysis. Energy Fuels. 1991;5(6):840-6.

55. Wiehe I. A solvent resid phase-diagram for tracking resid conversion. Ind Eng Chem Res. 1992;31(2):530-6.

56. Alshareef AH, Scherer A, Tan X, Azyat K, Stryker JM, Tykwinski RR, et al. Formation of archipelago structures during thermal cracking implicates a chemical mechanism for the formation of petroleum asphaltenes. Energy Fuels. 2011;25(5):2130-6.

57. Alshareef AH, Azyat K, Tykwinski RR, Gray MR. Measurement of cracking kinetics of pure model compounds by thermogravimetric analysis. Energy Fuels. 2010 ;24:3998-4004.

58. Alshareef AH, Scherer A, Tan X, Azyat K, Stryker JM, Tykwinski RR, et al. Effect of chemical structure on the cracking and coking of archipelago model compounds representative of asphaltenes. Energy Fuels. 2012;26(3):1828-43.

59. Miki Y, Yamadaya S, Oba M, Sugimoto Y. Role of catalyst in hydrocracking of heavy oil. Journal of Catalysis. 1983;83(2):371-83.

60. Prins R, Debeer V, Somorjai G. Structure and function of the catalyst and the promoter in co-mo hydrodesulfurization catalysts. Catalysis Reviews-Science and Engineering. 1989;31(1-2):1-41.

61. Weisser O, Landa S. Hydrogenation of unsaturated hydrocarbons. In: Sulphide catalysts, Their properties and applications. 1st ed. Prague: Pergamon Press; 1973. p. 118-24.

62. Kabe T, Ishihara A, Qian W. Hydrodesulfurization and hydrodenitrogenation: Chemistry and engineering. Tokyo: Kodansha; 1999.

63. Yoneyama Y, Song C. A new method for preparing highly active unsupported mo sulfide. catalytic activity for hydrogenolysis of 4-(1-naphthylmethyl)bibenzyl. Catalysis Today. 1999;50(1):19-27.

64. Bernardini F, Brill R. Uber wolframsulfid als reduktionskatalysator. Chemische Berichte-Recueil. 1963;96(9):2340.

65. Meerbott W, Hinds G. Selective hydrotreating over tungsten nickel sulfide catalyst - reaction studies with mixtures of pure compounds. Industrial and Engineering Chemistry. 1955;47(4):749-52.

66. Nikolaeva A, Puchkov P. Hydrogenation of 1-heptene and heptane under hydrogen pressure. Dokl AN SSSR. 1939;24:345.

67. Liu Z, Yang J, Zondlo J, Stiller A, Dadyburjor D. In situ impregnated iron-based catalysts for direct coal liquefaction. Fuel. 1996;75(1):51-7.

68. Hirano K, Kanda Y. Study on industrial catalyst for bituminous coal liquefaction. Fuel Process Technol. 2001;72(1):35-45.

69. Ramaswami R, Patmore DJ, Khulbe CP, Pruden BP, inventors; Catalytic hydrocracking of heavy oils. Canada patent US 4,370,221., 1983.

70. Guin J, Lee J, Fan C, Curtis C, Lloyd J, Tarrer A. Pyrite-catalyzed hydrogenolysis of benzothiophene at coal-liquefaction conditions. Industrial & Engineering Chemistry Process Design and Development. 1980;19(3):440-6.

71. Kamiya Y, Nagae S, Oikawa S. Effect of coal minerals on the thermal-treatment of aromatic ethers and carbonyl-compounds. Fuel. 1983;62(1):30-3.

72. Ogawa T, Stenberg V, Montano P. Hydrocracking of diphenylmethane roles of H2s, pyrrhotite and pyrite. Fuel. 1984;63(12):1660-3.

73. Hei R, Sweeny P, Stenberg V. Mechanism of the hydrogen-sulfide-promoted cleavage of the coal model compounds - diphenyl ether, diphenylmethane and bibenzyl. Fuel. 1986;65(4):577-85.

74. Sweeny P, Stenberg V, Hei R, Montano P. Hydrocracking of diphenyl ether and diphenylmethane in the presence of iron sulfides and hydrogen-sulfide. Fuel. 1987;66(4):532-41.

75. Montano P, Stenberg V, Sweeny P. Insitu study of the hydrogenation of diphenyl ether in the presence of pyrrhotite and H2s. J Phys Chem. 1986;90(1):156-9.

76. Chadha A, Stinespring C, Stiller A, Zondlo J, Dadyburjor D. Characterization and activity of ferric-sulfide-based catalyst in model reactions of direct coal liquefaction: Effect of preparation conditions. Ind Eng Chem Res. 1997;36(2):284-95.

77. Anderson R, Bockrath B. Effect of sulfur on coal-liquefaction in the presence of dispersed iron or molybdenum catalysts. Fuel. 1984;63(3):329-33.

78. Shyu H, Vaishnava P, Montano P. Insitu study of the decomposition of pyrite in an oxygen atmosphere. Fuel. 1981;60(11):1022-6.

79. Montano P, Vaishnava P, King J, Eisentrout E. Mossbauer study of decomposition of pyrite in hydrogen. Fuel. 1981;60(8):712-6.

80. Baldwing R, Vinciguerra S. Coal-liquefaction catalysis - iron pyrite and hydrogen-sulfide. Fuel. 1983;62(5):498-501.

81. Cook P, Cashion J. Mossbauer study of iron catalysis in victorian brown coal-liquefaction. Fuel. 1987;66(5):669-77.

82. Weng S, Wang Z, Gao J, Cheng L, Wu Z, Lin D, et al. A new activity phase in hongqi brown coal-liquefaction. Hyperfine Interactions. 1990;58(1-4):2635-9.

83. Hansen LP, Ramasse QM, Kisielowski C, Brorson M, Johnson E, Topsøe H, et al. Atomic-scale edge structures on industrial-style MoS2 nanocatalysts. Angewandte Chemie - International Edition. 2011;50(43):10153-6.

84. Kisielowski C, Ramasse QM, Hansen LP, Brorson M, Carlsson A, Molenbroek AM, et al. Imaging MoS2 nanocatalysts with single-atom sensitivity. Angewandte Chemie - International Edition. 2010;49(15):2708-10.

85. Anon. Chevron RDS process. Hydrocarbon Processing. 1998;77(11):62.

86. Topsøe H, Clausen B, Massoth F. Hydrotreating catalysis, science and technology. Berlin: Springer; 1996.

CHAPTER 3

Experimental Materials and Methods

3.1 Materials

A list of all the chemicals used in this study is presented in Table 3-1.

3.1.1 Model Compounds

Two model compounds were investigated under hydrogenation conditions, are listed in Table 3-2 with their specifications. The simpler one, n-hexadecane used for developing method and some initial tests while the main model compound was

1,3,6,8-tetrahexylpyrene consisted a pyrene group with four alkyl chains of six carbons. It is abbreviated as THP in this thesis. It was synthesized in the Department of Chemistry at the University of Alberta in Dr. Jeffrey Stryker's research group via Kumada cross coupling reaction by mixing the suspension of tetrabromopyrene, 1,2-Bis(diphenylphosphino)ethane nickel(II) chloride and dry dioxane with 1.5 M solution of n-hexylmagnesium chloride in THF similarly as described elsewhere. (1) No peaks of impurities were been detected by MALDI-MS and no traces of Ni remained after purification.

3.1.2 Catalysts
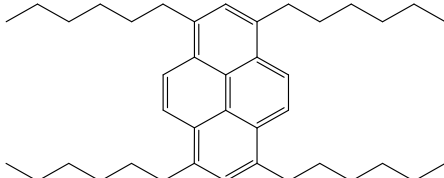
All of the iron catalysts were prepared by incipient wetness method and the detailed method is written in catalyst preparation method section. The only commercially available catalyst that used in this study was a Shell S424 Ni-Mo/γ-Al$_2$O$_3$ hydrotreating catalyst. It contained approximately 2-4 wt % Ni and 12-15 wt % Mo. The estimated pore volume for this catalyst was 0.39 mL/g. The surface area was measured as 158 m^2/g and the bulk density was 0.75 g/mL (Ying et al. (2)). The tri-lobed catalyst, approx. 3 mm in length, was ground by mortar and pestle into a powder and passed through a Fisher Scientific 150 μm sieve (No.100); the larger particles were discarded.

Table 3-1 List of the chemicals used

Chemical	Manufacturer	Purity (%) and/or Grade
1,2,3,4-tetrahydronaphthalene	Fisher Scientific	98
Pyrene	Sigma Aldrich Co.	98
n-hexadecane	Fisher Scientific	99
Carbon disulfide	Fisher Scientific	Certified Grade
Benzo[a]pyrene	Sigma Aldrich Co.	96
Iron (III) nitrate nonahydrate	Sigma Aldrich Co.	98
Magnetite (Fe_3O_4) (<5micron)	Sigma Aldrich Co.	95
α-alumina 100-325 mesh	Sigma Aldrich Co.	99
Unwashed glass beads (<106 micron)	Sigma Aldrich Co	N/A
Acid washed glass beads (<106 micron)	Sigma Aldrich Co	N/A
γ-alumina 5.8 nm pore size	Sigma Aldrich Co	N/A
Gas Cylinders		
Hydrogen	PRAXAIR Canada Inc.	Ultra High Purity, 5.0
Nitrogen	PRAXAIR Canada Inc.	Ultra High Purity, 5.0
DCTB Matrix		
T-2-(3-(4-t-Butyl-phenyl)-2-methyl-2-propenylidene) malononitrile	Santa Cruz Biotechnology	N/A
Methanol	Fisher Scientific	HPLC Grade
Methylene chloride	Fisher Scientific	HPLC Grade
Never Seez	Bostik, NSBT-8	Regular Grade
Toluene	Fisher Scientific	Certified ACS Grade

N/A=not available

Table 3-2 List of model compounds investigated

Model Compound	Molecular Structure	Molecular Weight (g/mol)
n-hexadecane		226.27
1,3,6,8-tetrahexylpyrene		538.45

3.2 Experimental Equipment

The following sections list the equipment and their specifications used in this study.

3.2.1 Batch Microreactor

The schematic of the micro batch reactor, 0.85 mL in volume, is illustrated in Figure 3-1. This batch microreactor design is a similar but smaller version of a laboratory reactor used previously in experiments studying pendant groups of asphaltene (Rueda et al. (3)). The smaller microreactor was chosen over the larger one for catalytic hydrogenation experiments because of the small quantity of feed that was available. The batch microreactor consisted of a 6.35 mm (1/4") outer-diameter (OD) stainless steel tube, 5 cm (2") in length, which was joined and capped with Swagelok fittings. The bottom of the reactor was a Swagelok stainless steel end cap which sealed the bottom of the reactor. The top of the reactor was a 1/4" x 1/16" Swagelok reducing union. The neck of the reactor protruding from the 1/4" x 1/16" reducing union at the top of the reactor was a 1.6 mm OD (1/16") stainless steel tube, 8.26 cm (3¼") in length, which was connected to a 1/8" x 1/16"

reducing union at the other end. The connection to both unions at the ends of the neck was made with ferrules fused to the 1.6 mm tube to seal the fittings.

The 1/8" x 1/16" reducing union at the top of the reactor neck was then affixed to a Swagelok Severe-Service Union-Bonnet Needle Valve. This valve allowed for operation at temperatures up to 648 °C and working pressures up to 29.4 MPa at 400 °C. The 1/8" male connector mouth of the valve was connected to a 1/8" female connector used to connect to the hydrogen gas cylinder. Not shown in Figure 3-1 is a relatively large stainless steel sleeve attached to the valve, which allowed the reactor to attach to a rod used to immerse the reactor in the sand bath. The batch microreactors were assembled by the author, whereas, the sleeve was custom built for the microreactor by University of Alberta Chemical and Materials Engineering Department Machine Shop.

A larger batch reactor, 15 mL in volume, was also constructed with Swagelok parts and was assembled by the Chemical and Materials Engineering Department Machine Shop. The same severe condition valve used in the micro batch reactor was also used for this larger reactor. The schematic and materials are the same as shown in Figure 3-1, except for larger dimensions. The reactor body was made of 3/4" stainless steel tube, 1/16" thick and 5 cm long, with a 3/4" end cap for a bottom, and a 3/4" x 1/8" reducing union for a top. The neck was constructed out of 1/8" stainless steel tube, approx. 7 cm long, with a 1/8" x 1/ 8" fitting at the end, which connected to the severe service valve. This larger batch reactor was used in the presulfidation of the catalyst, where a larger reactor volume was required.
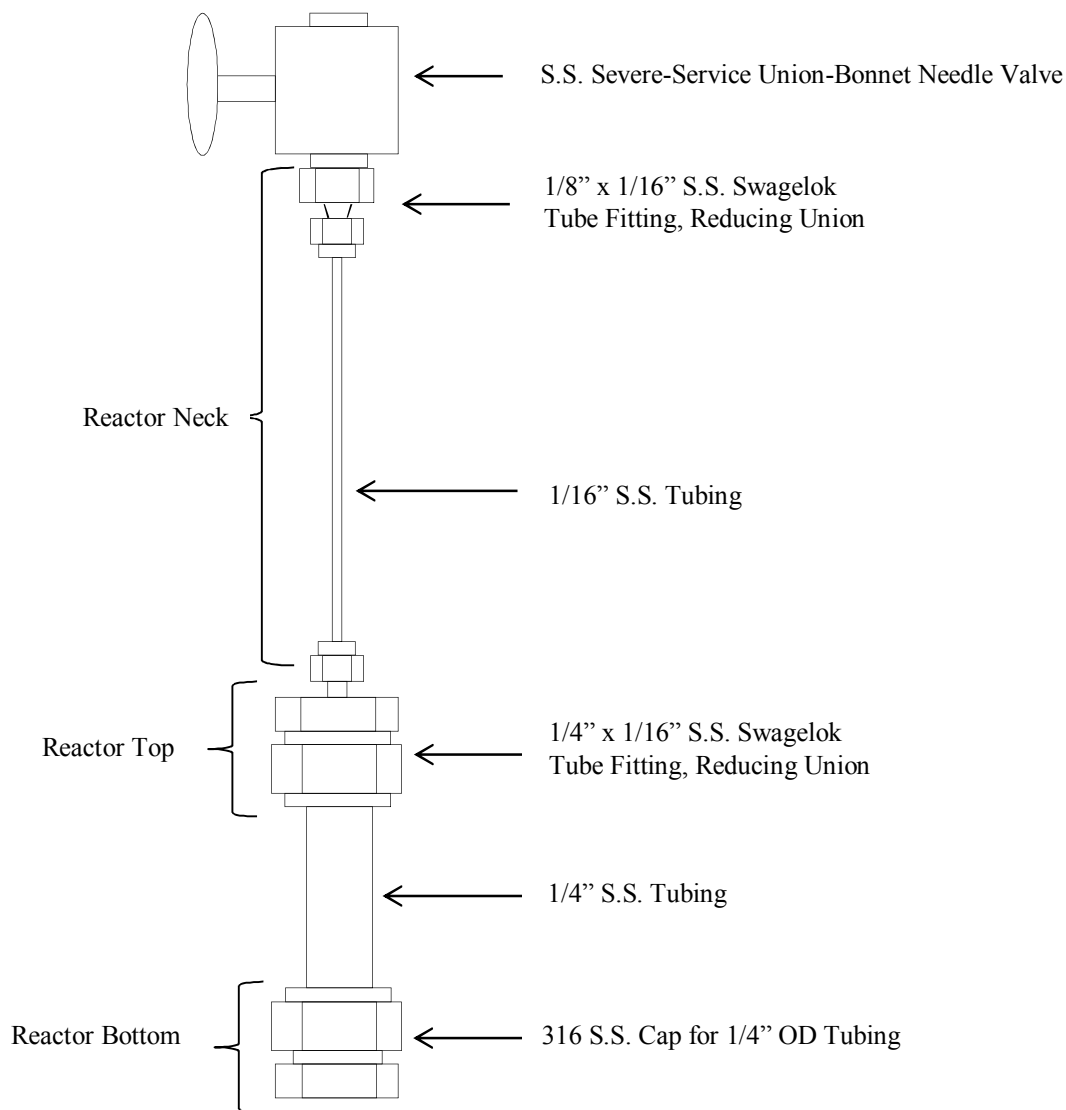
Figure 3-1 Schematic of the micro batch reactor

3.2.2 Sand Bath

The sand bath used to provide isothermal temperature for the micro reactor in the experiments for this study was a Tecam Fluidized Sand Bath Model No. SBS-4. A picture of the sand bath set-up is shown in Figure 3-2. The sand bath was filled with approximately 20 cm of silica sand. Air was sprayed through the

sand near the bottom of the sandbath by a distributor. The air flow to the sand bath was regulated by a needle valve and measured by a Gilmont D1703 rotameter. An ALL Temperature Sensors thermocouple measured the temperature of the sand bath at approximately the mid-point along the sand bath. An OMRON E5CK controller maintained the sand bath temperature at the selected set point value. A rotating cam powered by a motor was mounted above the sand bath. Reactors were attached to a rod, which could be immersed in the sand bath. To immerse the rod, the upper arm of the rod was placed onto the cam and the motor switched on, which raised and lowered the rod. The reactor was raised and lowered a total of 3 cm at a frequency of 3 Hz. This reciprocating motion provided mixing within the micro reactor. A welded guide kept the rod centred within the sand bath.
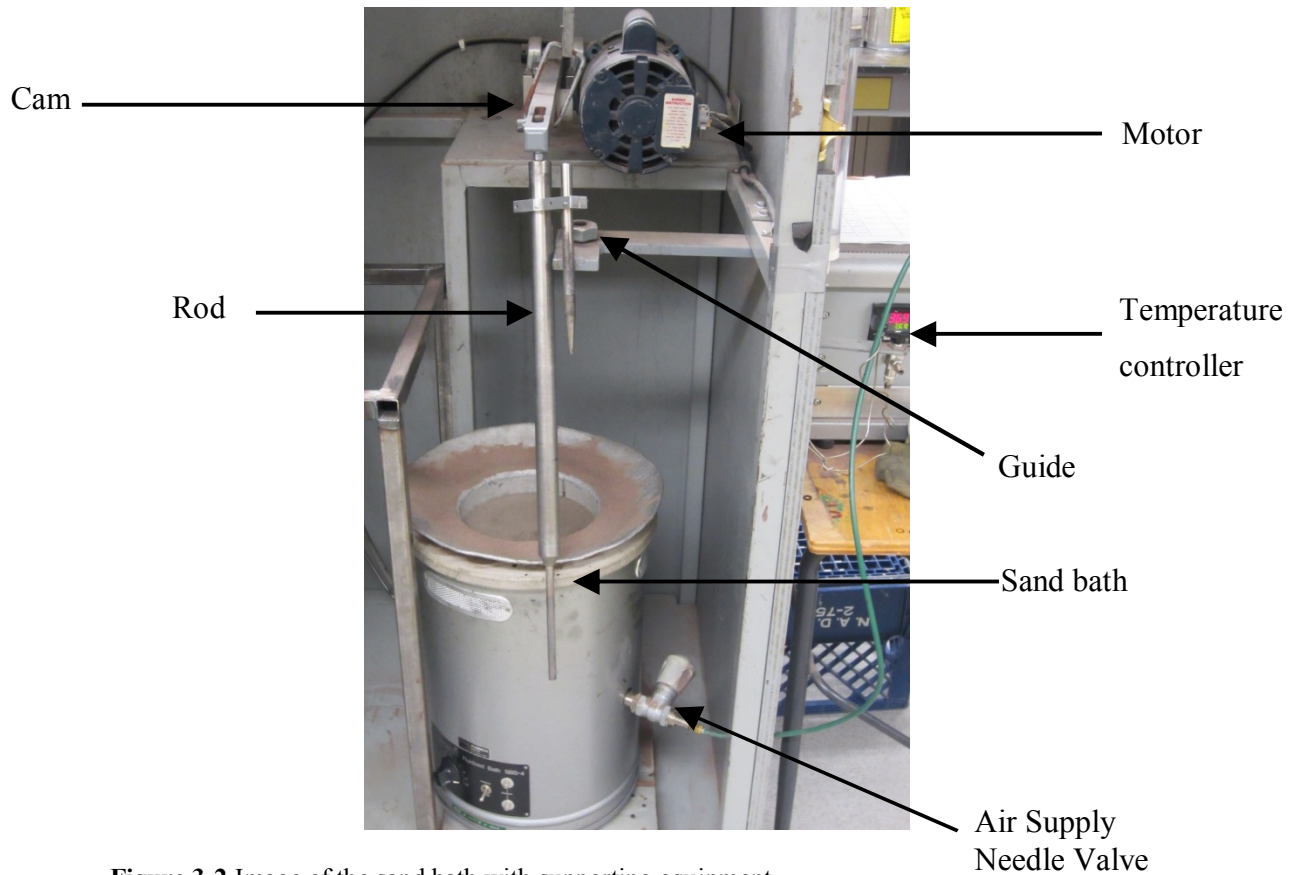
Figure 3-2 Image of the sand bath with supporting equipment

3.2.3 High Performance Liquid Chromatograph

An Agilent Technologies 1200 Series High Performance Liquid Chromatograph (HPLC) with a Zorbax Eclipse PAH column of 4.6 x 150 mm with a C18 phase of 3.5 µm particles was used to determine the concentration of unconverted THP.

The mobile phase consisted of 75-85% methanol and 15-25% methylene chloride. The temperature of the mobile phase was controlled by the instrument and was set to 23 °C. The mobile phase flow was regulated by a pump. The instrument stopped operation if a maximum pressure delivered by the pump of 400 bar was surpassed.

Table 3-3 shows the mobile phase composition and flow rate profile, for sample analyzed. This flow program and change in the composition of mobile phase allowed for good resolution during the retention times corresponding to product, parent peaks and internal standard.

The injection of samples was automated by the instrument and was set to 1 µL injection volumes, with a sample draw depth of 2.5 mm. The ultraviolet (UV) detector used to produce the chromatograms, was set record at two wavelengths, 239 nm and 270 nm, which have the maximum absorbance for THP and benzo[a]pyrene.

Table 3-3 Mobile phase composition and flow profile for THP

Time (min)	Mobile Phase Composition (Vol %)		Flow (mL/min)
	CH_3OH	CH_2Cl_2	
0-2	75	25	1
2-7	75	25	1
7-10.5	85	15	0.500
10.5-11.5	85	15	0.500
>11.5	75	25	1

3.2.4 Gas Chromatograph

Gas chromatography was used to detect and study lighter cracked products. Individual reaction products were identified by comparing their retention times with those of authentic samples and by inspection of their mass spectra. Analysis was performed by a Thermo Scientific-Trace GC Ultra (model no. K2733B0000000B0) gas chromatograph with an AI3000 Auto-injector auto sampler, and an attached Trace DSQII-Mass Spectrometer. The GC had a 30 m Thermo TR-5 GC capillary column with a 0.25 mm inner diameter and a film thickness of 0.25 μm. Three PRAXAIR cylinders of ultra-high purity: Nitrogen, hydrogen and helium were fed to the GC and were delivered at 283 kPa, 441 kPa and 441 kPa, respectively. The carrier gas was helium. Two detectors were used for analysis in this study and are shown in Table 3-4. Both instrument methods used Split flow of 25 mL/min.

The flame ionization detector (FID) was used for quantification of samples. The FID was operated at 250 °C with the following gas flows: air at 350 mL/min, hydrogen at 35 mL/min, and make-up gas at 30 mL/min. The autosampler rinsed

once with methylene chloride before injection and had a draw depth at the bottom of the sample vial.

Analysis by the mass spectrometer (MS) was performed to identify product peaks, which often was followed up by GC-FID analysis to quantify the peaks. As indicated in Table 3-4, samples were injected into the GC manually. Sample volumes were drawn with a 10 µL micro pipette, which had been rinsed three times with methylene chloride. The sample volume was then injected into the GC inlet once the software indicated to do so.

Integration of the peaks was carried out by Xcalibur 2.0.7 Thermo Fisher software which also operated the instrument. The instrument library database was a useful tool to assign structures to detected mass spectra.

The GC oven was set at 35℃ for 2 min, followed by ramping at 10℃/min to 180℃, hoding for 1 min and another ramping at 5℃/min to 300℃.

Table 3-4 Instrument method by detector used for GC operation

Parameter	Instrument Method	
	GC-FID	*GC-MS*
Sample Injection method	Autosampler	Manual injection
Sample Volume (µL)	1	1
Carrier Gas Flow (mL/min)	1.0	2
Acquisition Time (min)	44.50	44.50
Inlet Temperature (°C)	250°C	250°C
Temperature Profile		
Initial Oven Temperature	35 °C	35 °C
Hold Time	2.00 min	2.00 min
1ˢᵗ Ramp	10.0 °C/min to 180 °C	10.0 °C/min to 180 °C
Hold Time	1.00 min	1.00 min
2ⁿᵈ Ramp	5.0 °C/min to 300 °C	5 °C/min to 300 °C
Hold Time	3.00 min	3.00 min

3.2.5 Matrix-Assisted Laser Desorption Ionization-Mass Spectrometer

Matrix-assisted laser desorption ionization (MALDI) mass spectroscopy was used to detect products that are too heavy to elute in GC-MS. The instrument was an Applied Biosystems/MDS SCIEX 4800 Plus MALDI TOF/TOF Analyzer. Samples to be analyzed were prepared on a 384 Opti-TOF 123 mm x 81 mm stainless steel plate by Applied Biosystems, which was then magnetically affixed.

Laser intensity was kept constant for all analysis and the mass range of spectra was between 200-1200 Da. This particular MALDI-MS featured a tandem MS/MS mode that allowed for the fragmentation of selected precursor ions identified by normal MS operation. The settings used for MS/MS mode were the same as MALDI-MS data acquisition.

3.2.6   Proton Nuclear Magnetic Resonance Spectrometer

Nuclear magnetic resonance (NMR) spectroscopy (500MHz Varian Inova, Santa Clara, CA) was conducted in CDCl3 solution. NMR spectra were calculated using MestReNova software (Mestrelab Research, Santiago de Compostela, Spain).

3.2.7   Scanning Electron Microscopy

Scanning electron microscopy (SEM) was performed with a Hitachi S-2700 Scanning Electron Microscope equipped with a PGT (Princeton Gamma-Tech) IMIX digital imaging system and a PGT PRISM IG (Intrinsic Germanium) detector for Energy Dispersive X-Ray Analysis (EDX). A GW Electronics System 47 four quadrant solid state Backscattered Electron Detector was used for backscattered electron microscopy. A carbon evaporative coater was also housed on-site

3.2.8   Atomic Absorption Spectroscopy

The iron content of catalysts was measured by a Varian SpectrAA 220FS atomic absorption (AA) spectrometer.

3.2.9   X-Ray diffraction

X-ray diffraction (XRD) analyses were performed with a Rigaku Ultima IV diffractometer (40 kV, 44 mA) with CuKa radiation and a graphite monochromator while the Jade software was used to identify the crystalline structures.

3.2.10 X-ray photoelectron spectroscopy

X-ray photoelectron spectroscopy (XPS) analyses were carried out with an Axis 165 X-ray photoelectron spectrometer from Kratos Analytical with a Mono Al Kα source operating at 15 mA and 14 kV. Background subtraction (Shirley-type), smoothing and peak fitting were performed using the CasaXPS software package.

3.3 Experimental Procedure

3.3.1 Catalyst preparation

Iron (III) nitrate nonahydrate was used as catalyst precursor for incipient wetness treatment of α-alumina (100-325 mesh), unwashed and acid washed glass beads (<106 micron) and γ-alumina (average pore size of 5.8 nm, surface area $155\frac{m^2}{g}$). (4)

3.3.1.1 Pre-calcination of supports

All kinds of supports were calcined in a ceramic crucible inside the furnace with temperature of 500°C for 4 hours to evaporate any possible impurities. After this time, they were kept inside oven for one hour to cool down and then stored inside vial for next steps.

3.3.1.2 Pore volume measurement of supports

Knowing pore volume of support helps to calculate allowable amount of aqueous solution which can be added to support for preparation. Since glass beads and α-alumina are not porous compare to high porous γ-alumina, the pore volume here refers to void volume between support particles.

To determine the pore volume, a mass of support is weighed and water was added drop by drop to the support and mixed well. At the point that water remained on the surface and did not diffuse into the pores any more, additional mass of water was measured and mass of water per mass of support calculated, also by using density of water it reported as volume of water per mass unit of support. Table 3-5 shows pore volume values for these three supports.

Table 3-5 Pore volume of supports

Support	Mass water per mass unit of support (gr/gr)	Volume per mass unit of support (mL/gr)
α-alumina	0.5853	0.5871
acid washed glass beads	0.2517	0.273
unwashed glass beads	0.251	0.2738
γ-alumina	0.708	0.711

3.3.1.3   Incipient wetness of catalyst precursor on support

The exact mass of catalyst precursor was weighed based on required loading of iron on final catalyst and dissolved in water with the solution volume just enough to fill the pores of the support. Then these solutions were added drop by drop to support by pipette. A uniform mixture was obtained by stirring with a glass rod in order to avoid pockets of solution in particular locations.

3.3.1.4   Vacuum oven drying

Impregnated supports were dried in vacuum oven for 16 hours and at 60℃ to vaporize their water content. For some catalyst batches, it seemed that distribution of precursor is not uniform; in such cases small amount of water is added to the sample while mixing it with a stirring glass rod and then samples were kept in vacuum oven for another 16 hours.

3.3.1.5   Calcination

After drying and removing of water content, the catalysts were placed inside the oven for calcination which was at 500℃ and for 4 hours.

3.3.1.6 Presulfidation

A 15 mL stainless steel batch microreactor was used to convert iron oxide to iron sulfide. Reaction conditions were 350℃, 18.5 MPa for 2 hours. Dried and calcined iron oxide was loaded into microreactor with 10 times excess amount of CS_2 as sulfiding agent, based on stoichiometric calculation for sulfidation of elemental iron to iron sulfide. The microreactor was pressurized by hydrogen with 8.2 MPa in room temperature. After leak check, microreactor was immersed in sandbath for 2 hours. After reaction microreactor was taken out from sandbath and the sulfided catalyst product was then recovered from the reactor by rinsing with toluene solvent, following by filtration with 0.22 micron filter paper. The filtrated catalysts were dried in oven for half an hour and in 80℃. Around 5 % of catalyst weight decrease was observed after drying and it was due to loss in extraction and filtration. All of these sulfidation processes were repeated again with same conditions and sulfided iron as final product was stored for further reactions.

3.3.1.7 Unsupported iron disulfide

Unsupported iron disulfide was prepared from sulfidation of magnetite Fe_3O_4 (<5 micron, 95%) with the same procedure as the supported sulfided iron.

3.3.1.8 Ni-Mo sulfide catalyst

A commercial tri-lobed Shell S424 Ni-Mo/γ-Al_2O_3 hydrotreating catalyst (2–4 wt % Ni and 12–15 wt % Mo) was used as a positive control for catalytic hydrogenation activity. Presulfidation step with CS_2 was the same as sulfided iron catalysts with the same 10 times excess ratio for stoichiometric sulfidation of elemental Mo and Ni to their sulfide form.

3.3.2 Reactor Feed

Tetra-hexyl pyrene (THP) was found to be completely soluble in tetralin with brief shaking. Tetralin was chosen as a solvent for these experiments because

of its ability to maintain a liquid phase at experimental conditions, 430 °C and 13.9 MPa. Batches of feed solution with a concentration of 2.4 mg of THP per 1 mL of tetralin [0.0045 mol/L] were prepared by sonication for 5 minutes to give a homogeneous mixture. Reactor feed was prepared in batches of sufficient amount to perform 3-4 experiments, i.e. circa 4-5 mg of model compound in 2 mL of tetralin, and stored in a screw top vial (~4 mL) in a drawer at room temperature until the experiment was performed. No more than one batch at a time was prepared and stored in this way. Feed for aromatic hydrogenation experiments performed with pyrene for ^{1}H-NMR, was prepared in the same way and concentration of 20 mg/1 mL [0.1 mol/L]. Feeds for n-C_{16} experiments were prepared in the same fashion with the solutions of 1 wt % of compound in tetralin. The calculations to achieve the weight of compound needed to obtain 1 wt % assumed a density for tetralin of 0.970 g/mL.

The phase calculation with VMG process simulator from Virtual Material Group, Calgary, Alberta, Canada using Peng-Robinson equation of state showed that experimental pressure is 13.9 MPa and tetralin is in the liquid phase at reaction conditions.

3.3.3 Reactor Loading

First, the desired mass of catalyst according to loading of iron was weighed and added into microreactor. In order to be able to study role of catalyst and support in the reaction, the molar ratio of model compound to active metal (iron or Ni-Mo) was kept constant in all experiments (0.05 mol/mol); for example, it was 2 mg for the 2.54 wt % iron loading of sulfided Fe/α-Al$_2$O$_3$. Around 0.4 g of feed mixture was injected into the microreactor with a syringe. The syringe was rinsed at least two times with CS$_2$ before injection into the reactor. Around 0.01 g of CS$_2$ was added to the reactor as well to ensure that the catalyst remained sulfided. Finally, the top half of microreactor was tightened to the bottom half by a wrench and it connected to microreactor holder.

3.3.4 Reactor Sealing and Hydrogen Pressurization

After the reactor was successfully loaded with feed and tightened, the top of the reactor was then loosened, but not opened, and the female nut lifted up so Never Seez sealant could be applied to the threading of the reactor top. Never Seez promoted a more effective seal, helping to prevent leaks, and made the reactor easier to open after reaction. The reactor was then sealed by tightening the top of the reactor with a bench vice and wrench.

After the reactor was sealed, the reactor was connected to the H_2 cylinder with the valve apparatus shown in Figure 3-3. The reactor was pressurized by opening the H_2 cylinder valve (Valve 1), H_2 supply valve (Valve 2) and the reactor valve (Valve 4). Once pressurized, a leak detection fluid, usually water or a mixture of water and Snoop, was applied to the reactor fittings to check for leaks. If no leaks were suspected (absence of bubbles formed by the fluid), the reactor valve was closed, the cylinder valve closed, the purge valve (Valve 3) opened, and then the reactor valve opened (Valve 4). Subsequently, H_2 would vent from the reactor. The sequence was reversed to fill the reactor with H_2. Once the filling/purge sequence was started Valve 1 was left open. The reactor valve was always opened and closed first to prevent back flow of air from entering the reactor from the purge line. This filling and purge cycle was repeated three times. Then, the reactor and cylinder valves were closed and the reactor was disconnected. The reactor was then observed briefly for leaks before being immersed in the sand bath. If at any time in the above procedure a leak was detected, the reactor was disconnected from the H_2 cylinder and either the seal was tightened or loosened and Never Seez reapplied and retightened again. The H_2 pressurization procedure was then repeated to check the new seal. This procedure to address leaks rarely occurred more than twice. If a reactor was becoming problematic to seal, it was removed from service to insure that it did not fail to seal once feed and catalyst were inside.
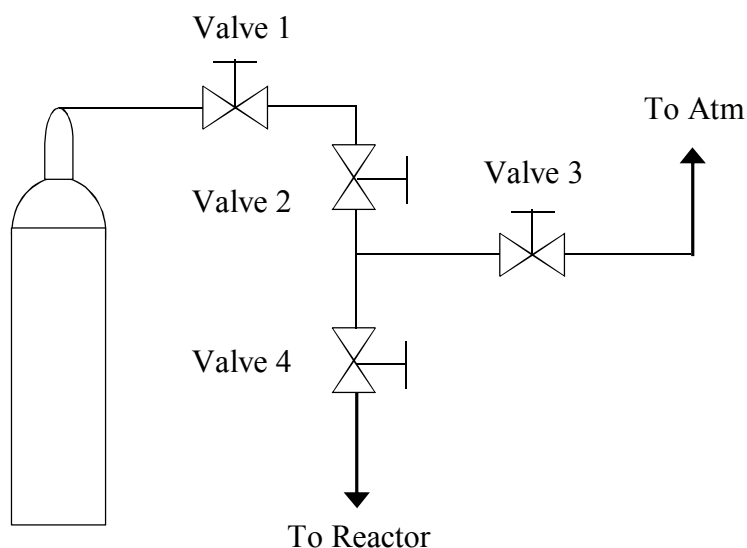
Figure 3-3 Schematic of the hydrogen cylinder valve set-up

3.3.5 Reaction

After successful sealing and pressurizing with 5 MPa pressure of hydrogen at room temperature, microreactor holder was attached to the rod of electromotor and immersed in the sand bath. The shaking provided by the electric motor promotes good agitation of reactants and catalyst. After turning on the electromotor, reaction was conducted for 30 minutes at 430℃.

After reaction the microreactor was quenched quickly with a flow of cool air to reduce the temperature and stop the reactions. Measurement of temperature profile during cooling with a thermocouple showed that it took 36 seconds to bring temperature from 430 to 300 which is a reasonable temperature to stop cracking, and about 5 minutes was needed to have the microreactor in room temperature (details about the temperature profile would be in next chapter). After cooling with air the microreactor was kept about 1 hour in the lab before opening. The reason to do this was because if there were any liquid drops inside the connecting tube between the reactor and holder valve, they can come down to the bottom of reactor and did not come out when gas purging.

3.3.6   Product Recovery

3.3.6.1   Opening of reactor

It had been observed that when the valve of microreactor was opened, some liquid drops were released with the gas because of the high pressure inside microreactor, and this could cause loss of sample and reaction products. To avoid it, a 30 cm plastic tube was connected to the valve while its other end was inside a beaker and if liquid came out, it would go inside the beaker or remain in the tube and it can be extracted easily by washing the tube with methylene chloride.

3.3.6.2   Product recovery

In next step, the top half of reactor was loosened with a wrench and products and other contents of microreactor drained into a beaker, and microreactor was being rinsed with solvent until it was thought that all the contents of reactor have been recovered.

Also to make sure that there was not any sample inside the connecting tube of microreactor and its holder, this tube was being rinsed with solvent for 5 times.

3.3.6.3   Separation of Catalyst from liquid sample

Catalysts were separated from liquids by filtration using a 0.22 μm filter paper.

3.3.6.4   Evaporation of methylene chloride

A rotary evaporator apparatus was used for solvent separation. Heat was provided by water at temperature of 55℃, while condenser temperature was 9.5℃. Also a bump trap was utilized to make evaporation more efficient. Evaporation was stopped when it was observed that all of solvent was separated from tetralin and model compound mixture. Approximately 1-2 mg of benzo(a)pyrene was added to the recovered reaction products after evaporation of solvent as an internal standard

for GC-MS and HPLC analysis. Final product was pipetted into a vial and stored in the freezer for further analysis.

3.3.6.5   Evaporation of Tetralin

The evaporation of Tetralin was performed only for ^{1}H-NMR spectroscopy samples which needed to be tetralin free because of overlapping of peaks. For evaporation, a rotary vacuum evaporator was used while the temperature of water for evaporation was 90℃, condenser temperature was 4℃ , pressure was around 0-1 mbar and time of evaporation was around 4 hours.

3.3.7   Sample Analysis

Once the reactions had been completed and the product liquid recovered, analysis by HPLC, MALDI-MS or GC was carried out depending on the experiment performed. The reaction product samples were analyzed by HPLC to determine the conversion, while MALDI-MS was used to identify product species, and determine a selectivity ratio for product compounds, and GC to detect and quantify cracked products. The schematic of different classes of reaction products and the corresponding analysis technique is shown in Figure 3-4.
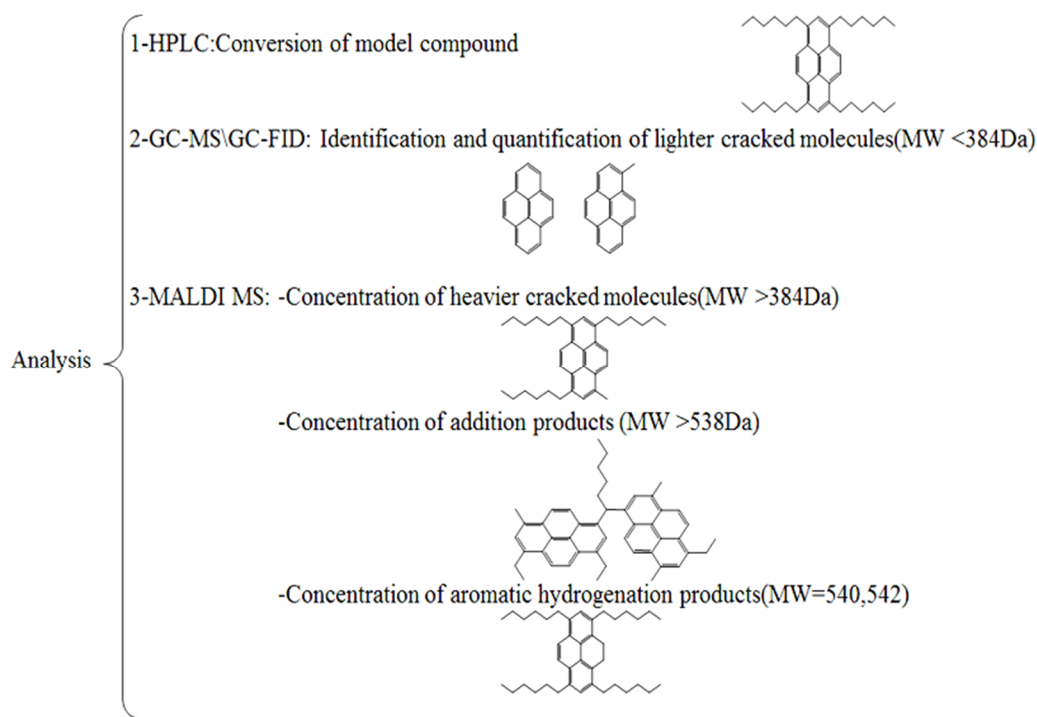
Figure 3-4: Different classes of reaction products and the corresponding analysis technique

3.3.7.1 HPLC Analysis

Product samples were analyzed by HPLC to evaluate the remaining model compound concentration and therefore measure the conversion of the model compound after a reaction was performed. HPLC analysis was selected for conversion evaluation because the model compound was known not to elute in GC instruments due to its relatively large size (>500 Da).

Undiluted samples were pipetted into a 2 mL vial and placed into the auto sampler of the HPLC.

Integration of the resulting chromatograms was performed by the Agilent software operating the HPLC. Generally, peak resolution was good and retention times were consistent. Calibration curves were constructed for the calculation of the measured concentration of the model compound. Detailed information on how the calibration curves and the chromatograms were obtained can be found in Appendix A.

3.3.7.2 GC Analysis

GC analysis was used to detect and quantify lighter cracked products formed in the reaction.

About 0.1-0.2 mL of sample was diluted with methylene chloride in a vial for analysis. The vial was then placed in the autosampler to be injected and analyzed by the GC.

Integration of the peaks was carried out by Xcalibur software which also operated the instrument. The instrument library database was a useful tool to assign structures to detected mass peaks. Detailed information on how the calibration curves and the chromatograms were obtained can be found in Appendix B.

3.3.7.3 MALDI-MS Analysis

Analysis by MALDI-MS allowed for the identification of heavier product compounds, and determination of their yields for the reaction products.

MALDI-MS/MS is a powerful mass spectrometer technique that allows for the verification of plausible product peaks in a reaction product MALDI-MS spectrum. This technique isolates ions of a single precursor (selected m/z ratio) by two polarized plates, and irradiates them with a high intensity laser, and then detects the resulting ionized fragments. Unfragmented parent ions also are detected at the appropriate mass to charge ratio.

Producing the DCTB matrix, which is used to ionize the large molecules to be analyzed, was the first step in preparation of the MALDI plate to be analyzed by the MALDI-MS instrument. For matrix preparation, solution of DCTB in methylene chloride with concentration of 10 mg/mL was prepared and with sonication for around 1 minute it assured that matrix was fully soluble in methylene chloride. Then 15 μL of sample was mixed with matrix into small containers in 3 ratios 1:1, 1:2 and 1:4 by a vortex device and centrifuge. They were injected on MALDI plate wells with a micro-pipette. The plate with the samples to be analyzed, once dry, was blown mildly across the surface with air to remove dust. Dust was

also removed in this way from the metal plate holder and the loading chamber to the MALDI-MS instrument. The plate was then affixed to the plate holder and placed into the loading chamber.

The generation of MALDI-MS spectra was performed manually by directing the laser to irradiate sections of the plate with sample. The results obtained in this study are representative of the typical spectrum produced from the observance of multiple spectra from various wells of the same sample. Poor MALDI-MS spectra, i.e. lots of noise, no model compound or products detected, too little ionization, or excessive detection of matrix adducts and contaminates, were summarily discarded. MALDI-MS/MS spectra were obtained in the same fashion using the same sample plate. Further detail of MALDI-MS analysis method can be found in Appendix C.

3.3.7.4 ^{1}H-NMR analysis

MestReNova software (Mestrelab Research, Santiago de Compostela, Spain) was used for generation of NMR spectra, integration and interpretation of results for this set of experiments, also software database helped for identification of unknown peaks.

3.3.8 Catalyst characterization

To have better understanding of the prepared iron sulfide catalyst several characterization experiments were performed on sulfided Fe/α-Al$_2$O$_3$: scanning electron microscopy (SEM/EDX) for imaging from catalyst and using mapping mode imaging for finding the location of elements in the depth correspond to diffusion of equipment signal, X-Ray diffraction (XRD) to specify the crystalline phase of iron sulfide in the bulk of catalyst before and after reaction and X-ray photoelectron spectroscopy (XPS) to specify chemical and electronic state of iron and sulfur elements on the surface. AAS and SEM test were performed on the catalyst before reaction, while the XRD and XPS applied to the catalyst both before

and after reaction. For AAS, a known mass of sulfided iron was dissolved in 100 mL of 1 molar nitric acid and was submitted for analysis.

3.4   References

1. Liu N, Wang Z-. Kumada coupling of aryl, heteroaryl, and vinyl chlorides catalyzed by amido pincer nickel complexes. J Org Chem. 2011;76(24):10031-8.

2. Ying Z, Gevert B, Otterstedt J, Sterte J. Large-pore catalysts for hydroprocessing of residual oils. Ind Eng Chem Res. 1995;34(5):1566-71.

3. Rueda-Velasquez RI, Freund H, Qian K, Olmstead WN, Gray MR. Characterization of asphaltene building blocks by cracking under favorable hydrogenation conditions. Energy Fuels. 2013;27(4):1817-29.

4. Groot CK, de Beer VHJ, Prins R, Stolarski M, Niedzwiedz WS. Comparative study of alumina- and carbon-supported catalysts for hydrogenolysis and hydrogenation of model compounds and coal-derived liquids. Ind Eng Chem. 1986;25(4):522-30.

CHAPTER 4

Results and discussion

4.1 Validation of experiments

4.1.1 Temperature profile of microreactor in the sandbath

To measure the actual temperature profile inside the microreactor during the reaction and in the quenching period, a modification was made to the microreactor. The end cap of microreactor was replaced with a 1/4 in.×1/16 in. union and the thermocouple was inserted all the way to the center of microreactor. The reactor was loaded with the hydrogen gas at the same pressure as in the usual

experiments (5 MPa) but without feed. After successful leak check, the thermocouple was connected by wire to the recorder device. The temperature of sandbath was set to 430°C, and the modified microreactor was immersed into the sandbath and recording began. Another thermocouple was inserted inside the sandbath to check if the actual temperature has any deviation from controller temperature. After spending enough time, the reactor is pulled out from sandbath and quenching started immediately while the thermocouple was still inside the microreactor. Figure 4-1 shows the temperature profile for the microreactor and sandbath.
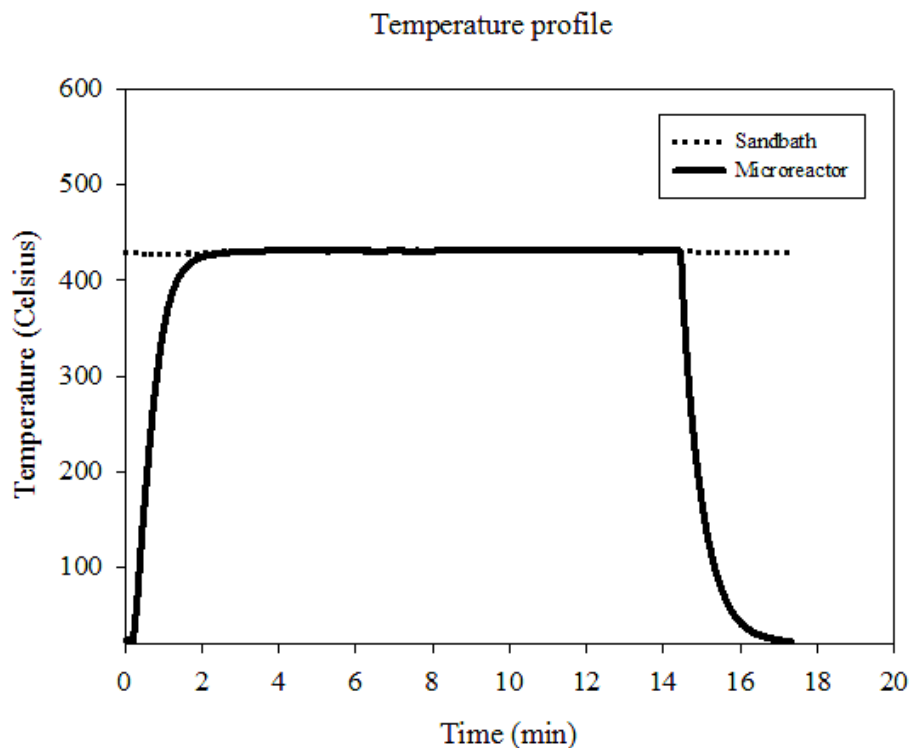

Figure 4-1: Temperature profile of microreactor and sandbath, measured by thermocouples

The steady state temperature for reaction time is determined by average of temperature in the plateau section and it was 430.18°C. The heating time is defined as the time microreactor needs to get to the 95 % of steady state temperature (410°C) and it was 1 minute and 29 seconds, which is only 4 % of total reaction time. The cool down time is defined as the amount of time required to decrease microreactor

temperature to 300℃ , after which we expected to see no further cracking activity. The Figure 4-2 shows the comparison between cool down time with water and air.
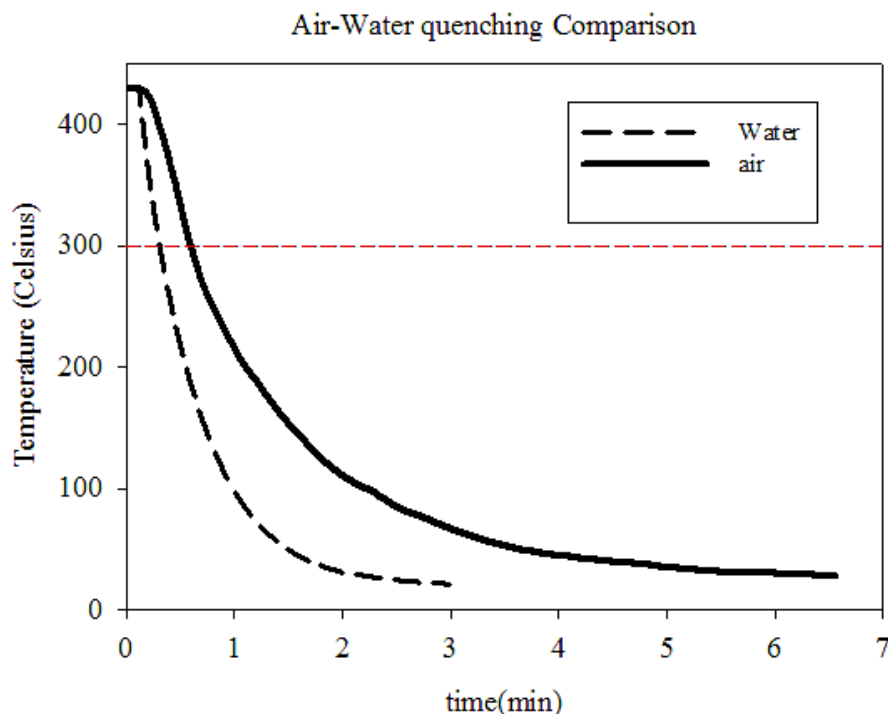
Figure 4-2: Comparison of cool down time between quenching with water and air

The cool down time was measured as 17 and 36 seconds for water and air quenching respectively. Although this time for water is almost half of the time for air, the sudden temperature decrease made problems for the microreactor and it couldn't be used for more than 2 reactions because of leaking. Therefore; the microreactor was quenched with flow of air for the model compound experiments.

The temperature controller of the sandbath with the set point value of 430℃, would turn off the heating if the temperature overshoots the set point, allowing the temperature to drop down until it fell below the set point and at this time the heater starts again. In this temperature measurement, the sandbath temperature varied between 426.1 and 431.6℃ so total deviation from set point was only 1.1 %. Because the setting of the temperature controller was the same for all of the experiments, this variation should not have considerable effects on the results. In

this experiment the effect of heat required for heating the feed and reaction heat has not been considered because both of them should have negligible effect on the temperature profile compare to the mass of microreactor, 37.7 g while the feed, catalyst and CS_2 mass was not more than 0.5 g.

4.1.2 Repeatability of results

Analysis of the repeatability of results was performed to make sure that the HPLC, GC and the MALDI-MS data were repeatable, and also to find the error estimates involved with these instrument measurements.

4.1.2.1 Repeatability of HPLC Analysis

The analysis were performed at two wavelengths (239 and 279 nm) in which the model compound and the internal standard had the maximum absorbance respectively. The calibration curves are illustrated in Figure 4-3 and Figure 4-4. The detailed method for finding these figures is available in Appendix A. After obtaining these calibration curves, some known concentration samples were tested at two wavelengths to compare the values found by calibration curve with the actual concentrations. This comparison is presented in Figure 4-5. The average uncertainty of values was 5 % with a maximum of 7%. Therefore; the reliability of calibration curve was confirmed with this experiment. Moreover, for each reaction sample, the HPLC analysis was repeated 3 times at each wavelength and the average values were used for calculation.
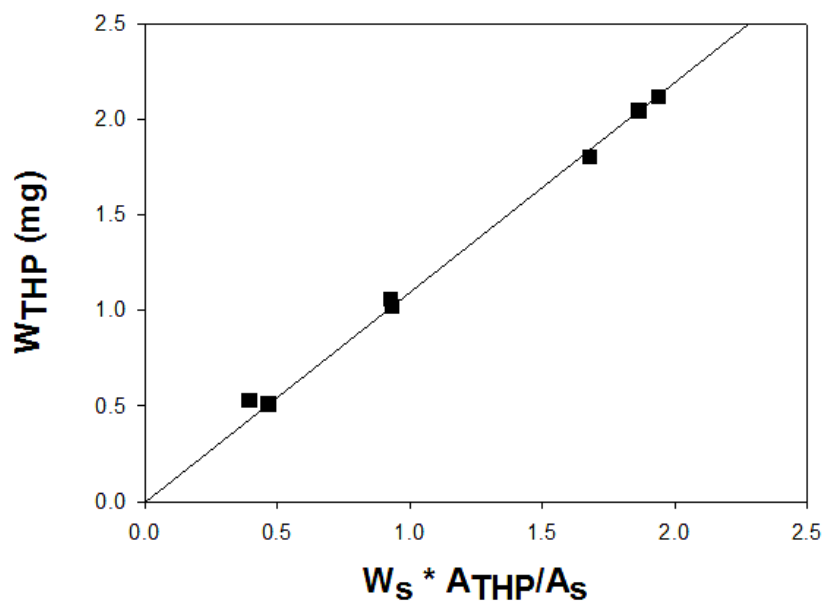
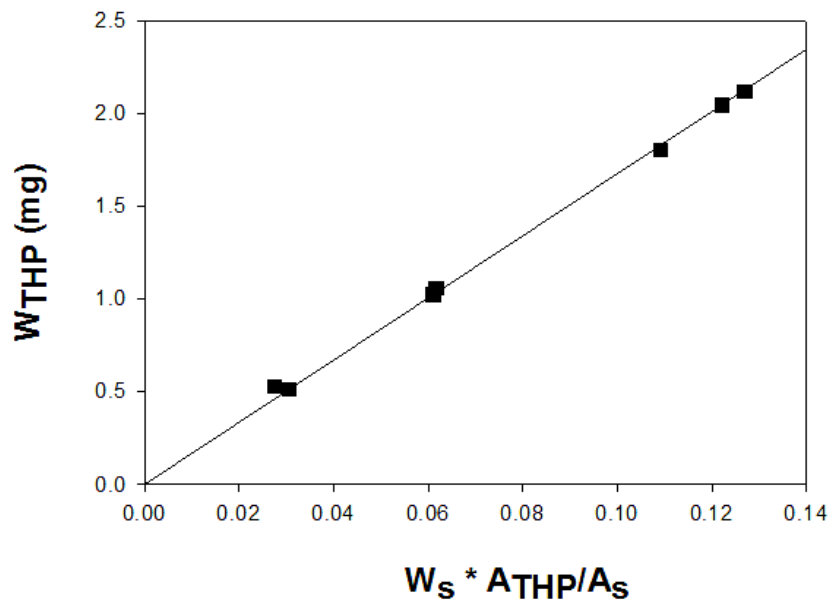**Figure 4-3:** HPLC calibration curve of for 1,3,6,8-tetrahexylpyrene at 239 nm

Figure 4-4: HPLC calibration curve of for 1,3,6,8-tetrahexylpyrene at 270 nm
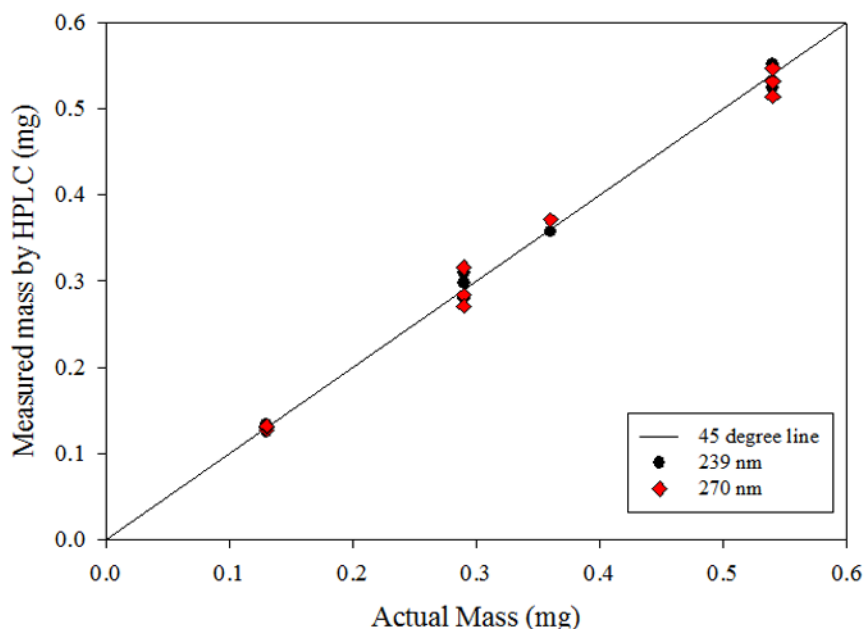
Figure 4-5: Verification of HPLC analysis by measuring known samples

4.1.2.2 Repeatability of GC Analysis

The GC-FID was used to determine the concentration of pyrene and other short alkylpyrenes in the cracking products. The internal standard calibration curve for GC-FID is presented in Figure 4-6 assuming that the response factor for short alkylpyrenes is the same as pyrene. Due to insignificant concentration of these compounds compared to longer alkyl chain pyrenes from MALDI-MS no attempts were made for a special verification experiment and the reliability of concentrations from GC-FID was checked only by duplicating each sample. In addition from the Figure 4-6, it is obvious that uncertainty of the calibration curve is much less at the lower concentrations which is relevant to the range of concentrations for pyrene and alkylpyrenes.

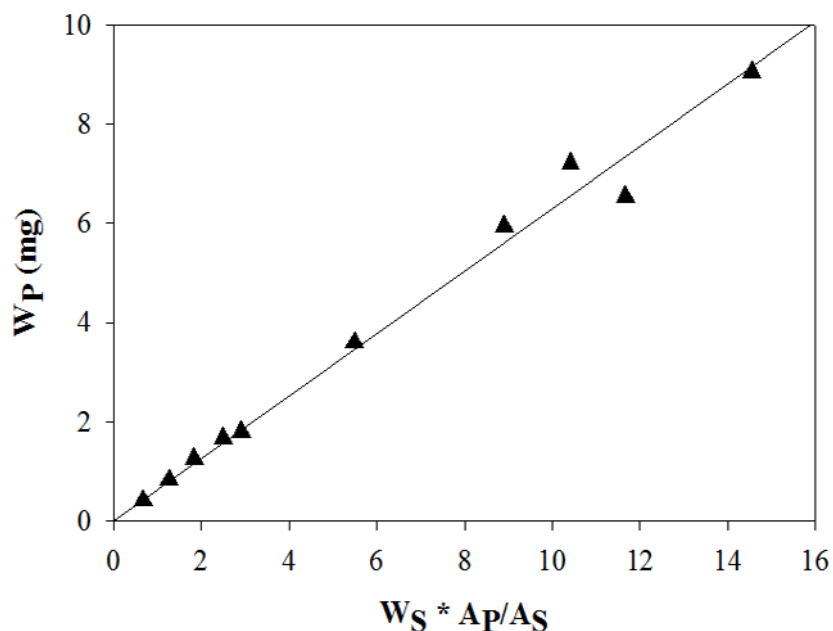**Figure 4-6:** GC-FID calibration curve of for pyrene

4.1.2.3 Repeatability of MALDI-MS Analysis

MALDI-MS spectra can be different even for the same well on the plate, due to nature of the instrument. Therefore it is very important to have error estimate about the reliability of measurements. The average percent error for MALDI-MS experiments from previous work in our research group (1) was from 5% to 17%. The average percent error for all repeatability data obtained was 12%. In this work, samples to be analyzed with MALDI-MS, prepared in 3 different ratios to the matrix (1:1, 1:2 and 1:4) and each sample was injected on the two plate wells. The change in the concentration of matrix in the sample solutions would change the absolute intensity of peaks but the ratio should be constant. If the ratios of the intensity of the product peak with highest intensity to parent compound remained in the error bounds mentioned above, the value was accepted; If not, the analysis was repeated for that sample.

4.1.3 Validation of catalyst activity

Reactions with n-hexadecane were conducted to develop the experimental method and also check the activity of sulfided iron catalyst for addition reaction suppression. This long chain alkane was a proper choice for the validation experiments due to its high molecular weight which ensures cracking in the liquid phase and also it was observed before that it would produce addition products and olefins.(2, 3) For this set of experiments only GC-FID and GC-MS were used for finding conversion and yield of addition product by using biphenyl as internal standard. The major products were: alkanes and alkenes with 7 to 14 carbon numbers, branched and linear alkanes with carbon number greater than 16 and alkyl-tetralins with different size of alkyl chains as the addition product. Naphthalene, 1-methyl indane and n-butyl benzene were the products of tetralin dehydrogenation, ring contraction and ring opening reactions respectively. They are illustrated in Figure 4-7.

Naphthalene   1-methyl Indane   n-butyl Benzene
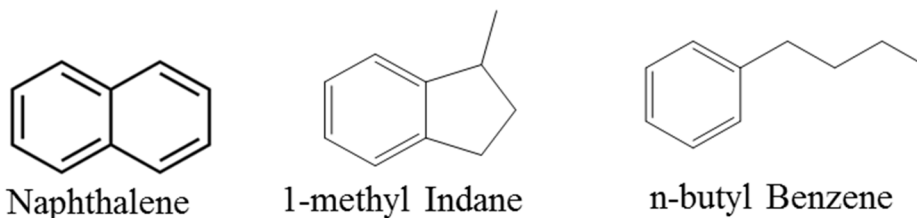
Figure 4-7: Products of tetralin reaction in n-hexadecane hydrogenation.

The GC-FID results showed that yield of addition products was reduced by using sulfided Fe/α-Al$_2$O$_3$ catalyst around 47 %, and its activity was confirmed to proceed to the next set of experiments. Figure 4-8 is the GC-MS spectrum of the reaction products for cracking of n-hexadecane in tetralin with sulfided Fe/α-Al$_2$O$_3$ catalyst at 430℃, 13.9 MPa, 30min.
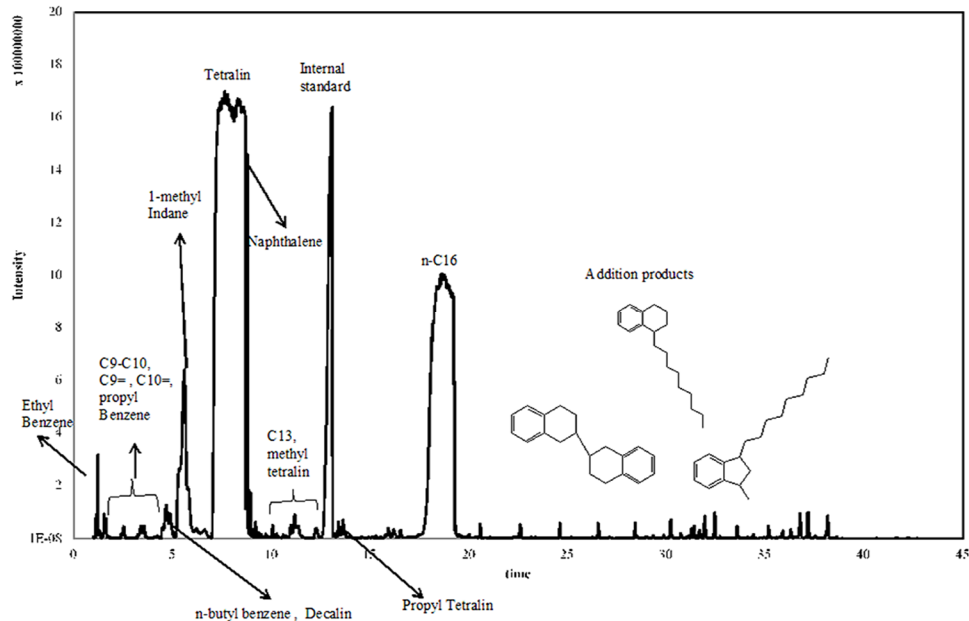
Figure 4-8: GC-MS spectrum of n-hexadecane hydrogenation with sulfided Fe/α-Al$_2$O$_3$ catalyst at 430℃, 13.9 MPa, 30 min and the major products of reaction

4.2 Reactions of 1,3,6,8-tetrahexylpyrene

4.2.1 The phases present in the reactor and effect of reaction parameters

It is necessary to remind which phases are present in the multiphase microreactor. The phase calculation showed that the materials are in the liquid phase, therefore both cracking and addition reactions are occurring in liquid phase, whereas the hydrogenation reaction of olefins is on the surface of catalysts with dissociatively adsorbed hydrogen atoms. It has to be mentioned that the role of catalyst is in suppression of the side reactions, while the main mechanism is happening in the liquid phase and olefins need to migrate to the active sites of catalyst; therefore the catalytic reaction is different from general catalytic mechanism which requires diffusion of main reactant to active sites of catalyst for reaction to occur.

The dilution ratio of model compound in tetralin is selected based on the fact that diluted systems are more suitable for catalytic studies by reducing the rate

of reaction which helps to study precisely what is happening in reaction mixture for such a complex system. Increase in the concentration of model compound, will result in an increase in concentration of formed radicals, and possibly the rate of addition reactions would rise and higher yield of addition products is expected to be observed.

The hydrogen gas pressure was selected to meet two criteria: first, it should not exceed the safety limit of pressure for microreactor and second, the data obtained from simulation of phase calculation to keep the reactor feed in the liquid phase. Increase in pressure of the reactor is expected to increase rate of hydrogenation by facilitating saturation of liquid phase from hydrogen and its adsorption on the surface.

4.2.2 Reaction pathways

The reaction products, as detected by GC-MS and MALDI-MS, can be ascribed to the addition reactions, cracking and aromatic hydrogenation. The balance to 100% was considered as losses during extraction, handling and evaporation of solvent. Addition products are defined as compounds with higher molecular weight than model compound and they were identified and quantified by MALDI-MS. The most abundant compounds are molecules with masses of 612 and 788 Da. These two peaks were studied with MS/MS technique to find their structure. The peak at 612 is ascribed to a molecule consisting of two alkyl pyrenes connected together with an alkyl bridge; for the 788 Da peak, an alkyl tetralin is substituted to one of pyrenes. The other peaks are compounds with the same structures with different size alkyl chains up to 1040 Da. The region of the MALDI-MS spectrum that corresponds to the addition products and the suggested structures for the two products with highest intensities is presented in Figure 4-9.
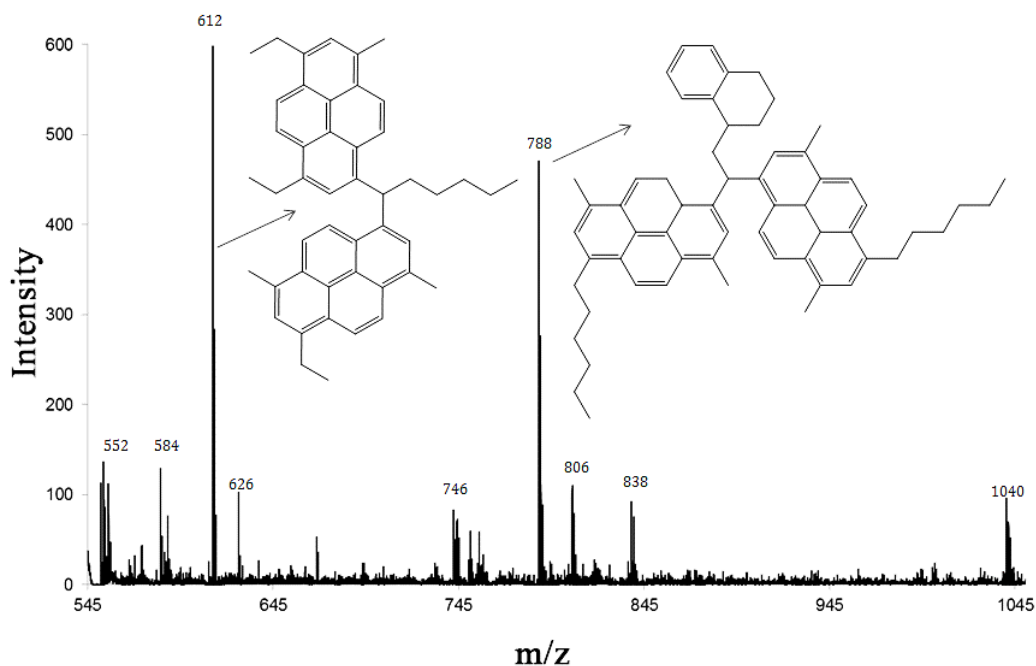
Figure 4-9: Addition products region of MALDI-MS spectrum and suggested structures for the peaks with the highest intensity

Cracking products are defined as compounds with lower molecular weight than THP, resulting from β-scission of alkyl chains. The compound 1-methyl 3,6,8-trihexylpyrene, with mass of 468 Da, was the most abundant product. The concentration of smaller molecules such as pyrene and short-alkylpyrenes was measured by GC-MS, while MALDI-MS was utilized for heavier compounds. The concentration of pyrene and short-alkyl pyrene compounds was insignificant compared to longer alkyl chain pyrenes from MALDI-MS. The region in the MALDI-MS spectrum corresponding to the cracking products and the suggested structure for the product with highest intensity is presented in Figure 4-10.
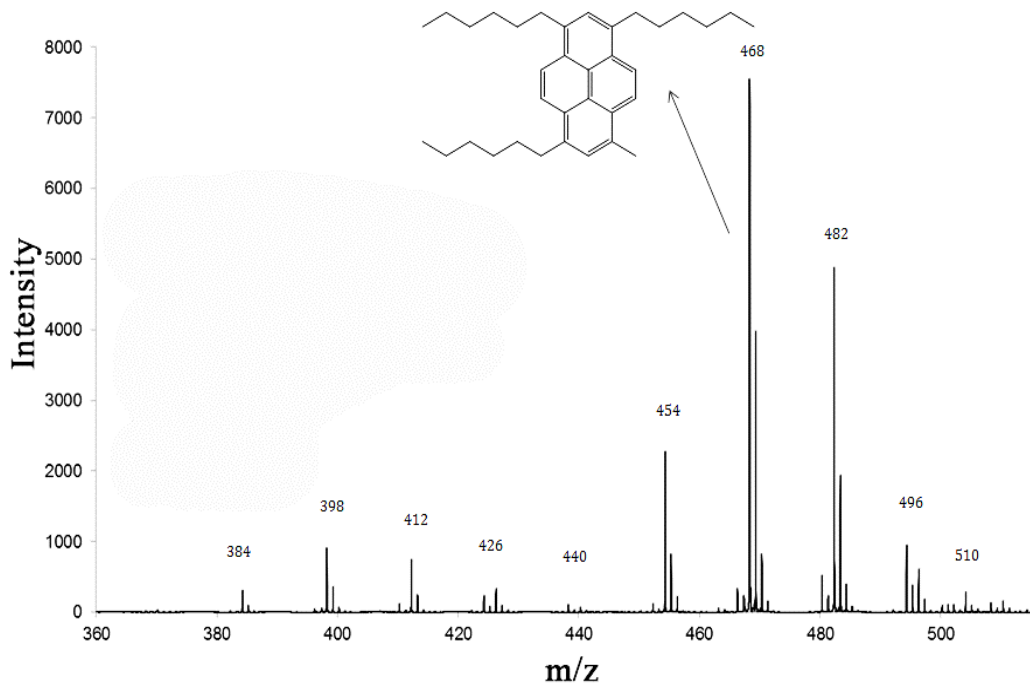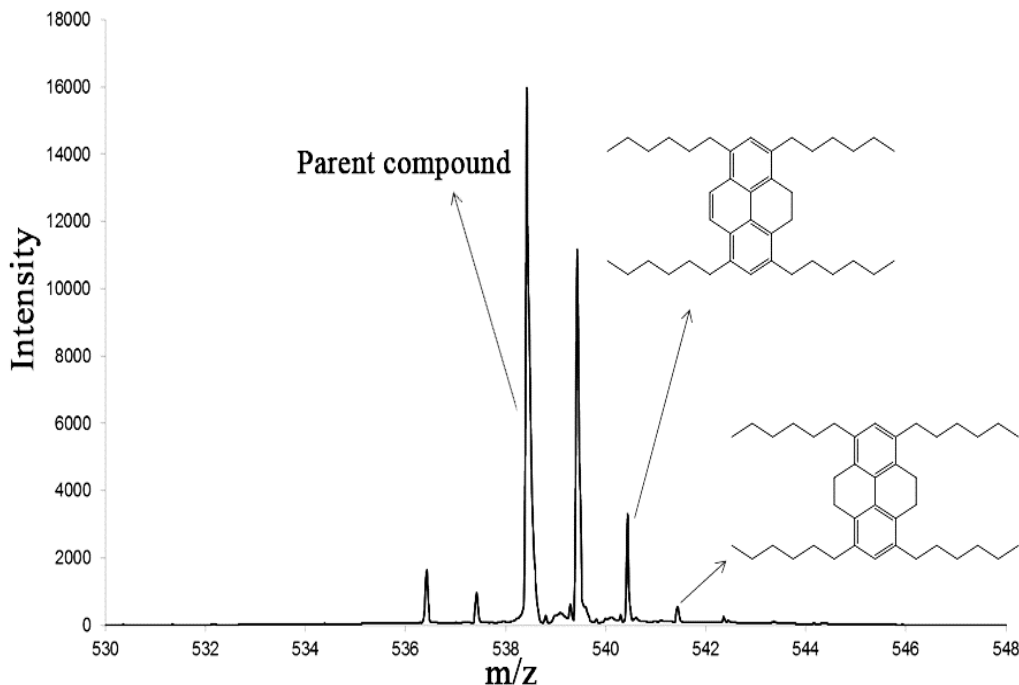
Figure 4-10: Cracking products region of MALDI-MS spectrum and suggested structure for the peak with the highest intensity

The concentration of pyrene and short alkyl pyrenes from GC-MS were less than 4 % of total cracking product. For the calculations it is assumed that response factor of the alkylpyrenes is equal to pyrene.

Finally, the peaks in MALDI-MS spectrum with +2 and +4 difference with THP were assigned to the aromatic hydrogenation products that are hydrogenated THP molecules that did not participate in further cracking or addition reactions. Figure 4-11 shows the region of MALDI-MS spectrum for aromatic hydrogenation products and the expected structures of di- and tetrahydro alkylpyrenes.

Figure 4-11: Aromatic hydrogenation products region of MALDI-MS spectrum and structures of di- and tetrahydroalkyl pyrenes

The peaks intensity in the last three figures needs to be processed by considering the effect of isotopes. Isotopes were identified using the Scientific Instrument Service Isotope Distribution Calculator at http://www. sisweb.com/mstools/isotope.htm. For example, the isotope distribution for the m/z = 468.13 cracking product peak gives an isotope distribution of 38.6%, 7.3%, 0.9% and 0.1% for each isotopes at m/z = 469, 470, 471 and 472, respectively. These ratios were used to find the actual intensity of the signal associated with each compound. In the edited MALD-MS spectra, the entire signal for each compound is assigned to the m/z corresponding to the highest abundance isotopes. These effects would become critical for parent compound when it had isotope with m/z equal to aromatic hydrogenation products.

4.2.3 Mole balance calculation

After identification and assigning each peak to its proper class of product, yield of each class should be calculated and be used to confirm the mole balance of

reaction. Using simple mass balance for yield calculation was not possible due to the loss of side chains as vapor products and during evaporation of solvent. Therefore mole balance based on the moles of pyrene rings used in this study with the assumption that no formation, neither destruction of pyrene ring happens in the reaction condition. The term "destruction" here refers to ring opening reaction resulting in aromatic cores with three or less number of rings. In our batch reactor we have:

$$\frac{dmol_{Pyrene\ ring}}{dt} = 0 \qquad \rightarrow \quad mol_{Pyrene\ ring}^{in} = mol_{Pyrene\ ring}^{out} \qquad (4-1)$$

The known initial pyrene ring moles in the feed, can participate in any of the reaction pathways mentioned above or can be remained unreacted:

$$mol_{Pyrene\ ring}^{in} = mol_{Pyrene\ ring}^{Reacted} + mol_{Pyrene\ ring}^{Unreacted} \qquad (4-2)$$

Reacted pyrene rings moles, can be determined by HPLC value for conversion of model compound:

$$mol_{Pyrene\ ring}^{in} - mol_{Pyrene\ ring}^{Unreacted} = mol_{Pyrene\ ring}^{Reacted} \qquad (4-3)$$

The reacted pyrene rings moles would be summation of three reaction pathways:

$$mol_{Pyrene\ ring}^{Reacted} = mol_{Pyrene\ ring}^{Addi.} + mol_{Pyrene\ ring}^{Crac.} + mol_{Pyrene\ ring}^{Aroma.\ Hydr.} \qquad (4-4)$$

Addition products in Figure 4-9 shows that there are two pyrene ring moles in per mole of addition reactions, while for cracking and aromatic hydrogenation this ratio is one. (Figure 4-10 and Figure **4-11**)

$$mol^{Reacted}_{Pyrene\,ring} = 2\left(\frac{mol_{Pyrene\,ring}}{mol_{add.}}\right) + 1\left(\frac{mol_{Pyrene\,ring}}{mol_{Crac.}}\right) + 1\left(\frac{mol_{Pyrene\,ring}}{mol_{Arom.Hydr.}}\right) \quad (4-5)$$

The simplified MALDI-MS spectra were plotted to allow yield calculations in which the peak intensity is plotted against the corresponding m/z. In Figure 4-12, one example of the simplified MALDI-MS spectrum is illustrated. Product yield is defined as a number of moles of each reaction product per 100 moles of reacted model compound. Calculations were made based on the fact the ratio of intensity is equal to molar ratio of peaks.
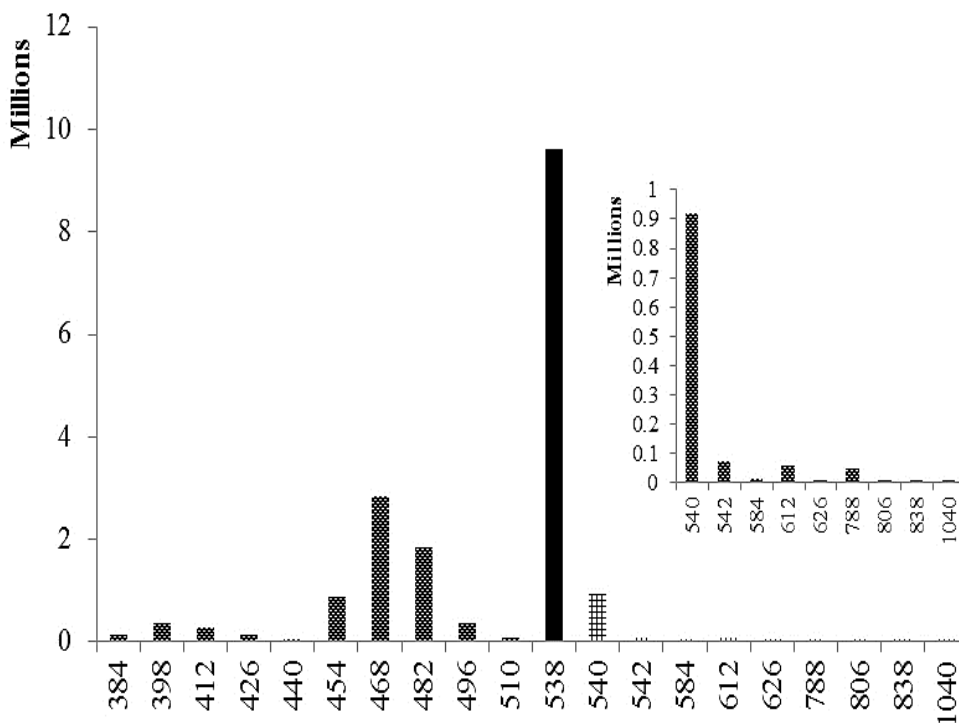

Figure 4-12: simplified MALDI-MS peaks for calculation of yields of each pathway, Ni-Mo sulfide/ γ-Al$_2$O$_3$, 430℃, 13.9 MPa, and 30 min

The parent compound was selected as a reference. The ratio of intensity of any peak to parent compound peak is equal to the moles of that product to moles of unreacted model compound and unreacted moles can be found using the conversion value that is reported by HPLC. The material balance was closed with losses that were below 4%. For example, for a 2.54 wt % loading of iron on sulfided iron/α-Al_2O_3, the product distribution was: 13.6 mol % of addition products, 84 mol % of cracked products, no aromatic hydrogenation and losses was 2.4 mol % by difference.

4.2.4 Comparison of catalyst activity

The specifications of different catalysts, THP conversion and products yields for catalytic and non-catalytic reactions are shown in Table 4-2.The blank control experiments were performed without any catalyst and with γ-alumina. Due to the large size of model compound, in order to overcome internal mass transfer limitations, non-porous glass beads, low porous α-alumina were selected for the catalyst preparation and compared with porous γ-alumina. The size of model compound is estimated using Materials Studio software at 430 °C and vacuum, for 1 ns with sampling for 1 ps. Three distances are defined and shown in Figure 4-13. Table 4-1 shows the average distances and standard deviations for these three distances. Based on these results, γ-alumina with pore sizes of 5.8 nm is a suitable support to study effect of mass transfer limitations.
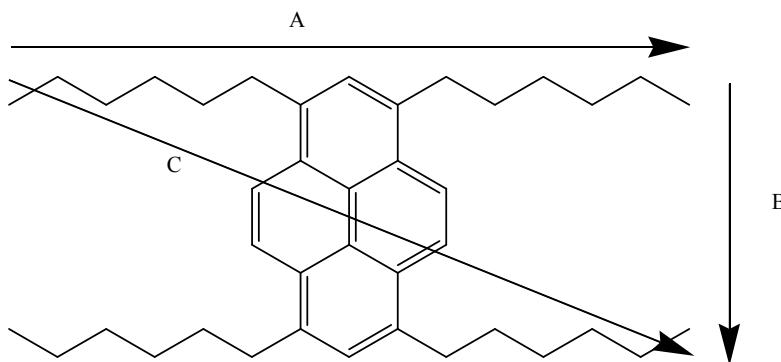
Figure 4-13: Three defined distances in Materials Studio software for size estimation of model compound

Table 4-1: The size of three defined distances for model compound at 430°C and vacuum

Distance	Length(nm)	Standard deviation
A	1.07	0.30
B	1.85	0.32
C	1.64	0.32

The unsupported sulfided iron sample was also used for comparison to confirm its activity in the suppression of addition reactions, as well as to verify the absence of mass transfer limitations, since its particle size (5 μm) was at least at order of magnitude lower than the particle size of the supported catalysts, but the same as the active phase cluster size in the Fe/α-Al$_2$O$_3$ sample. The choice of particle size for this unsupported catalyst was made based on the results of SEM/EDX of the Fe/ α-Al$_2$O$_3$ catalyst that showed the maximum size of clusters is around 4-5 micron. The error values in the parentheses are standard deviation of 3 replicates expect for unsupported sulfided iron (F) which is averages of two reactions. The yields in this table have not been normalized, and we estimate losses at less than 4%.

Table 4-2: Conversion and product yields for non-catalytic and catalytic reactions of tetrahexylpyrene in tetralin at 430°C, 13.9 MPa hydrogen, 30 min

Sample #[a]	A(N$_2$)	B(H$_2$)	C	D	E	F	G	H	I
Active sites	-	-	-	sulfided iron	sulfided iron	sulfided iron	sulfided iron	Unsupported sulfided iron	Ni-Mo sulfide
supports	-	-	γ-Al_2O_3	α-Al_2O_3	acid washed glass beads	unwashed glass beads	γ-Al_2O_3	-	γ-Al_2O_3
Metal loading (wt%) on support	-	-	0	2.54	2.54	2.54	2.54	-	2-4 Ni 12-15 Mo
Conversion (%)	78	80($\pm$4)	80	88 ($\pm$7)	83	80	87	90($\pm$4)	90($\pm$7)
Yield of addition products	63	63($\pm$2)	59	13($\pm$3)	22	24	15	13($\pm$2)	4($\pm$1)
Yield of cracking products	35	35($\pm$1)	39	85($\pm$2)	77	74	84	81 ($\pm$3)	84 ($\pm$3)
Yield of aromatic hydrogenation	0	0	0	0	0	0	0	3($\pm$1)	11($\pm$2)

[a]: Except for A and B, the mol/mol ratio of initial THP/active metal was 0.05 for all catalysts. For Ni-Mo, Ni is considered for calculations.

The observed product distribution is in agreement with the free radical chain reaction mechanism described in the Table 2-2 in the first chapter. In the β-scission steps (2-7), cracking occurs in the beta position of alkyl chains resulting in the formation of a radical and an olefin. The formed radical may participate in the hydrogen abstraction, radical rearrangement, and radical termination or in another β-scission step for other chains (reactions 2-6, 2-7, 2-9, and 2-10) yielding cracking products with lower molecular weight. The structure of cracked products was consistent with free radical mechanism in which methyl products were the most abundant remnants formed by loss of side chains accompanied with lower yield of methyl free analogous. The lowest yield was for pyrene which needs multiple cycles of side chains cracking and also hydrogen transfer.

If the olefin reacts with other radicals in the reaction environment through a radical addition (reaction 2-8), a larger size radical would form and if it abstracts hydrogen or participates in radical termination, addition products with higher molecular weight than parent compound will be formed, leading to coke formation.

Other possible pathways for the olefin are reactions (2-11) and (2-12), with donor solvent or in catalytic reactions. Finally, aromatic hydrogenation products may form by reaction (2-13), although low yield is observed in our work because of the low activity of iron sulfide.

In Figure 4-14, product yields for the reaction catalyzed by four sulfided Fe-based catalysts are compared. The sulfided iron catalyst supported on glass beads (E and F) had the highest yield of the addition reaction products compared to the alumina-supported catalysts (Table 4-2), therefore, they are omitted for further consideration as the least efficient catalyst. The addition reactions are significantly suppressed in the presence of the sulfided Fe catalysts, with 3-fold lower yield of the addition products as compared to the Fe-free reaction with the support presence (alumina, sample C). Within the experimental error, no appreciable difference could be seen between the sulfided iron supported on α-alumina, γ-alumina and unsupported catalyst. Also the product yields for Fe-free γ-alumina sample and the

non-catalytic reaction indicates that the support did not significantly promote activity of acid catalyzed cracking of THP and its addition products.

In all cases, and also for the reactions in the next section, the concentration of pyrene and short-alkylpyrene detected by GC-FID was no more than 4 % of the total cracking yields. Short-alkylpyrenes were mainly pyrene ring with one or two methyl groups on pyrene ring, and their concentration were 4 times more than pyrene. The corresponding peaks in GC-FID spectrum were very weak, furthermore they were close to noise level and identification and quantification of longer chain cracked products was impossible. Savage and Smith (4) studied pyrolysis of 1,3-bis(1-pyrene)propane (BPP) neat and in benzene solution. They identified pyrene as minor products in low conversions via cleavage of alkyl-aryl C-C bond, but at higher conversion, high yields of it were produced via secondary pathways involving dealkylation of alkylpyrenes formed in primary reactions. In their work the major primary pathway leads to methylpyrene and vinylpyrene, and a less important parallel primary pathway leads to pyrene, the minor products, and char. Secondary reactions include the rapid conversion of vinylpyrene to ethylpyrene (and possibly other products) and dealkylation of both ethylpyrene and methylpyrene to form pyrene. Thus, pyrene can be formed directly from BPP as a primary product, but its formation is largely from methylpyrene and ethylpyrene as a secondary product. The authors concluded that strong alkyl-aryl C-C bond could be broken even at low temperatures in absence of added H_2 and donor solvent by some mechanism of hydrogenolysis including radical hydrogen transfer (RHT) (5) or molecular disproportionation (MD). (6)

In this study, as it is mentioned before, the concentration of pyrene and short-alkyl pyrenes were very low compare to longer chain alkylpyrenes. We believe that the mechanism responsible for formation of these species is the same as Smith and Savage mechanism. It should be considered that because of two reasons we did not observe high yield of pyrene in our study: first, dilution of model compound in solvent by decreasing concentration and consequently rate of these reactions, and second presence of four side chains in model compound which can cause a steric hindrance effect. The required hydrogen for pyrene formation could

be provided from several abstractable hydrogen sources in the reaction environment such as: tetralin, hydrogen atoms of side chains and hydrogen gas.
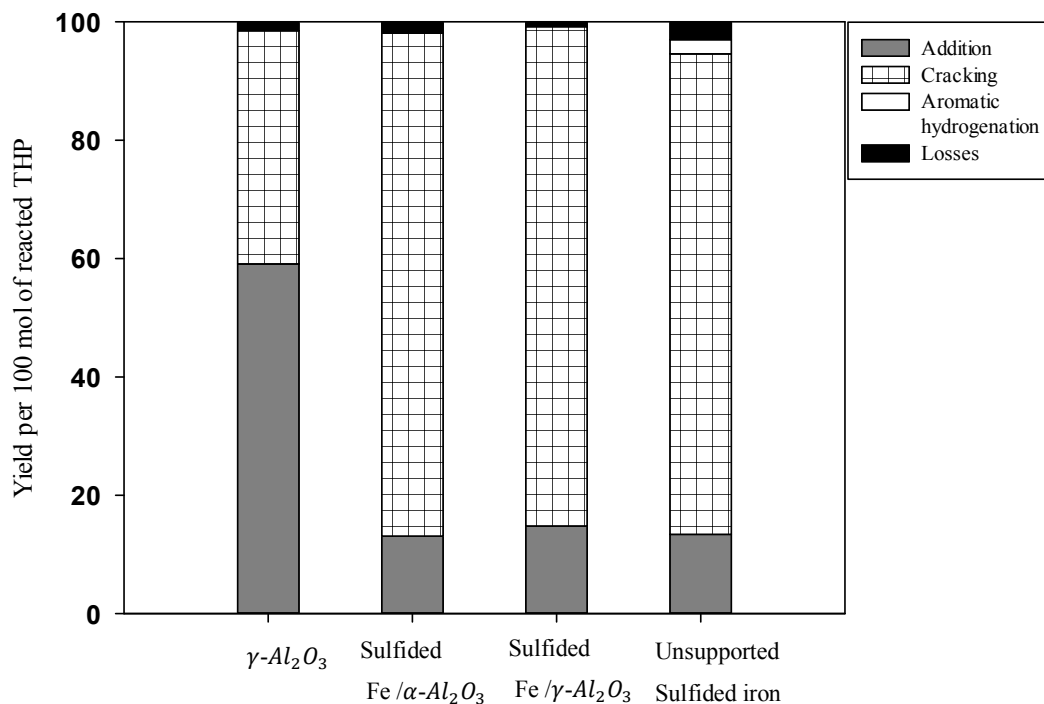

Figure 4-14: Comparison of iron based catalysts for the suppression of addition reaction, 430°C, 13.9 MPa, 30 min

4.2.5 Comparison with control experiments

The product yield for a sulfided Fe/α-Al$_2$O$_3$ is compared in Figure 4-15 with two control reactions: reaction without a catalyst (negative control) and with a commercial Ni-Mo sulfide catalyst (positive control). In the Table 4-2, there are no differences between catalyst free reaction in nitrogen and hydrogen (sample A and B), and the same conclusion was confirmed by Savage et al. (7), therefore sample (B) is selected for comparison. The catalyst presence did not impact conversion (Table 4-2) but significantly decreased the selectivity to the addition products from 63% in a non-catalytic reaction (B) to 13% for the sulfided Fe/α-Al$_2$O$_3$(D), with the commercial Ni-Mo catalyst being the most selective towards suppression of addition reactions. The latter catalyst was also active in the hydrogenation of

aromatics, as was confirmed from MALDI-MS results and also from ^{1}H-NMR spectra for pyrene as a test compound
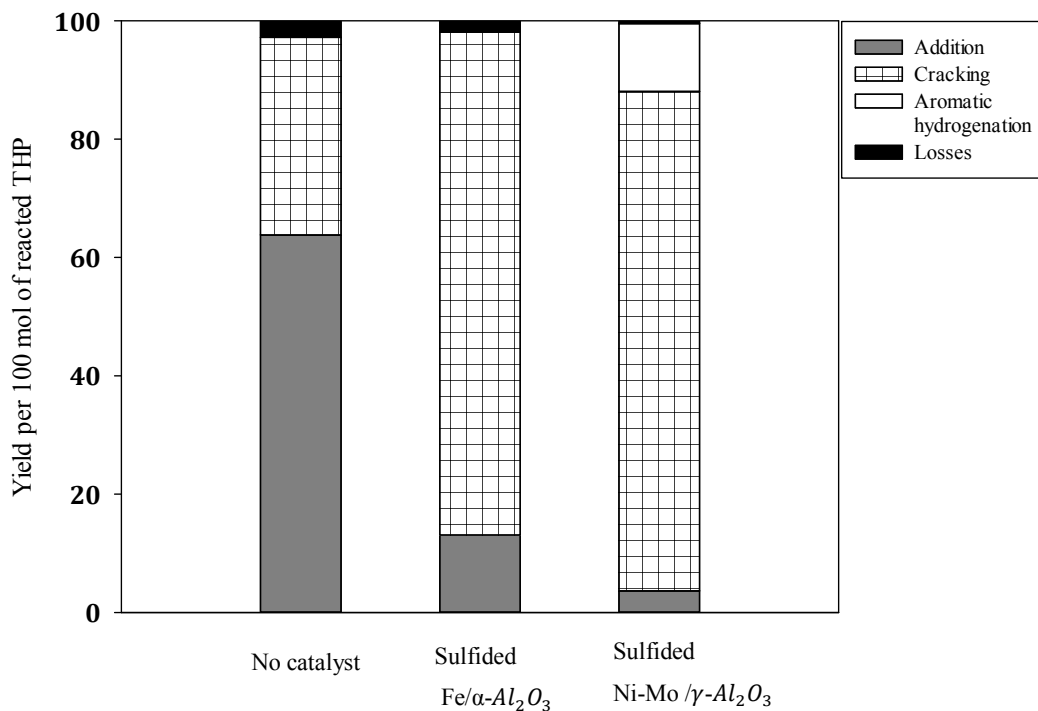
Figure 4-15: Comparison of product yields in the reactions with the sulfided Fe/α-Al$_2$ O$_3$ (D), no catalyst (B), and sulfided Ni-Mo (I) at 430°C, 13.9 MPa, 30 min

The MALDI-MS spectra of three selected reactions are shown in Figure 4-16 for no catalyst (I), Fe/α-Al$_2$O$_3$(II) and Ni-Mo/γ-Al$_2$O$_3$(III), where the change in intensities of addition peaks can be seen.
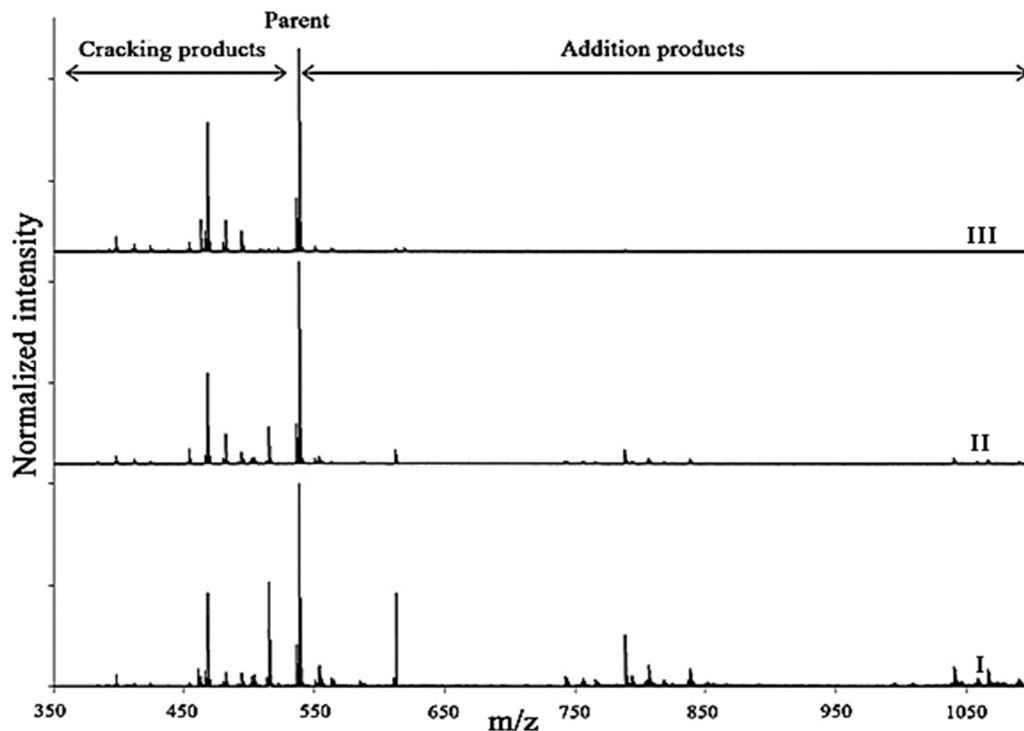
Figure 4-16: MALDI-MS spectra for THP showing addition and cracking region for the reactions with no catalyst (I), and sulfided Fe/α-Al$_2$O$_3$ (II) and Ni-Mo/γ- Al$_2$O$_3$ (III) catalysts. Reaction conditions: 430℃, 13.9 MPa, 30 min

The data show that the catalysts had no statistically significant impact on the conversion of the parent THP (80±4% for non-catalytic versus 88±7% for sulfided Fe/α-Al$_2$O$_3$); However, Student t-Test can help to better see whether there is a significant difference in the means. The probability associated with a Student's t-Test with assumption of unequal standard deviations and with a two-tailed distribution is calculated between sulfided iron and non-catalytic and also Ni-Mo and non-catalytic samples. The results of p-value for conversions are 0.10 and 0.17 respectively. All these numbers are more than 0.05, showing that, there is no evidence to reject null hypothesis of t-test which is the equality of conversions with 95% confidence; consequently despite suppressing the consumption of the parent compound in addition reaction yet the same conversion values were observed. If the formation of the THP radical is the rate limiting step, giving either beta scission or addition, then the sulfided catalysts would have an importance effect to shift the mechanism from addition to beta scission step without affecting conversion.

94

The insensitivity of the conversion to the presence of catalyst is inconsistent with the claims that the radicals are efficiently hydrogenated by these catalysts. (8, 9) If radicals are hydrogenated by the catalyst, then the catalyst adds a significant termination step, and the concentration of radical species goes down. A reduction in the concentration of radicals will reduce conversion. Another explanation can be suggested by considering the activation energies: The observed activation energy of cracking of similar pyrene based model compounds was reported in the range of 170-200 kJ/mol (4, 10, 11) that is lower than the bond dissociation energy required for initiation (Reaction 2-5 in Table 2-2). Although the activation energy is not measured for cracking of THP, it is expected to be in the same range. Lower activation energies of the propagation steps (hydrogen abstraction and β-scission) contribute to the low observed activation energy. If we assume in the current work that the Fe catalyst promotes radical hydrogenation, the propagation steps would be suppressed, resulting in higher energy requirement and, thus, lower conversion. Since the catalyst did not contribute to the conversion decrease, the hypothesis of the radical hydrogenation may be rejected. Therefore, the suggested role of catalyst is in hydrogenation of intermediate olefins to stop further reactions between them and the free radicals. Such removal of olefins controls the addition reactions and may lead to the suppression of coke formation. (12, 13)

Likewise, our data do not support the claims of Yoneyama and Song (8) for catalytic hydrogenolysis of C-C bonds with Mo sulfide, and there was no evidence for presence of metallic catalyst which are active for hydrogenolysis in their samples. Opening up a new pathway would always be expected to increase conversion but this increase was not observed in catalytic reactions with commercial Ni-Mo on alumina. The lack of hydrogenolysis of C-C bonds that we observe in this study is consistent with the large literature on catalytic hydrotreating, which gives no evidence for significant dealkylation due to catalytic breakage of C-C bonds.

4.3 ^{1}H-NMR spectroscopy experiments

To investigate the catalyst activity in aromatic hydrogenation of THP, ^{1}H-NMR spectroscopy was used for three reaction product samples: no catalyst (I), Fe/α-Al$_2$O$_3$(II) and Ni-Mo/γ-Al$_2$O$_3$(III). In this set of experiments pyrene was used instead of THP for two reasons: first, high concentration of compound was required for NMR analysis while the quantity of available model compound was limited and second, presence of side chains in THP and their participation in addition reaction caused overlapping of peaks in NMR spectra. The aromatic region of the spectra is shown on Figure 4-17.

For samples of (I) and (II) the amount of pyrene decreased less than 3 percent, which is expected to be loss of sample during extraction, handling and solvent evaporation. For sample (III) the conversion was 82 %. The ^{1}H-NMR spectra shows that sulfided Fe/α-Al$_2$O$_3$catalyst (II) had little activity for hydrogenation of pyrene, which was the same as for the non-catalytic reaction control (I). Alternatively, the spectrum for Ni-Mo-catalyzed reaction (III) showed peaks of hydrogenated pyrene and mostly 4,5-dihydropyrene, that was also confirmed by GC-MS as well. These data suggest that the sulfided Fe/α-Al$_2$O$_3$ is not active for aromatic hydrogenation under the selected conditions.
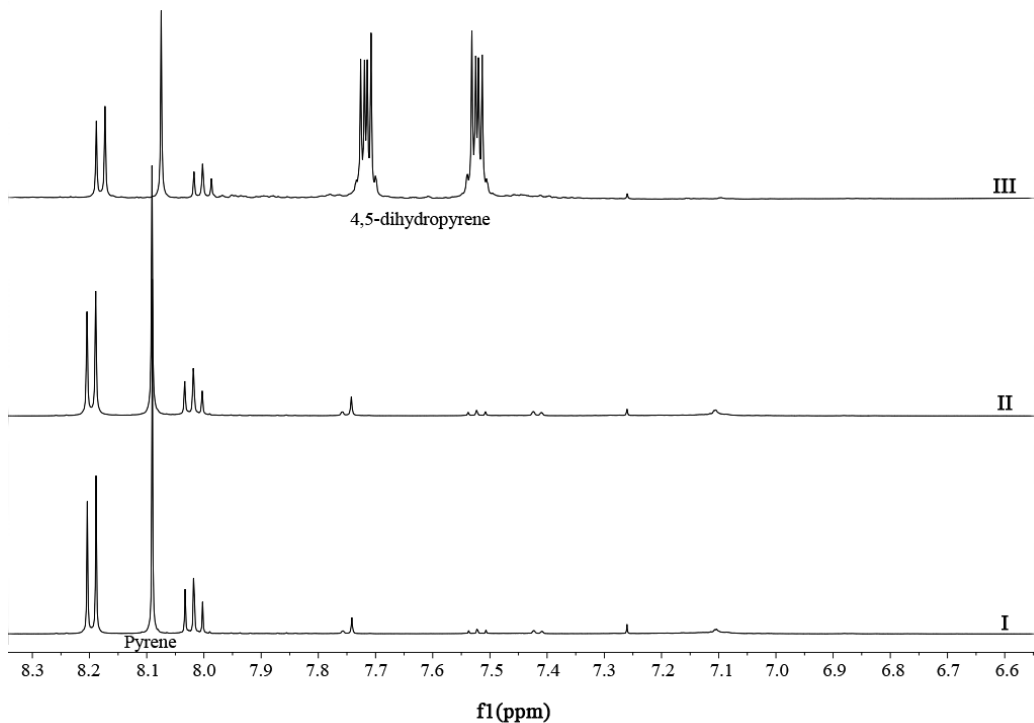
Figure 4-17: Aromatic region of ^{1}H-NMR spectra for hydrogenation of pyrene with no catalyst (I), and sulfided Fe/α-Al$_2$O$_3$ (II) and Ni-Mo/γ- Al$_2$O$_3$ (III) catalysts. Reaction conditions: 430℃, 13.9 MPa, 30 min

4.4 Catalyst Characterization

Figure 4-18 and Figure 4-19 show SEM and EDX mapping images of the sulfided Fe/α-Al$_2$O$_3$ catalyst before the catalytic reaction. The sulfided iron clusters appear as 4-5 μm in size. The loci of Fe and S coincide, suggesting successful sulfidation of Fe in the catalyst. Three types of distributions for active sites in catalyst based on mapping mode imaging were observed: 1) clusters rich of iron and sulfur which are formed due to sintering of active metal, 2) randomly distributed sites and 3) some loci with the concentration lower than the detection threshold of equipment(<0.5 wt %).

97
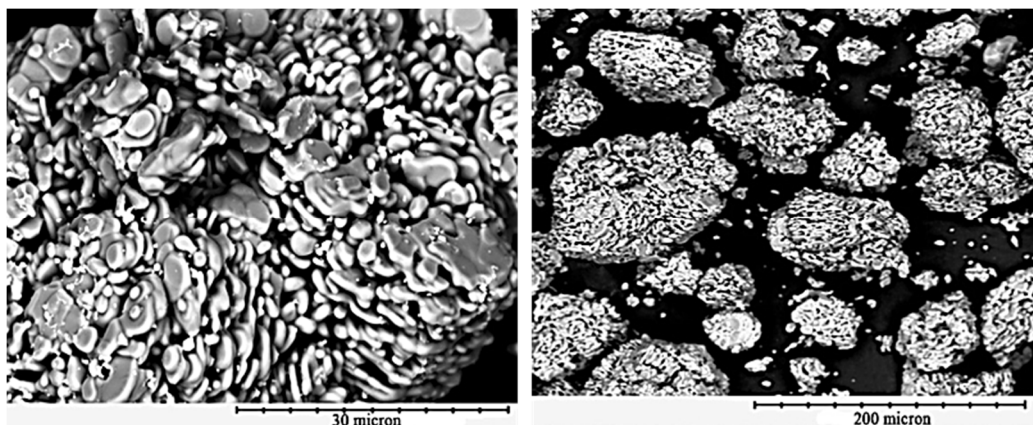
**Figure 4-18**: Back-scattered SEM images of the sulfided Fe/α- Al_2O_3 before the catalytic reaction
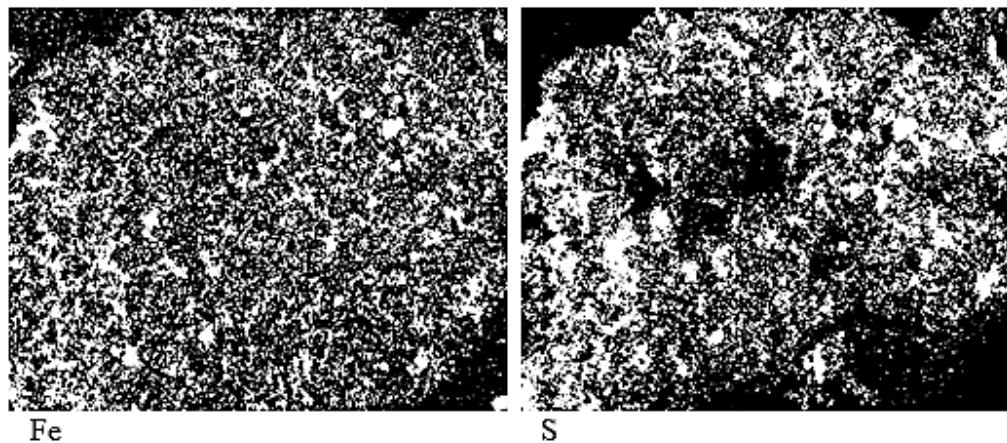
Figure 4-19: Location of iron (left) and sulfur (right) in the sulfided Fe/α- Al_2O_3 by EDX mapping mode

Table 4-3 shows the elemental composition with 1.6 S-to-Fe atomic ratio, which is consistent with the three types of the observed sites.

Table 4-3: Average elemental composition of the sulfided Fe/α- Al_2O_3 catalyst before the reaction from SEM/EDX

	Fe	S	Al	O
Weight %	2.6	2.4	48.0	47.1
Atomic %	1.0	1. 6	36.7	60.8

98

The XRD patterns of the catalyst before and after catalytic reaction are shown in Figure 4-20. Sulfided iron was in pyrite (FeS$_2$) form before the reaction and during reaction it was converted to Pyrrhotite (Fe$_{1-x}$S).
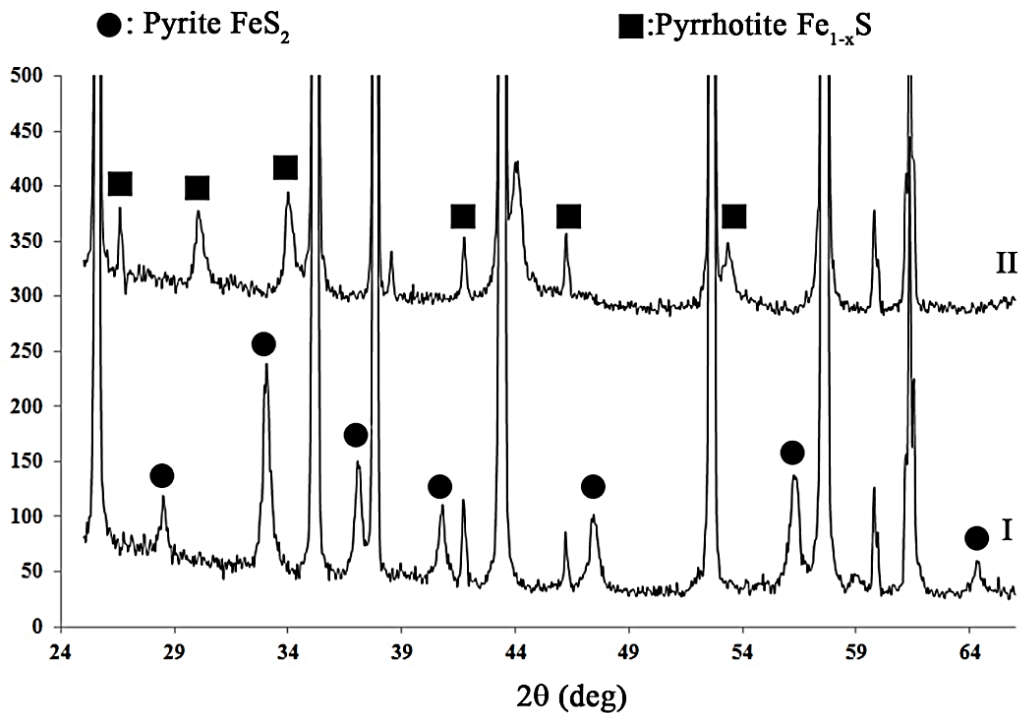
**Figure 4-20**: XRD patterns of the sulfided Fe/α- Al$_2$O$_3$ before (I) and after the catalytic reaction (II) at 430℃, 13.9 MPa, 30 min

The profiles of high resolution XPS are shown in Figure 4-21 and Figure 4-22 for iron (Fe2p) and sulfur (S2p), respectively. The Fe spectrum shows that although there was some metallic and oxidized Fe before the reaction, it converted to the sulfided iron after the reaction. The same trend was seen for sulfur too, the sulfur was in disulfide state before reaction but during reaction it changed to the sulfide. These observations are consistent with the XRD results about the change in the crystalline structure after reaction to pyrrhotite.
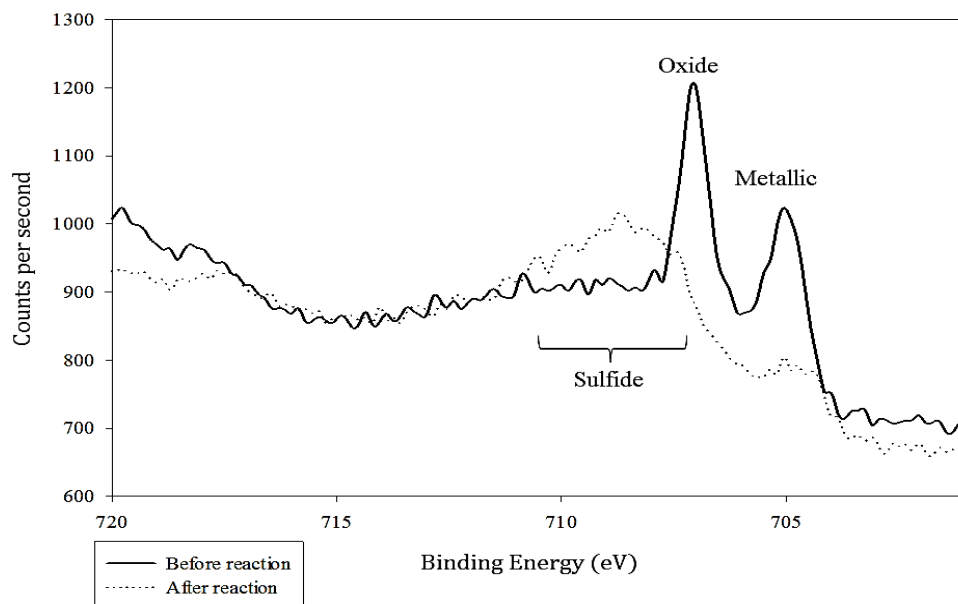
Figure 4-21: High resolution XPS spectra of sulfided Fe/α- Al$_2$O$_3$ before and after the reaction at 430℃, 13.9 MPa, 30 min
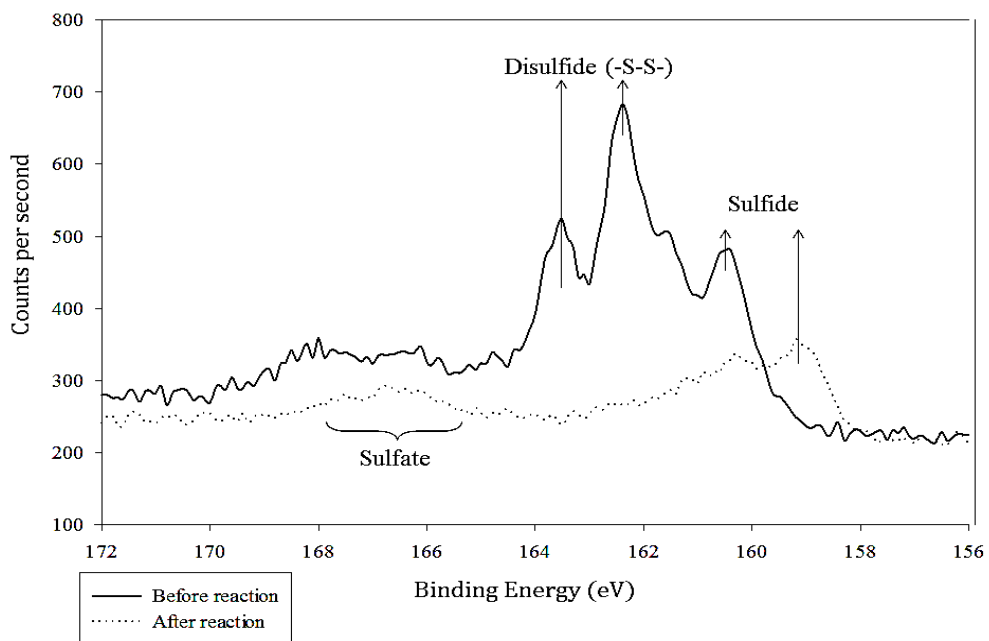
Figure 4-22: High resolution XPS spectra of sulfur in sulfided Fe/α-Al$_2$O$_3$ before and after the reaction at 430℃, 13.9 MPa, 30 min

The sulfided Fe/α-Al$_2$O$_3$ catalyst undergoes a change in chemical state of iron and sulfur during the reaction as evidenced both from XRD and XPS, which is consistent with earlier proposed hydrogenation mechanism on the sulfided metals, i.e., a metal atom should be exposed to the reactant after the sulfur vacancy had been created in hydrogen atmosphere. (14-18) Huffman et al. (19) also observed that the pyrrhotite content of catalysts obtained after direct coal liquefaction in a hydrogen atmosphere increased, as was shown by the Mössbauer and EXAFS spectroscopic analysis of the catalysts.

4.5   References

1. Mierau JM. Patterns and pathways of hydrogenation of asphaltene model compounds [dissertation]. University of Alberta; 2011.

2. Khorasheh F, Gray M. High-pressure thermal-cracking of N-hexadecane in tetralin. Energy Fuels. 1993;7(6):960-7.

3. Khorasheh F, Gray M. High-pressure thermal-cracking of N-hexadecane. Ind Eng Chem Res. 1993;32(9):1853-63.

4. Smith C, Savage P. Reactions of polycyclic alkylaromatics .2. pyrolysis of 1,3-diarylpropanes. Energy Fuels. 1991;5(1):146-55.

5. McMillen D, Malhotra R, Chang S, Ogier W, Nigenda S, Fleming R. Mechanisms of hydrogen transfer and bond scission of strongly bonded coal structures in donor solvent systems. Fuel. 1987;66(12):1611-20.

6. Billmers R, Brown R, Stein S. Hydrogen transfer from 9,10-dihydrophenanthrene to anthracene. Int J Chem Kinet. 1989;21(6):375-86.

7. Savage P, Klein M, Kukes S. Asphaltene reaction pathways .3. effect of reaction environment. Energy Fuels. 1988;2(5):619-28.

8. Yoneyama Y, Song C. A new method for preparing highly active unsupported mo sulfide. catalytic activity for hydrogenolysis of 4-(1-naphthylmethyl)bibenzyl. Cat. Tod. 1999;50(1):19-27.

9. Sasaki M, Song C, Plummer M. Transition metal tetrachloroaluminate catalysts for probe reactions simulating petroleum resids upgrading. Fuel. 2000;79(3-4):295-303.

10. Alshareef AH, Scherer A, Tan X, Azyat K, Stryker JM, Tykwinski RR, et al. Effect of chemical structure on the cracking and coking of archipelago model compounds representative of asphaltenes. Energy Fuels. 2012;26(3):1828-43.

11. Freund H, Matturro M, Olmstead W, Reynolds R, Upton T. Anomalous side-chain cleavage in alkylaromatic thermolysis. Energy Fuels. 1991;5(6):840-6.

12. Gray M, McCaffrey W. Role of chain reactions and olefin formation in cracking, hydroconversion, and coking of petroleum and bitumen fractions. Energy Fuels. 2002;16(3):756-66.

13. Weisser O, Landa S. Hydrogenation of unsaturated hydrocarbons. In: Sulphide catalysts, Their properties and applications. 1st ed. Prague: Pergamon Press; 1973. p. 118-24.

14. Ogawa T, Stenberg V, Montano P. Hydrocracking of diphenylmethane roles of H2s, pyrrhotite and pyrite. Fuel. 1984;63(12):1660-3.

15. Hei R, Sweeny P, Stenberg V. Mechanism of the hydrogen-sulfide-promoted cleavage of the coal model compounds - diphenyl ether, diphenylmethane and bibenzyl. Fuel. 1986;65(4):577-85.

16. Montano P, Stenberg V, Sweeny P. Insitu study of the hydrogenation of diphenyl ether in the presence of pyrrhotite and H2s. J Phys Chem. 1986;90(1):156-9.

17. Baldwing R, Vinciguerra S. Coal-liquefaction catalysis - iron pyrite and hydrogen-sulfide. Fuel. 1983;62(5):498-501.

18. Thomas M, Padrick T, Stohl F, Stephens H. Decomposition of pyrite under coal-liquefaction conditions - a kinetic-study. Fuel. 1982;61(8):761-4.

19. Huffman G, Ganguly B, Zhao J, Rao K, Shah N, Feng Z, et al. Structure and dispersion of iron-based catalysts for direct coal-liquefaction. Energy Fuels. 1993;7(2):285-96.
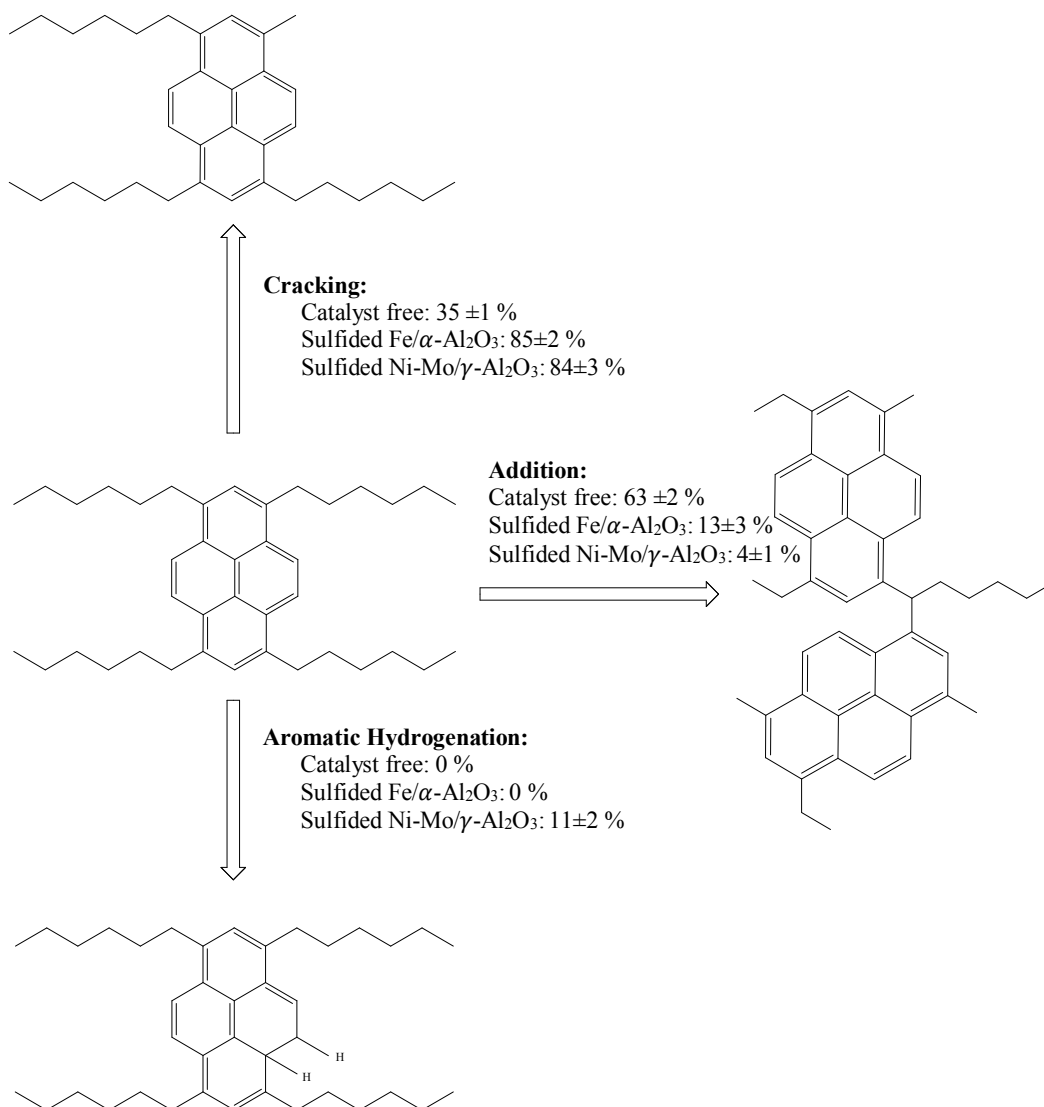
CHAPTER 5

Implications and Conclusions

5.1   Summary of catalytic reactions of 1,3,6,8-tetrahexylpyrene

Our hypothesis was that the low-hydrogenation-activity sulfided iron catalyst can effectively suppress addition reactions in asphaltene hydroconversion via hydrogenation of intermediate olefins. This working hypothesis was verified for the hydroconversion of 1,3,6,8-tetrahexylpyrene as an asphaltene model compound using tetralin as a hydrogen donor solvent at 430°C and 13.9 MPa of H_2 in a batch microreactor with and without sulfided Fe catalysts. The reaction products were analyzed via GC-FID, GC-MS, MALDI-MS, ^{1}H-NMR spectroscopy and HPLC to obtain THP conversion and product yields for possible pathways.

In Figure 4-11, the main reaction pathways and representative structures of the most abundant products of each pathway are shown. The values show how using sulfided Fe/α-Al$_2$O$_3$ and sulfided Ni-Mo/γ-Al$_2$O$_3$ changed the product distribution. Iron catalyst can suppress addition reactions from 63 % to 13 %, most likely by hydrogenation of olefin intermediates, while Ni-Mo catalyst as a commercial catalyst with more active metals resulted in both suppression of addition reactions and hydrogenation of aromatics as well.

Cracking:
Catalyst free: 35 ±1 %
Sulfided Fe/α-Al$_2$O$_3$: 85±2 %
Sulfided Ni-Mo/γ-Al$_2$O$_3$: 84±3 %

Addition:
Catalyst free: 63 ±2 %
Sulfided Fe/α-Al$_2$O$_3$: 13±3 %
Sulfided Ni-Mo/γ-Al$_2$O$_3$: 4±1 %

Aromatic Hydrogenation:
Catalyst free: 0 %
Sulfided Fe/α-Al$_2$O$_3$: 0 %
Sulfided Ni-Mo/γ-Al$_2$O$_3$: 11±2 %

Figure 5-1: Schematic of the main products from each detected pathways of the THP reaction and their yields on a mol basis per 100 mol of reacted model compound

104

5.2 Implications

This study defines the value of low-cost iron catalyst, as compared to commercial nickel-molybdenum based catalysts, as an additive to reduce amount of coke formation in the thermal cracking processes in the presence of hydrogen. By avoiding the growth of higher molecular weight products, the separation of the coke phase can be suppressed.

One important advantage of iron over Mo sulfide catalysts is due to low activity of iron, it can avoid over hydrogenation which results in preventing reduction in solubility parameter of liquid phase. Therefore it can help to stabilize the liquid phase and prevent the separation of mesophase prior to coke formation.

A good example of the application of iron sulfide catalyst can be found in the work of Dehkissia et al.(1) To transfer the heavy oil from Doba-Chad oil fields in Chad to the Cameron ports for shipping, the viscosity of the oil must be reduced from 184 cSt to 25 cSt at 50℃ to meet the requirements of transfer by pipeline. Between different solutions such as heating of pipe, addition of diluent and pipeline booster, using catalytic hydrovisbreaking unit with iron sulfide catalyst was selected. A combination of distillation, hydrovisbreaking and deasphalting units reduced the viscosity to 21 cSt. According to the relation of viscosity and molecular weight, a reduction in viscosity after catalytic upgrading means that the feed is cracked into smaller size compounds without formation of addition products and iron sulfide catalyst was effective for this purpose.

In this project, both unsupported and supported sulfided iron catalyst were tested. The comparison would bring the discussion about whether presence of support is necessary or unsupported iron sulfide would be satisfactory. The data showed that they have likely same influence on conversion and product distribution, therefore operation and design factors must be determining for selection of proper catalyst. Using nanoparticle catalysts needs design of slurry

reactors over fixed bed or fluidized bed for supported metals in a three phase system. The slurry reactor has the advantages of excellent heat transfer, online catalyst addition and withdrawal, lower pressure drop, and less external diffusion limits while operation of fixed bed reactors are easier and the separation of ultra-fine particles from liquid phase for viscous liquids could be challenging. (2,3) Considering the size of molecules in asphaltenes and heavy oil fractions, diffusion of reactant to the pores of supports is unlikely and difficult and this was the reason for using low-porous or non-porous catalysts in our study; therefore, using iron sulfide nanoparticles in slurry reactor can be better approach than supported iron sulfide in fixed bed reactor if we could overcome the problems associated with fine particles.

And finally, by suppression of addition reactions, products of thermal cracking reactions would be smaller in size and easier for further hydrotreating processes.

5.3   Conclusions

1- Catalyst characterization experiments confirmed formation of sulfided iron on the catalyst surface and change in its crystalline structure from pyrite to pyrrhotite during reaction. Therefore, pyrrhotite is the active state of sulfided iron which has contact with model compound.

2- The pyrrhotite catalyst allowed lower yield of addition reaction products (13% vs. 63% in non-catalytic reactions), without promoting aromatic hydrogenation.

3- Alumina supports gave better suppression of addition reactions than glass beads supports. In addition, results of catalyst free-alumina and unsupported sulfided iron samples showed that the supports are not active for hydrogenation.

4- The independence of THP conversion on the catalyst presence contradicts the claims that radicals are efficiently hydrogenated by these catalysts,

because that would lead to the suppression of chain reactions and would cause a drop in conversion.

5.4 References

1. Dehkissia S, Larachi F, Rodrigue D, Chornet E. Lowering the viscosity of doba - chad heavy crude oil for pipeline transportation - the hydrovisbreaking approach. Energy Fuels. 2004;18(4):1156-68.

2. Wang T, Wang J, Jin Y. Slurry reactors for gas-to-liquid processes: A review. Ind Eng Chem Res. 2007;46(18):5824-47.

3. Tang Y, Curtis CW. Activity and selectivity of slurry-phase iron-based catalysts for model systems. Energy and Fuels. 1994;8(1):63-70.

APPENDIX A

HPLC Calculations and Chromatograms

This appendix details the calculations performed on HPLC chromatograms to obtain the feed model compound concentration remaining after the reaction, Included: the chromatograms, calibrations curves and formulae needed to do so.

1 HPLC Calibration Curve Calculations

HPLC calibrations curves were constructed for model compound concentration measurement. Calibration curves were made by tabulating the measured signal response, i.e. peak area, of a known quantity of analyte at differing concentration. Table A-2 and Table A-3 are examples of the data obtained to construct a

calibration curve. The internal standard response factor, RF, is defined by the following:

$$RF = \frac{A_s}{A_{THP}} \frac{W_{THP}}{W_s}$$

(A-1)

where A_S and A_{THP} are the internal standard and model compound peak areas and W_S and W_{THP} are the internal standard and model compound masses in the sample solution.

The calibration curves are the resulting plot of model compound mass vs. the ratio of model compound peak area to the internal standard response factor multiple by mass of internal standard. If the signal response (the aforementioned ratio) has a linear relationship with model compound mass then a linear regression can be obtained from the calibration curve. Model compound mass can then be calculated from these linear regressions directly. Data were obtained at two wavelengths of 239 and 279 nm which had the maximum absorbance for model compound and internal standard respectively. The intercepts of linear regression were set to zero. The calibration curves used in this work are presented in Figure A-1and Figure A-2, with the resulting linear regression equations listed in Table A-1.

$$W_{THP} = RF.W_s.\frac{A_{THP}}{A_s}$$

(A-2)

Table A-1 Calibration curve linear regression equations and error

Wavelength	Linear Regression Equation $y = ax + b$		R^2
	m	b	
270 nm	16.741	0	0.9978
239 nm	1.0976	0	0.9954

Table A-2 Calibration curve data for 1,3,6,8-tetrahexylpyrene at wavelength 270 nm

Sample	Mass of model compound (mg)	Model compound peak area (mAU.s)	Internal Standard Mass (mg)	Internal Standard Peak Area (mAU·s)	Ratio of model compound peak area to internal standard peak area multiple by mass of internal standard (mg)
1	2.12	385	0.66	2034	0.1269
2	2.04	2514	1.01	20920	0.1222
3	1.80	321	0.56	1652	0.1092
4	1.06	169	0.33	927	0.0616
5	1.02	1304	0.50	10855	0.0611
6	0.53	88	0.16	529	0.0274
7	0.51	663	0.25	5517	0.0305

Table A-3 Calibration curve data for 1,3,6,8-tetrahexylpyrene at wavelength 239 nm

Sample	Mass of model compound (mg)	Model compound peak area (mAU.s)	Internal Standard Mass (mg)	Internal Standard Peak Area (mAU·s)	Ratio of model compound peak area to internal standard peak area multiple by mass of internal standard (mg)
1	2.12	1680	0.66	588	1.93
2	2.04	11733	1.01	6401	1.86
3	1.80	1428	0.56	478	1.67
4	1.06	723	0.33	266	0.92
5	1.02	5818	0.50	3174	0.93
6	0.53	364	0.16	149	0.39
7	0.51	2935	0.25	1601	0.46
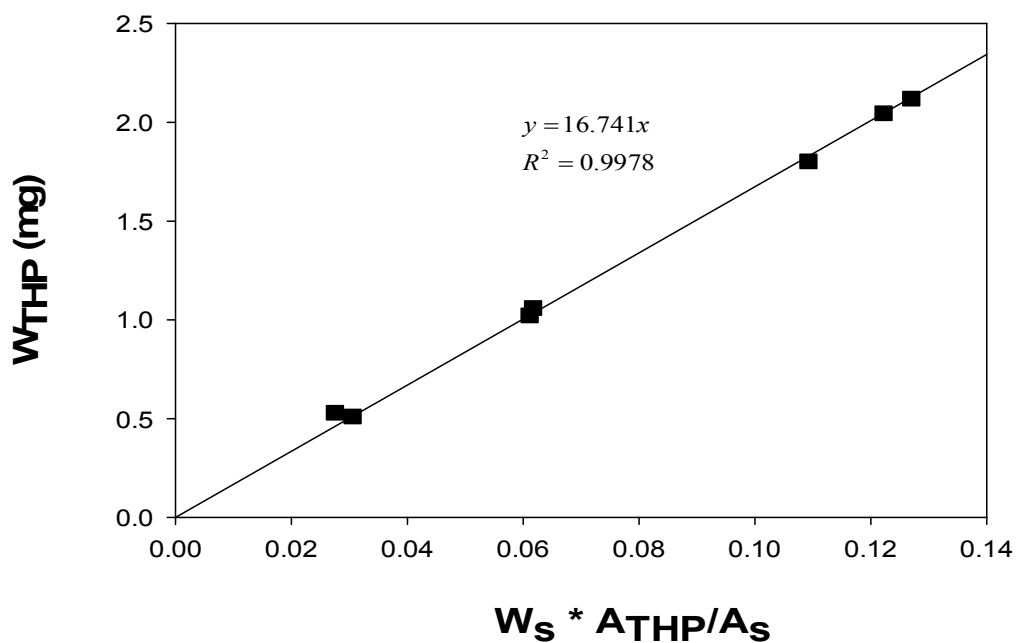
Figure A-1 HPLC calibration curve of for 1,3,6,8-tetrahexylpyrene at 270 nm
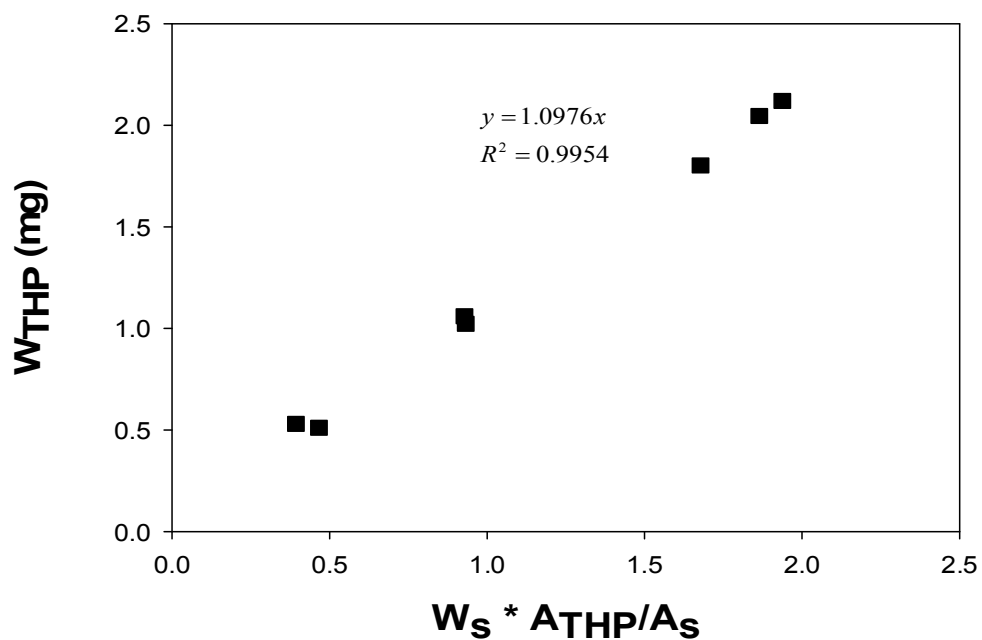
Figure A-2 HPLC calibration curve of for 1,3,6,8-tetrahexylpyrene at 239 nm

2   HPLC Chromatograms

The following are examples of the chromatograms used for calibration curve and also for 3 reaction samples (no catalyst, iron sulfide/α-alumina and Ni-Mo sulfide/γ-alumina):
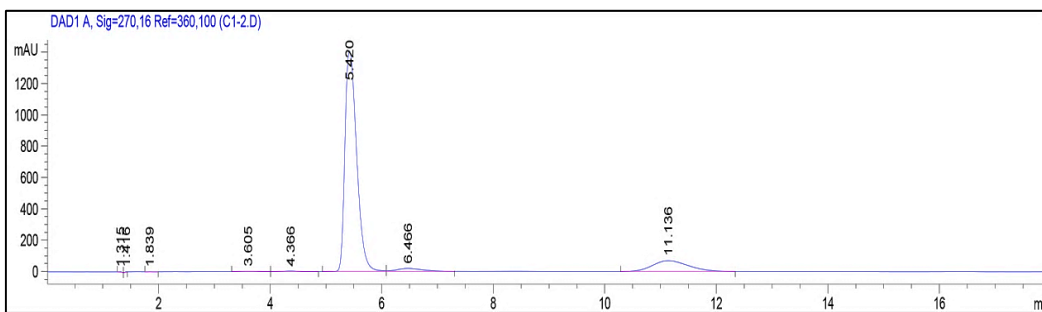
Figure A-3 Chromatogram of 2.04 mg of 1,3,6,8-tetrahexylpyrene in a mixture with 1.01 mg of benzo[*a*]pyrene at 270 nm
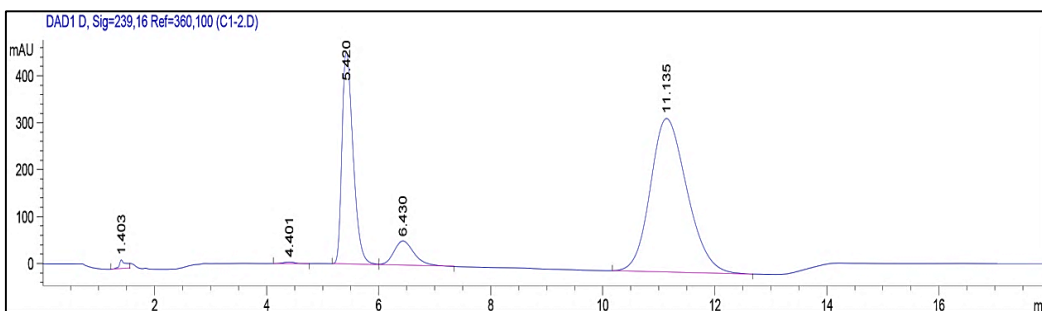
Figure A-4 Chromatogram of 2.04 mg of 1,3,6,8-tetrahexylpyrene in a mixture with 1.01 mg of benzo[*a*]pyrene at 239 nm
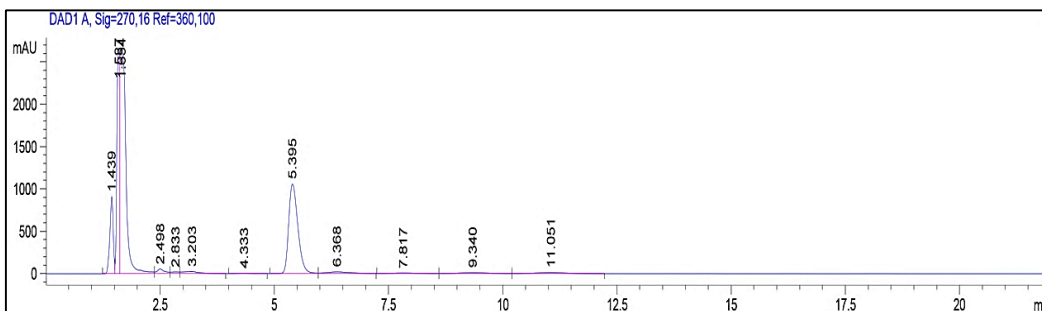
Figure A-5 Chromatogram of 1,3,6,8-tetrahexylpyrene reaction products with no catalyst and 1.136 mg of benzo[*a*]pyrene at wavelength 270 nm
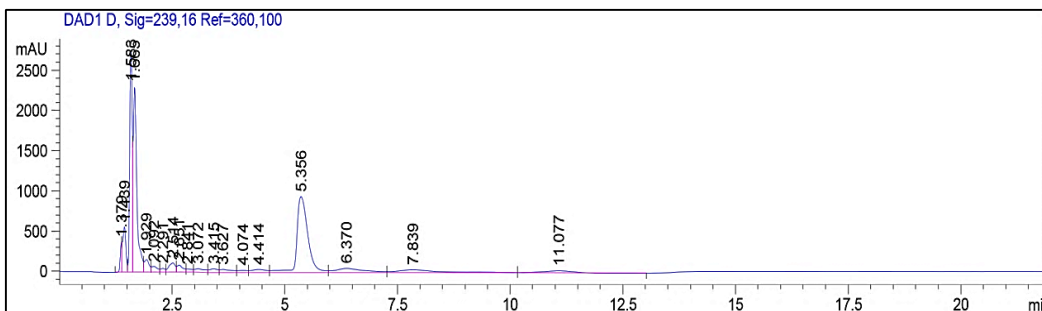
Figure A-6 Chromatogram of 1,3,6,8-tetrahexylpyrene reaction products with no catalyst and 1.136 mg of benzo[*a*]pyrene at wavelength 239 nm
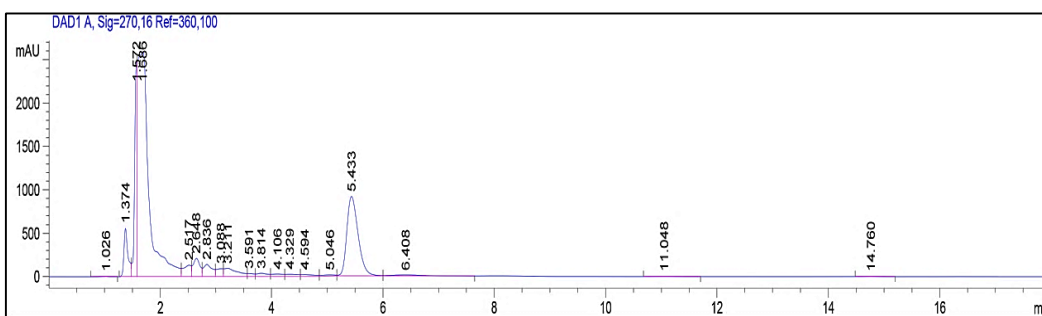
Figure A-7 Chromatogram of 1,3,6,8-tetrahexylpyrene reaction products with sulfided iron /α-alumina catalyst and 1.188 mg of benzo[*a*]pyrene at wavelength 270 nm
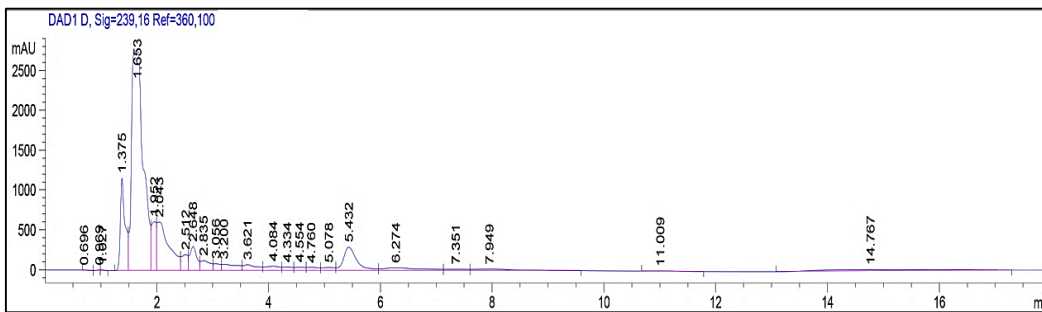
Figure A-8 Chromatogram of 1,3,6,8-tetrahexylpyrene reaction products with sulfided iron /α-alumina catalyst and 1.188 mg of benzo[*a*]pyrene at wavelength 239 nm
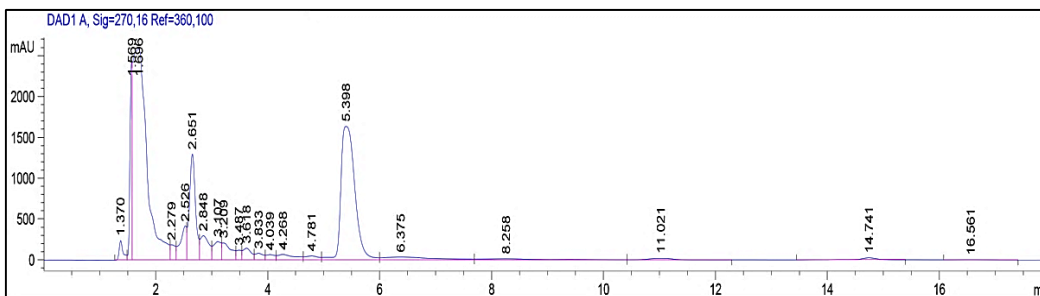
Figure A-9 Chromatogram of 1,3,6,8-tetrahexylpyrene reaction products with Ni-Mo sulfide/γ-alumina catalyst and 1. 884 mg of benzo[*a*]pyrene at wavelength 270 nm
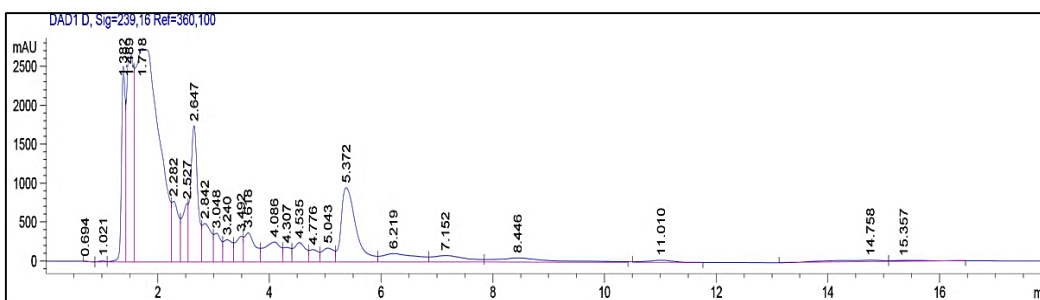
Figure A-10 Chromatogram of 1,3,6,8-tetrahexylpyrene reaction products with Ni-Mo sulfide/γ-alumina catalyst and 1. 884 mg of benzo[*a*]pyrene at wavelength 239 nm

APPENDIX B

GC Calculations and Chromatograms

This appendix details the calculations performed on GC chromatograms to obtain the concentration of pyrene and short alkylpyrenes in the reaction product mixtures,\ and also for ^{1}H-NMR, included are the chromatograms and formulae needed to do so.

1   GC Calibration Curve Calculations

The results obtained from GC-MS shows that pyrene and short alkylpyrenes were present in reaction product mixture. Calibration curve by GC-FID was made

to find mass of these compounds. It is assumed that response factor is the same for pyrene and alkylpyrenes. The response factor can be calculated from the internal standard and analyte peak areas and mass of internal standard from the following:

$$W_P = RF^{GC}.W_S.\frac{A_P}{A_S} \qquad \text{(B-1)}$$

where A_S and A_P are the internal standard and model compound peak areas and W_S and W_P are the internal standard and model compound mass in the sample solution.

Table B-1 shows the data for calibration curve of GC-FID using pyrene as analyte and benzo(a)pyrene as internal standard. The response factor was determined by linear regression of mass of pyrene versus the ratio of pyrene peak area to benzo(a)pyrene peak area multiple by mass of internal standard. The intercept of line was set to zero in the calculations. The calculated response factor was 0.6291.

The calibration curve used in this work is presented in Figure B-1.
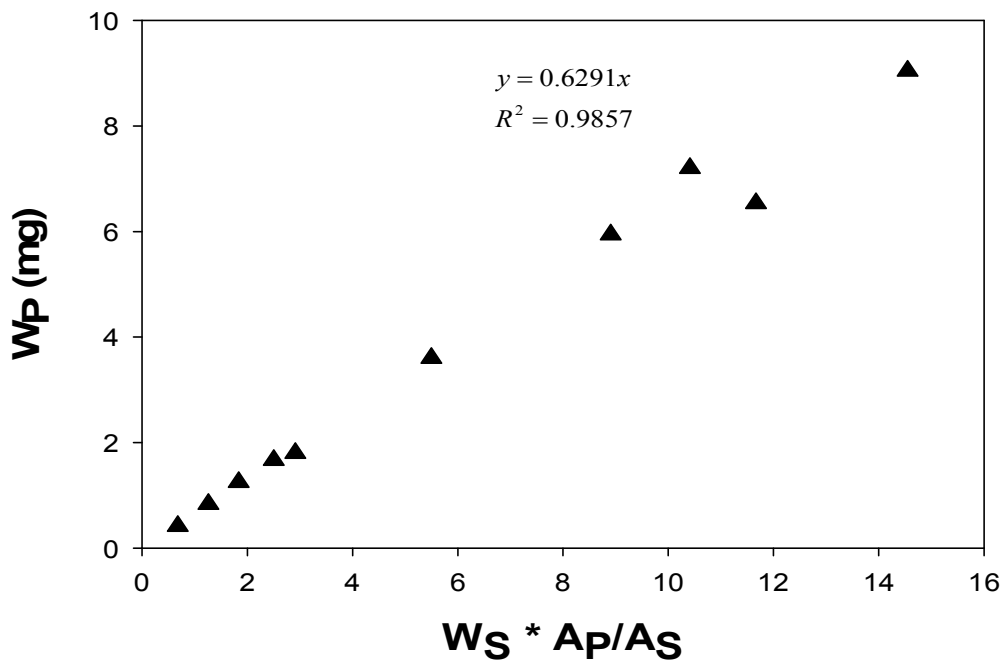
Figure B-1 GC-FID calibration curve of for pyrene

Table B-1 List of data required for GC-FID calibration curve

Sample	Mass of Pyrene (mg)	Pyrene peak area (arbitrary unit)	Internal Standard Mass (mg)	Internal Standard Peak Area (arbitrary unit)	Ratio of pyrene peak area to internal standard peak area multiple by mass of internal standard (mg)
1	9.04	141375153.5	2.48	24137282	14.54
2	6.53	125547650	1.92	20734529	11.66
3	7.201	1385762103	2.67	355598329	10.41
4	5.94	218951405	2.24	55272663	8.90
5	3.60	1319115696	1.33	320726283	5.49
6	1.80	743699443	0.66	170529463	2.91
7	1.66	778287154	1.34	419840180	2.50
8	1.25	634405990	1.01	349682236	1.83
9	0.83	484186767	0.67	259275758	1.25
10	0.41	253190074	0.33	126197792	0.67

1 GC Chromatograms

The following are the GC chromatograms used in this study: Figure B-2 is one example of calibration curve, Figure B-3 and Figure B-4 are samples of 1H-NMR with and without internal standard, Figure B-5 to Figure B-7 are three examples of chromatograms of reaction products and Figure B-8 is the chromatogram of iron sulfide/α-alumina between 23-37 minute to show pyrene and short alkylpyrenes.
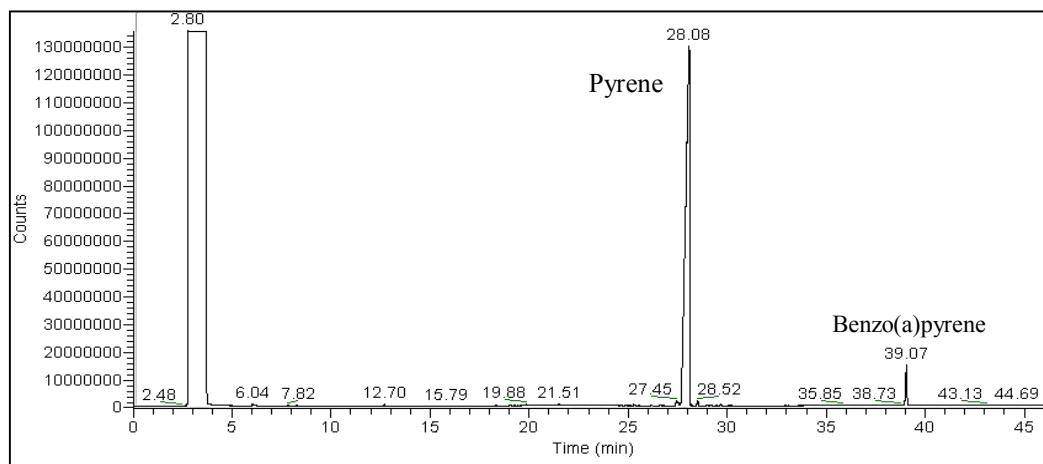
Figure B-2 Chromatogram of 5.94 mg pyrene in the mixture with 2.24 mg of benzo(a)pyrene for calibration curve
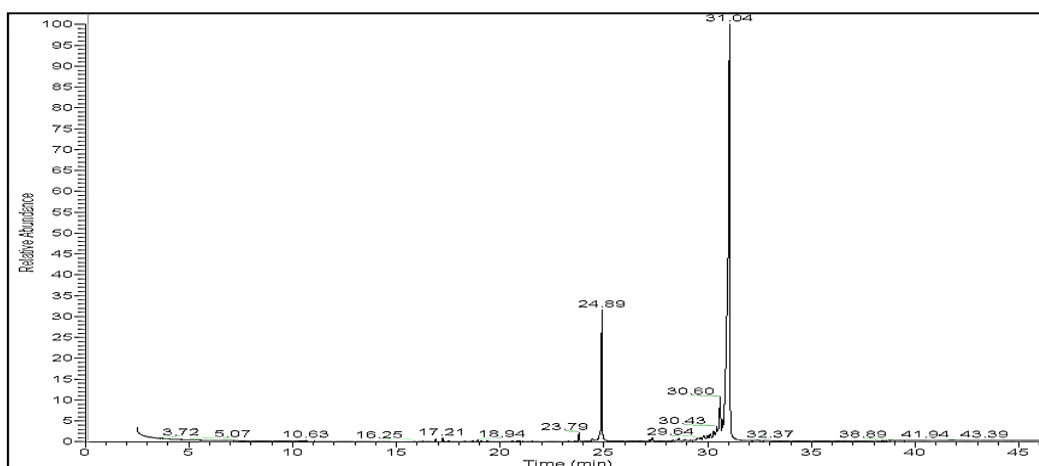
Figure B-3 Chromatogram of ^{1}H-NMR sample with Ni-Mo sulfide/γ-alumina catalyst without added internal standard, 430℃, 13.9 MPa, and 30 min

119
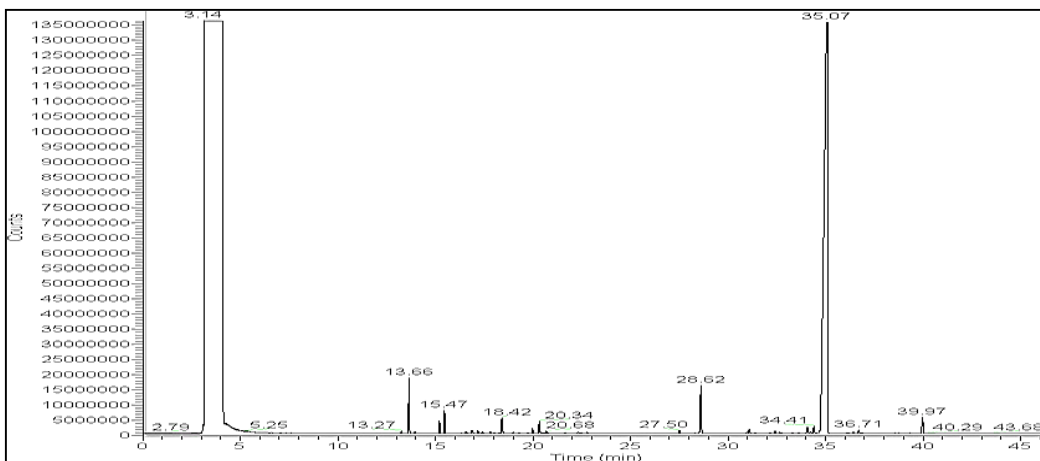
Figure B-4 Chromatogram of ¹H-NMR sample with Ni-Mo sulfide/γ-alumina catalyst with benzo(a)pyrene, 430℃, 13.9 MPa, and 30 min
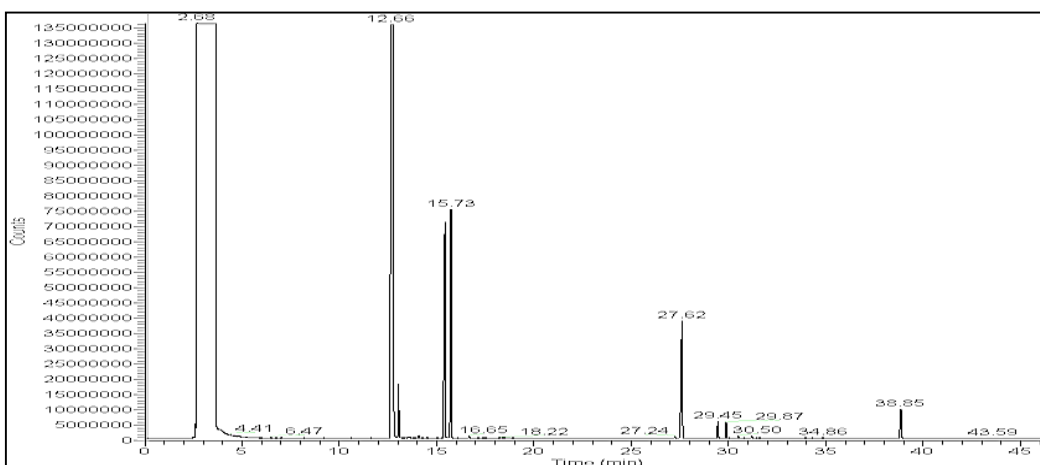
Figure B-5 Chromatogram of 1,3,6,8-tetrahexylpyrene reaction products without catalyst, 430℃, 13.9 MPa, and 30 min
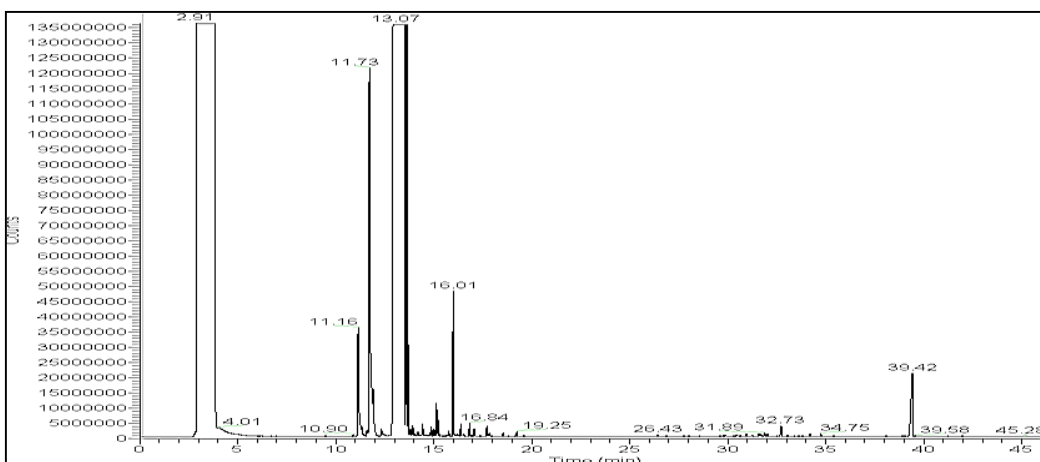
Figure B-6 Chromatogram of 1,3,6,8-tetrahexylpyrene reaction products with sulfided iron /α-alumina, 430℃, 13.9 MPa, and 30 min
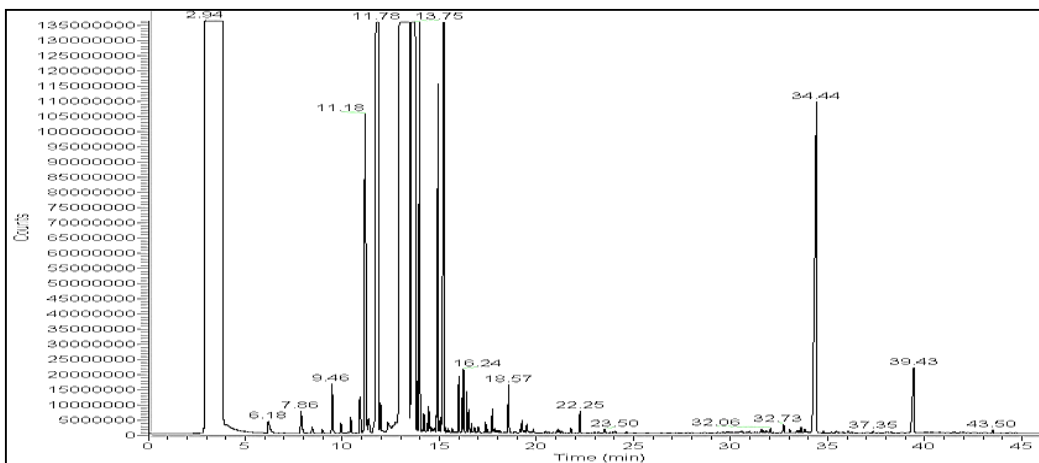
Figure B-7 Chromatogram of 1,3,6,8-tetrahexylpyrene reaction products with Ni-Mo sulfide/γ-alumina, 430℃, 13.9 MPa, and 30 min
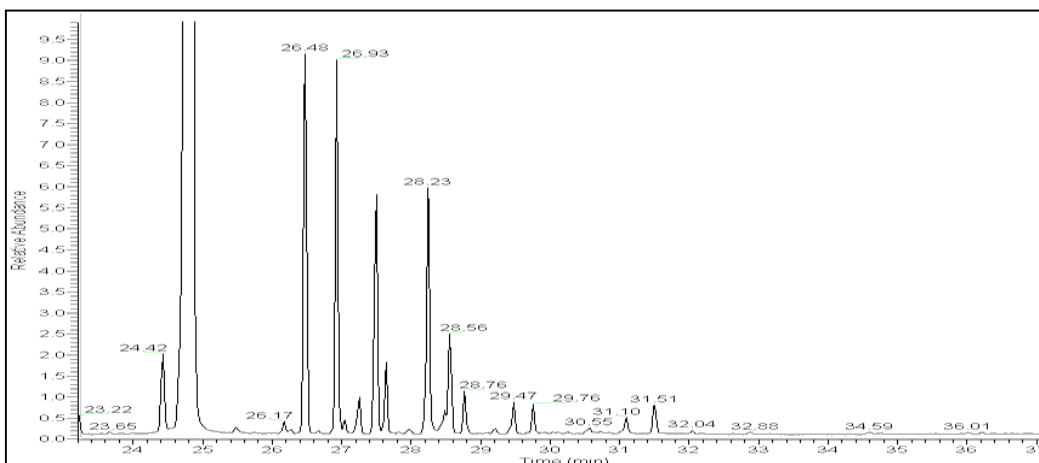
Figure B-8 Region between 23-37 minute from chromatogram of reaction products of sulfided iron /α-alumina to show pyrene and alkylpyrenes

APPENDIX C

MALDI-MS Analysis Method and Spectra

This appendix details the calculations performed on MALDI –MS spectra to obtain product identification and yields of different pathways of reaction. Included are spectra and a description of the analysis method needed to do so.

1. MALDI-MS Analysis Method

Analysis of the MALDI-MS spectra for calculation of yields of cracking, aromatic hydrogenation and addition were made based on this fact that the ratios of peaks intensities are equal to their molar ratio. Figure C-1 and Figure C-2 show the

MALDI-MS full spectra for reaction product without catalyst and for sulfided iron/α-alumina, respectively.

The MALDI-MS/MS technique is used to confirm suspected product peaks by identifying common fragment ions. The spectra of two major addition products are illustrated in Figure C-3 and Figure **C-4**.

To have the edited MALDI spectrum which only shows the selected products and their intensity the effect of isotope should be considered. Isotopes were identified using the Scientific Instrument Service Isotope Distribution Calculator at http://www. sisweb.com/mstools/isotope.htm. For example, the isotope distribution for the m/z = 468.13 cracking product peak gives an isotope distribution of 38.6%, 7.3%, 0.9% and 0.1% for each isotopes at m/z = 469, 470, 471 and 472, respectively. These ratios were used to find the actual intensity of the signal associated with each compound. In the edited MALD-MS spectra, the entire signal for each compound is assigned to the m/z corresponding to the highest abundance isotopes, i.e. ^{12}C and ^{1}H.
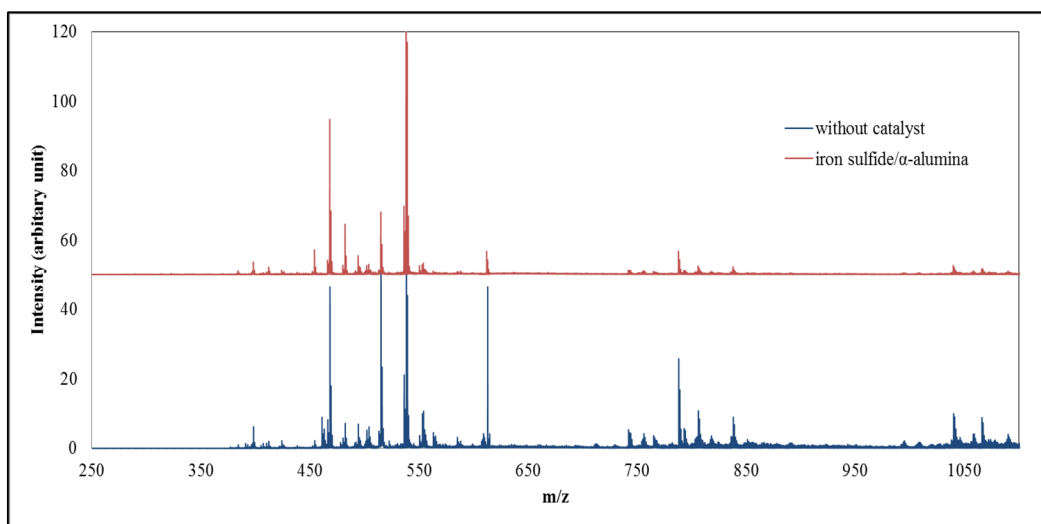
Figure C-1 MALDI-MS full spectra of reaction of 1,3,6,8-tetrahexylpyrene without catalyst (bottom) and with iron sulfide/α-alumina (top) 430°C, 13.9 MPa, and 30 min
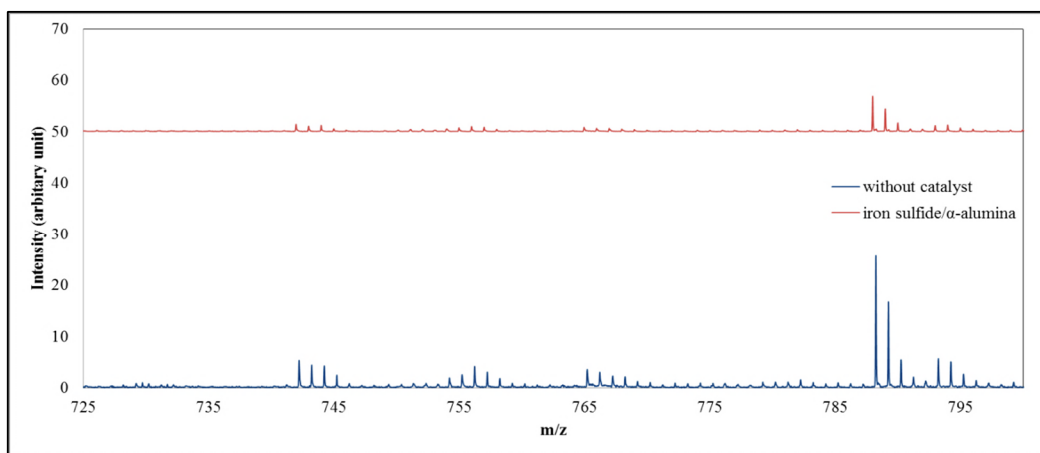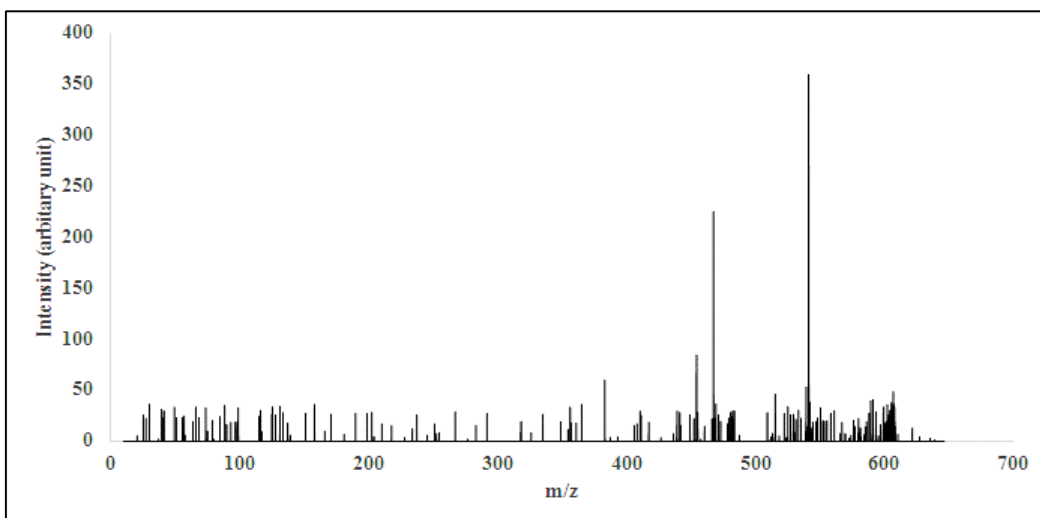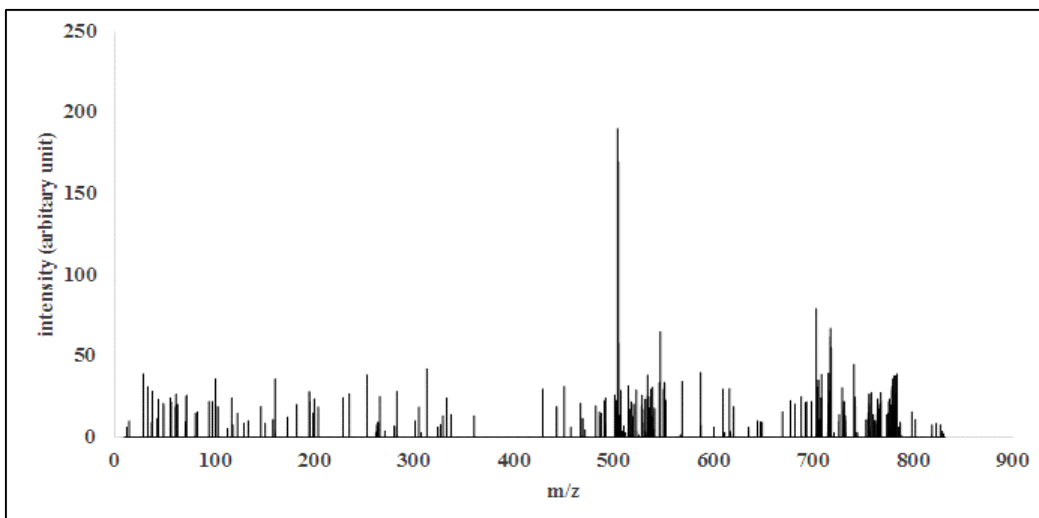
Figure C-2 MALDI-MS spectra of the reaction of 1,3,6,8-tetrahexylpyrene without catalyst (bottom) and with iron sulfide/α-alumina (top), in the range between 725-800 mass to charge ratio 430℃, 13.9 MPa, and 30 min
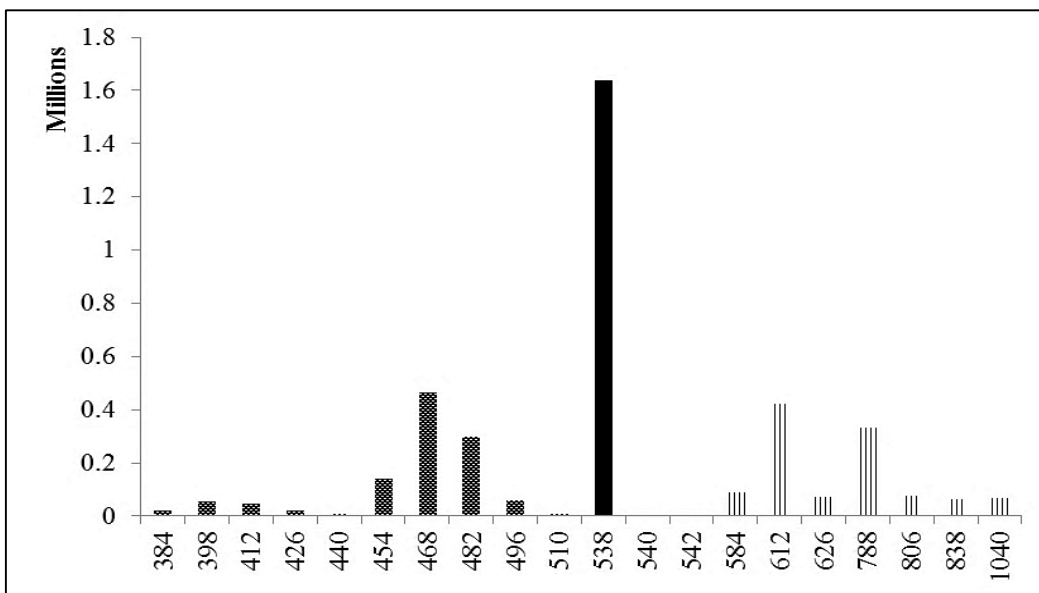

**Figure C-3** MALDI-MS/MS spectra of peak 612 m/z as the one of the major addition product peaks

Figure C-4 MALDI-MS/MS spectra of peak 788 m/z as the one of the major addition product peaks
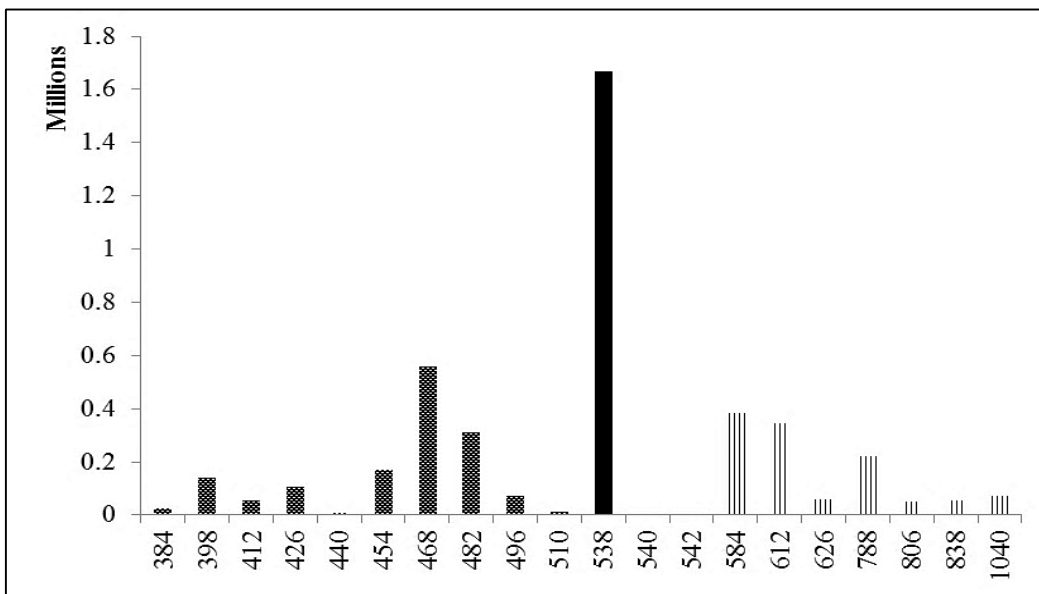
2 MALDI-MS Spectra

The following are the edited MALDI-MS product spectra used for calculations and interpretation in this study:
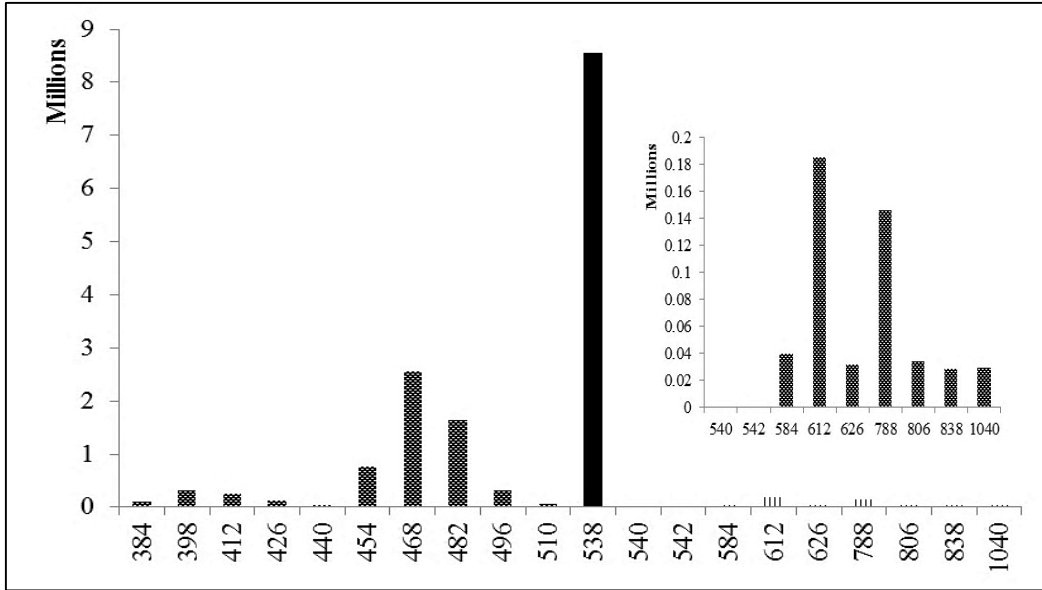

Figure C-5 Edited MALDI-MS peaks for calculation of yields of each pathway, no catalyst in N$_2$, 430°C, 13.9 MPa, and 30 min
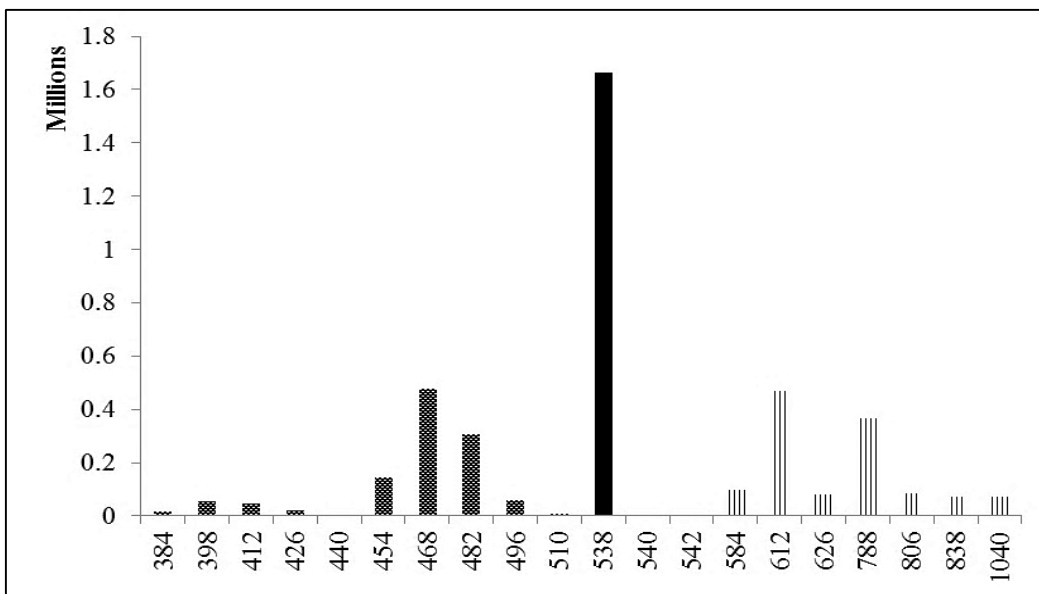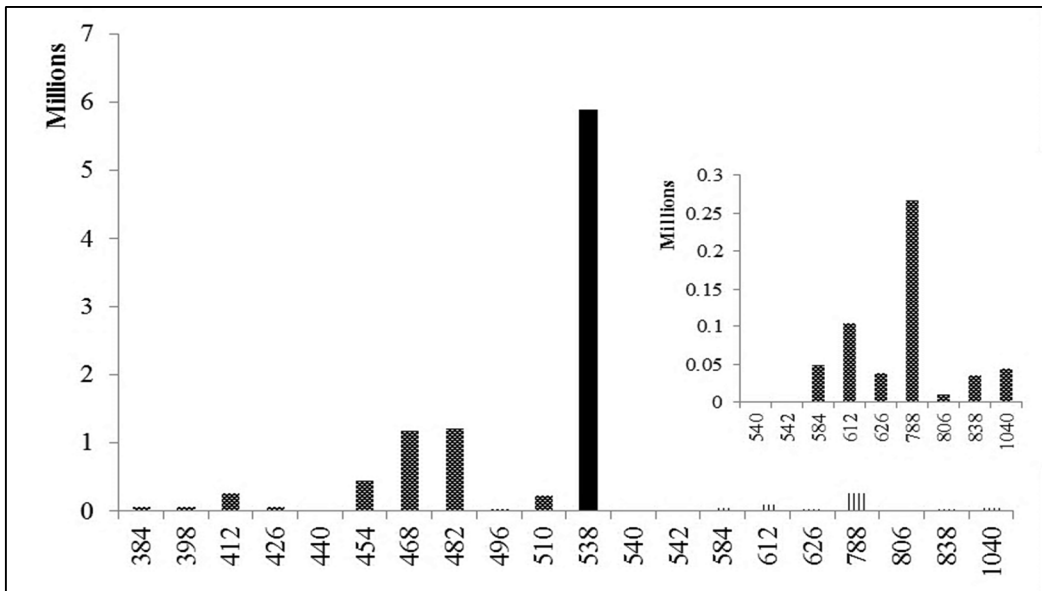
Figure C-6 Edited MALDI-MS peaks for calculation of yields of each pathway, no catalyst in H_2, 430℃, 13.9 MPa, and 30 min
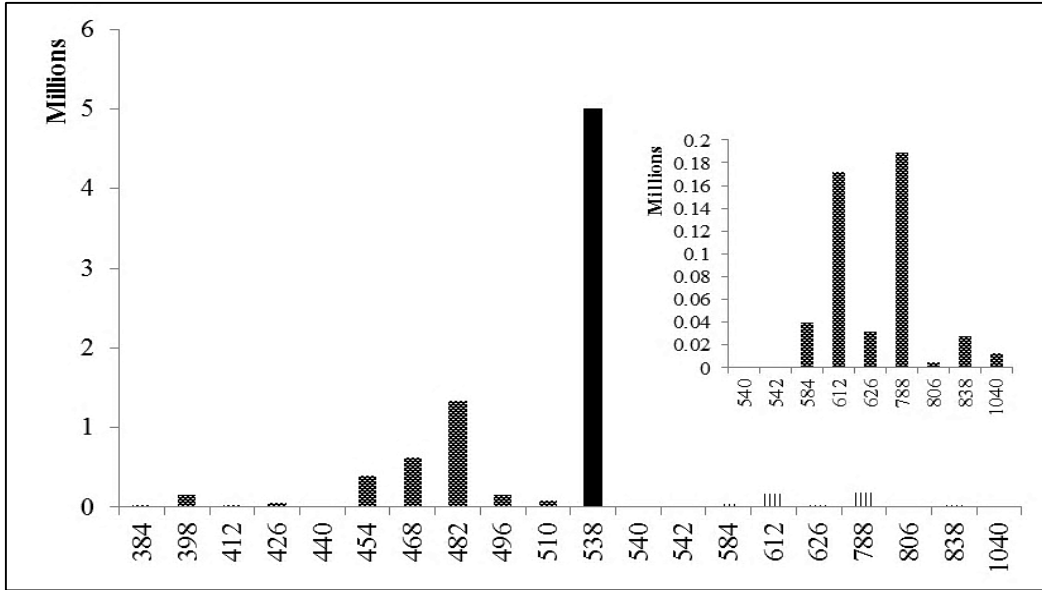

Figure C-7 Edited MALDI-MS peaks for calculation of yields of each pathway, γ-Al_2O_3, 430℃, 13.9 MPa, and 30 min
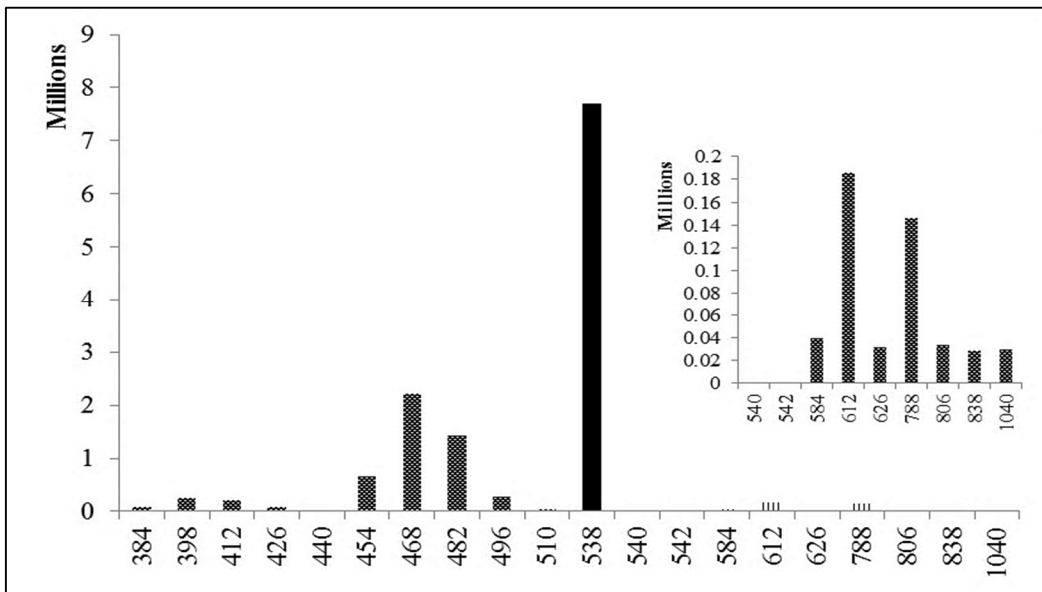
Figure C-8 Edited MALDI-MS peaks for calculation of yields of each pathway, sulfided iron/α-Al$_2$O$_3$ 430℃, 13.9 MPa, and 30 min
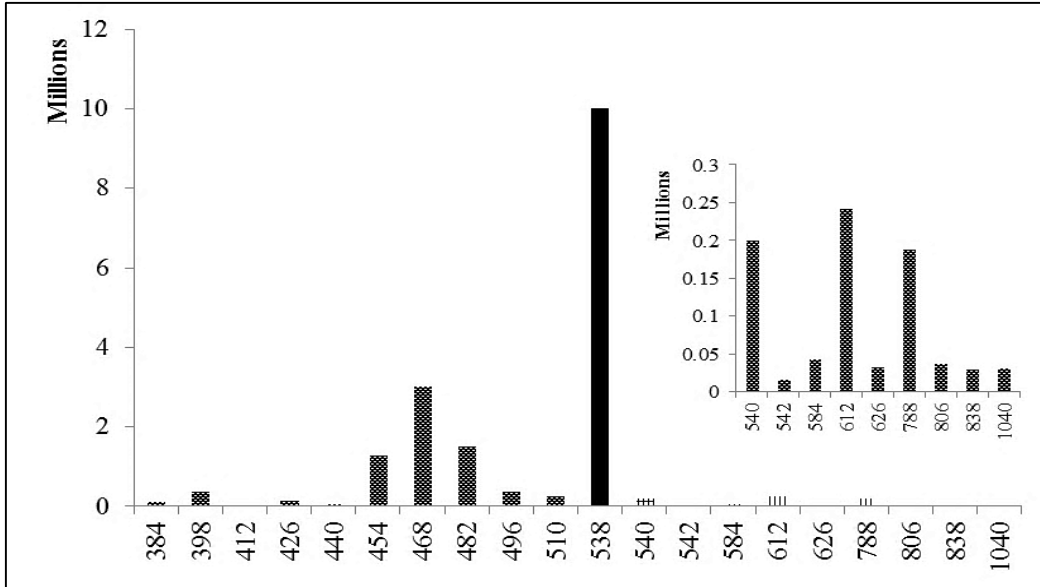

Figure C-9 Edited MALDI-MS peaks for calculation of yields of each pathway, sulfided iron/acid washed glass beads, 430℃, 13.9 MPa, and 30 min
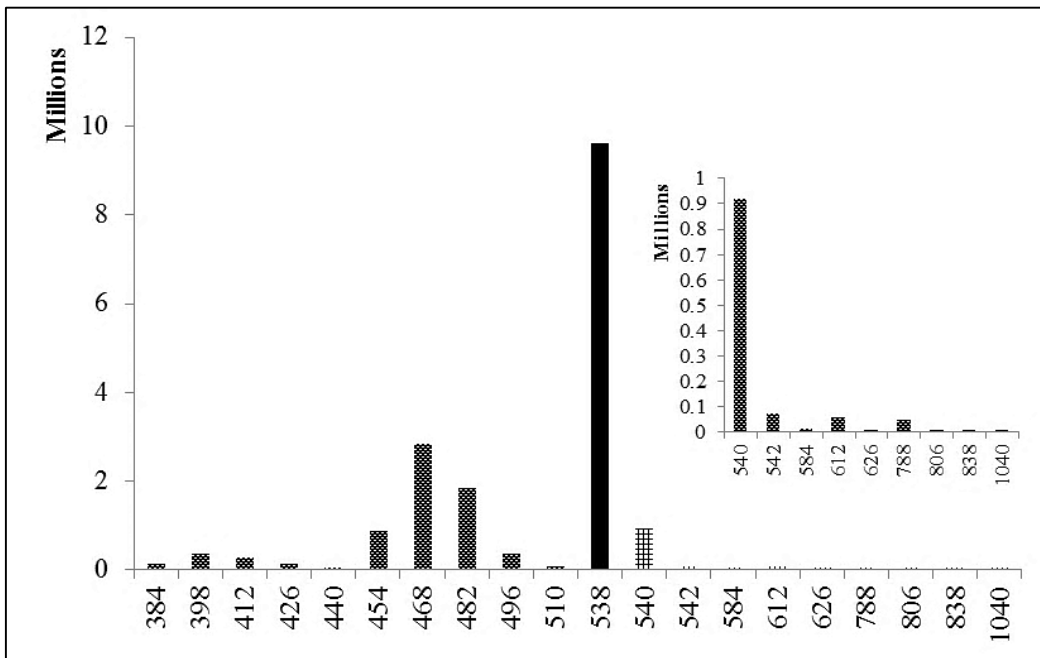
Figure C-10 Edited MALDI-MS peaks for calculation of yields of each pathway, sulfided iron/unwashed glass beads, 430°C, 13.9 MPa, and 30 min

Figure C-11 Edited MALDI-MS peaks for calculation of yields of each pathway, sulfided iron/γ-Al$_2$O$_3$, 430°C, 13.9 MPa, and 30 min

Figure C-12 Edited MALDI-MS peaks for calculation of yields of each pathway, unsupported sulfided iron, 430°C, 13.9 MPa, and 30 min

Figure C-13 Edited MALDI-MS peaks for calculation of yields of each pathway, Ni-Mo sulfide / γ-Al$_2$O$_3$, 430°C, 13.9 MPa, and 30 min

APPENDIX D

An example of yield calculation

In the following one example of calculation procedure is presented for 4 wt % iron sulfide/α-alumina.

Table D-1 Reaction and feed condition

Temperature	430°C	Cold pressure of hydrogen	5 MPa
Pressure	13.9 MPa	Catalyst amount	0.0194 g
Duration	30 min	CS$_2$	0.07 g
Mass of THP	0.994 mg	benzo[a]pyrene	0.886 mg
Mass of Tetralin	405.105 mg		

Calculation of conversion

Wavelength 239

Mass THP in the feed	0.994	mg
Mass standard	0.886	mg
HPLC response factor	1.0976	
Area of Standard peak	5990	
Area of THP peak	828.99	

$$W_{THP} = RF \times W_s \times \frac{A_{THP}}{A_s} = 1.0976 \times 0.886 \times \frac{828.99}{5990} = 0.13458 \, mg$$

$$X = \frac{W_{THP}^0 - W_{THP}}{W_{THP}^0} \times 100 = \frac{0.994 - 0.1345}{0.994} \times 100 = 86.46$$

Wavelength 270

mass THP in the feed	0.994	mg
mass Standard	0.886	mg
HPLC response factor	16.741	
Area of Standard peak	15900	
Area of THP peak	135.74	

$$W_{THP} = RF.W_s.\frac{A_{THP}}{A_s} = 16.741 \times 0.886 \times \frac{135.74}{15900} = 0.1266 \ mg$$

$$X = \frac{W_{THP}^0 - W_{THP}}{W_{THP}^0} \times 100 = \frac{0.994 - 0.1266}{0.994} \times 100 = 87.26$$

Average Conversion=86.86 %

$$Moles \ in \ feed = 0.994 \ mg \times \frac{10^{-3}}{538 \frac{gr}{mol}} = 1.84758 \times 10^{-6} mol$$

$$Reacted \ moles = 1.84758 \times 10^{-6} \times 0.8686 = 1.6048 \times 10^{-6} mol$$

$$Unreacted \ moles = 2.4277 \times 10^{-7} mol$$

Concentration of pyrene and methylpyrenes from GC

Area of standard: 419840179.714

Area of Pyrene+short alkylpyrenes: 9505827.896 (83% methyl pyrenes + 17% pyrene)

GC-FID response factor for pyrene: 0.6291

Assumption: the response factor is the same for short alkylpyrenes.

$$W_p = RF^{GC}.W_s.\frac{A_p}{A_s} = 0.6291 \times 0.886 \times \frac{9505827.896}{419840179.714} = 0.01262 \ mg$$

$$Pyrene = 0.01262 \times 0.17 = 2.1466 \times 10^{-3} mg \times \frac{10^{-3}}{202 \frac{gr}{mol}}$$

$$= 1.0626 \times 10^{-8} mol$$

$$short \ alkylpyrenes = 0.01262 \times 0.83 = 1.048 \times 10^{-2} mg \times \frac{10^{-3}}{216 \frac{gr}{mol}}$$

$$= 4.8521 \times 10^{-8} mol$$

$$total = 1.0626 \times 10^{-8} mol + 4.8521 \times 10^{-8} mol = 5.9147 \times 10^{-8} mol$$
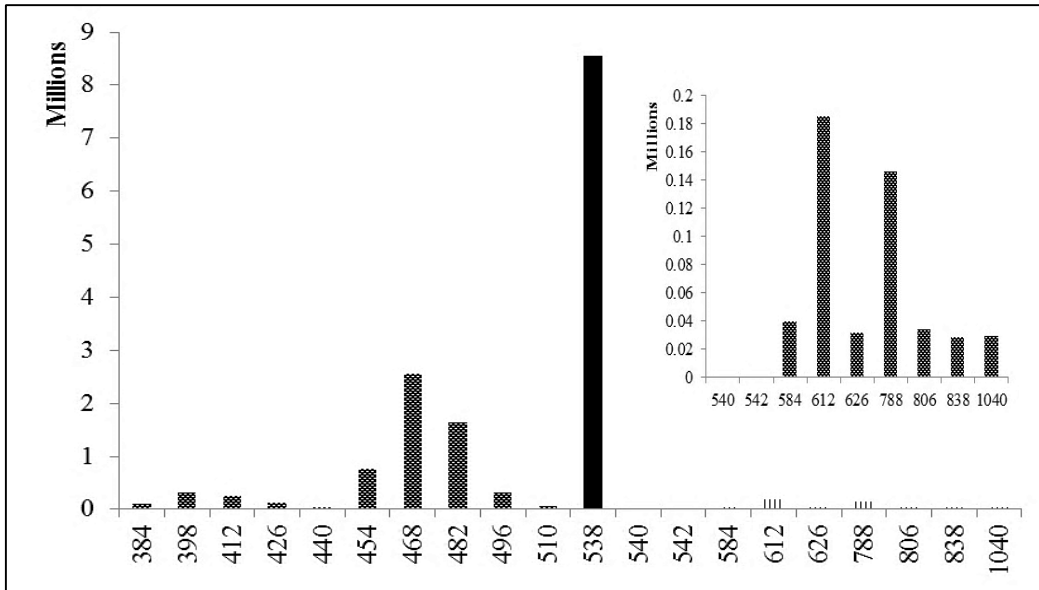
$$\frac{mol}{100 \ mol \ reacted} = \frac{5.9147 \times 10^{-8} mol}{1.6048 \times 10^{-6} mol} \times 100 = 3.68$$

Products from MALDI-MS

$$\frac{Intensity_{peak\ j}}{Intensity_{peak\ 538}} = \frac{mol_{peak\ j}}{mol_{peak\ 538}} \rightarrow mol_{peak\ j}$$

$$= \frac{Intensity_{peak\ j}}{Intensity_{peak\ 538}} \times mol_{peak\ 538}$$

$$mol_{peak\ 538} = mol_{unreacted\ THP} = 2.4277 \times 10^{-7} mol$$

Figure D-1 Edited MALDI-MS peaks for calculation of yields of each pathway, sulfided iron/α-Al$_2$O$_3$ 430℃, 13.9 MPa, and 30 min

Table D-2 The intensity of peaks for yield calculation from edited MALDI MS spectrum

m/z	Height	Ratio	mol
384	91331.3087	0.091331309	2.2175E-08
398	265210.4023	0.265210402	6.43923E-08
412	217037.776	0.217037776	5.26961E-08
426	98140.72159	0.098140722	2.38283E-08
440	32739.94205	0.032739942	7.94916E-09
454	664574.5284	0.664574528	1.61357E-07
468	2202906.951	2.202906951	5.34859E-07
482	1423166.709	1.423166709	3.4554E-07
496	274856.1949	0.274856195	6.67342E-08
510	46802.74574	0.046802746	1.13636E-08
538	7610350.076	1	2.42797E-07
540	0	0	0
542	0	0	0
584	36308.87318	0.036308873	8.81568E-09
612	169178.487	0.169178487	4.1076E-08
626	28867.39171	0.028867392	7.00891E-09
788	133061.7123	0.133061712	3.2307E-08
806	31077.51425	0.031077514	7.54552E-09
838	26055.37007	0.02605537	6.32616E-09
1040	27087.01521	0.027087015	6.57664E-09

Cracking moles= $\sum moles\ from\ peak\ 384\ to\ 510 = 1.2908 \times 10^{-6}\ mol$

Addition moles= $\sum moles\ from\ peak\ 584\ to\ 1040 = 1.0965 \times 10^{-7} mol$

Aromatic hydrogenation moles= $\sum moles of\ 540\ and\ 542 = 0\ mol$

Pyrene ring mole balance

1 mol cracking products= 1 mol pyrene (for both GC and MALDI-MS)

1 mol addition products= 2 moles pyrene

1 mol Aromatic hydrogenation= 1 mol pyrene

Cracking:

$$From\ MALDI: \frac{mol}{100\ mol\ reacted} = \frac{1.2908 \times 10^{-6}}{1.6048 \times 10^{-6} mol} \times 100 = 80.4$$

$$From\ GC: 3.68 \rightarrow total = 84.08$$

Addition:

$$From\ MALDI: \frac{mol}{100\ mol\ reacted} = \frac{2 \times 1.0965 \times 10^{-7}}{1.6048 \times 10^{-6} mol} \times 100 = 13.66$$

Aromatic Hydrogenation:

$$From\ MALDI: \frac{mol}{100\ mol\ reacted} = \frac{0}{1.6048 \times 10^{-6} mol} \times 100 = 0$$

Losses:

$$100 - 13.66 - 84.08 = 2.26\ \%$$